12-2018

Investigating the Electrodeposition of Plutonium and Curium for Safeguarding the Electrorefiner

Chantell L. Murphy
University of New Mexico

Recommended Citation

Murphy, Chantell L.. "Investigating the Electrodeposition of Plutonium and Curium for Safeguarding the Electrorefiner." (2018). https://digitalrepository.unm.edu/ne_etds/75

Chantell Lynne Marie Murphy

Candidate

Nuclear Engineering

Department

This dissertation is approved, and it is acceptable in quality and form for publication:

Approved by the Dissertation Committee:

Dr. Cassiano Endres De Oliveira ,Chairperson

Dr. Adam Hecht

Dr. Edward Blandford

Dr. Edward Arthur

Dr. Michael Simpson

Investigating the Electrodeposition of Plutonium and Curium for Safeguarding the Electrorefiner

by

CHANTELL L. MURPHY

B.S., Physics, Florida State University, 2005

M.S., Health Physics, Georgetown University, 2009

DISSERTATION

Submitted in Partial Fulfillment of the

Requirements for the Degree of

Doctor of Philosophy

Engineering

The University of New Mexico

Albuquerque, New Mexico

December, 2018

DEDICATION

This research is dedicated to my grandmother, Irene Murphy.

ACKNOWLEDGEMENTS

I cannot express enough thanks to my committee for their continued support and encouragement on this very long journey: Ed Blandford, Ed Arthur, Cassiano de Oliveira, and Adam Hecht. Thank you to Mike Simpson for opening up your lab and providing me with indispensable mentorship.

My completion of this project could not have been accomplished without the support of my colleagues from the University of New Mexico and University of Utah: Phil Lafreniere, Chao Zhang, Prashant Bagri, David Horvath, Adam Burak, Mario Gonzalez, Milan Stika, and Parker Okabe.

Thank you to my parents, Seibert and Cynthia, for always being there... especially when Samson needed looking after!

I am grateful for my large support network from Los Alamos National Laboratory who all provided me with countless opportunities to learn and grow in this field: DV Rao, Kari Senz, Carolynn Scherer, Kory Budlong Sylvester, Joe Pilat, Brian Fearey, Brian Boyer, Scott DeMuth, John Howell, Eric Rauch, Joe Durkee, Jim Doyle, and Stephen Croft.

Thank you to my tirelessly supportive and brilliantly funny friends and family who have kept me smiling and healthy through the years: Danielle Lowe, Brandie Gruenewald, Pauline Blanc, Sara Kutchesfahani, Alicia Swift, Marc Charest, Adam Wachtor, Stefanie Hausner, Grant Schneider and Tom Coppen. To Chris Jackson-Jordan for sharing large and small spaces with me, and to Cody Gipson for always answering the phone. To Maneesha Chitanvis, Raspberry Simpson, and Beyoncé Giselle Knowles-Carter, we do it for the culture.

Investigating the Electrodeposition of Plutonium and Curium for Safeguarding the Electrorefiner
Chantell L. Murphy
B.S., Physics
M.S., Health Physics
Ph.D., Nuclear Engineering

ABSTRACT

This research investigated the electrochemical deposition behavior of plutonium (Pu) and curium (Cm) for safeguarding the electrorefiner (ER) in a pyroprocessing facility. The main goal of this investigation was to evaluate the feasibility of using a safeguards concept called the neutron balance method to account for Pu in the ER. The neutron balance method relies on a known Pu/Cm ratio and measures neutrons from 244 Cm coming into and leaving a unit operation to track Pu. The application of the neutron balance approach for pyroprocessing facilities requires that Pu and Cm remain together in all extraction, product recovery, and waste streams. The electrochemical deposition experiments conducted, using a surrogate system of Tb and Gd, revealed that the Tb to Gd ratio was inconsistent between the electrolyte and the cathode deposit under different electrolyte concentrations. The Enhanced REFIN with Anodic Dissolution (ERAD) computer simulations of the same Tb/Gd surrogate system also found that the Tb to Gd ratio varied. ERAD simulations of a large-scale pilot facility also revealed that the Pu to Cm ratio was not constant between the electrolyte salt and the metal deposit when Pu co-deposition occurs. The safeguards assessment concluded that the neutron balance method was an insufficient safeguards approach for the eletrorefiner and working under the assumption that the Pu/Cm ratio was invariable resulted in the loss of significant quantities of special nuclear material (SNM) after processing only a few batches.

Contents

List of Figures

List of Tables

Nomenclature

Acronyms

ANL	Argonne National Laboratory
CE	counter electrode
Cm	curium
CV	cyclic voltammetry
DA	destructive analysis
ER	electrorefiner
ERAD	Enhanced REFIN with Anodic Dissolution
Gd	gadolinium
HEU	high enriched uranium
IAEA	International Atomic Energy Agency
IAT	input accountability tank
ICP-OES	inductively coupled plasma optical emission spectroscopy
KAERI	Korea Atomic Energy Research Institute
KAPF+	Korean Advanced Pyro-processing Facility Plus

KMP	key measurement point
LEU	low enriched uranium
LWR	light water reactor
MBA	material balance area
MOX	mixed oxide
MUF	material unaccounted for
NDA	non-destructive analysis
NFC	nuclear fuel cycle
NMA	nuclear material accountancy
O	oxidized species
OCP	open-circuit potentiometry
PM	process monitoring
ppm	parts per million
PRIDE	pyroprocess integrated inactive demonstration facility
Pu	plutonium
PUREX	Plutonium Uranium Redox EXtraction
PWR	pressurized water reactor
R	reduced species
RE	reference electrode
ROK	Republic of Korea
SBS	Signature Based Safeguards

SEM-EDS	scanning electron microscopy energy dispersive X-ray spectroscopy
SF	spontaneous fission
SNL	Sandia National Laboratory
SNM	special nuclear material
SQ	significant quantity
Tb	terbium
TRU	transuranic
W	tungsten
WE	working electrode

Greek Symbols

α	transfer coefficient
μ	electrochemical potential
η	overpotential
μ	chemical potential
ϕ	absolute potential

Nomenclature

Δ G	Gibb's free energy
C	concentration
D	diffusion coefficient
E	electrode potential
F	Faraday's constant

I	current
i	current density
J	molar flux
k	reaction rate constant
m	mass
MW	molecular weight
N	number of molecules electrolyzed
n	electrons transferred/ valance state
Q	charge
R	universal gas constant
T	temperature
t	time
V	volume
w	weight fraction

Other Symbols

∇	gradient

Chapter 1

Introduction

This project investigated the electrochemical deposition reactions of plutonium (Pu) and curium (Cm) for their relevance to safeguarding the electrorefiner (ER) in a pyroprocessing facility. The main goal of this investigation is to evaluate the feasibility of using a safeguards concept called the neutron balance method to account for Pu in the ER. For many spent fuel storage, process, and handling activities the ratio of Pu to Cm is invariant because there is no chemical process that changes the relative amounts of the actinides[1, 2]. It has been suggested by safeguards experts that Pu and Cm have similar electrochemical properties, i.e. reduction potential and oxidation state, and the Pu/Cm ratio in a spent nuclear fuel (SNF) batch will remain constant as it is processed in the pyroprocessing facility[3–10].

The neutron balance method relies on a known and invariant Pu/Cm ratio and measures neutrons from 244 Cm coming into and leaving a unit operation to track Pu in the mixture[1, 2]. The application of the neutron balance approach for pyroprocessing facilities requires that Pu and Cm stay together in all extraction, product recovery, and waste streams. Notably, the inseparability hypothesis between Pu and Cm has not been experimentally verified[9, 11]. Because of the high neutron activity of 244 Cm, it is recognized that these experiments are extremely difficult and expensive to perform[4]. However, preliminary computer simulations using an ER model called Enhanced REFIN with Anodic Dissolution (ERAD) provide the most extensive support for the hypothesis that Pu can be separated from Cm during the electrochemical deposition process[11–13].

To investigate the Pu/Cm ratio hypothesis, small scale electrochemical deposition experiments were run using a surrogate system with Tb and Gd instead of Pu and Cm. Experimental work was performed at the University of Utah's Department of Metallurgical Engineering to provide qualification of ERAD simulations. ERAD was used to model the experimental surrogate system to benchmark ERAD to make predictions for larger scale systems. The benchmarked ERAD software was then used to model an off-normal operation scenario to predict the mass transfer of Pu and Cm in an engineering-scale ER; the results of which were used to conduct a safeguards assessment.

The electrochemical deposition experiments revealed that the Tb to Gd ratio was inconsistent between the electrolyte and the cathode deposit under different electrolyte concentrations. The ERAD computer simulations of the same Tb/Gd surrogate system also found that the Tb to Gd ratio varied. ERAD simulations of a large-scale pilot facility also revealed that the Pu to Cm ratio was not constant between the electrolyte salt and the metal deposit when Pu co-deposition occurs.

1.1 Background

Plans to expand global nuclear energy production and concerns over the spread of sensitive nuclear technologies are placing increased strain on international safeguards[14, 15]. To the extent that this expansion involves new reprocessing and enrichment facilities, one of the most difficult challenges for the safeguards system will be verifying nuclear materials at these facilities.

In large bulk-handling facilities with high volume through-puts (hundreds to thousands of metric tons) and complicated equipment schematics, material unaccounted for, MUF, can represent a substantial proliferation challenge. Enrichment and reprocessing facilities, in particular, have the potential to be misused by separating Pu from SNF to develop materials for nuclear weapons[9, 12, 16].

The current commercial reprocessing method is called Plutonium Uranium Redox EXtraction or PUREX. PUREX is an aqueous chemical method used to separate SNF into uranium (U), Pu (or a Pu-U mix), and waste. Pyroprocessing is a method currently under development to reprocess SNF that attempts to combine Pu with other high activity waste products using dry electrochemical techniques, which, by comparison, lowers the potential for proliferation[17–22]. Current global interest in pyroprocessing is driving efforts to develop a standard safeguards approach for international commercial pyroprocessing facilities to verify these facilities are only being used for peaceful purposes to minimize the threat of nuclear proliferation[4, 9, 12, 23, 24].

Safeguards approaches must meet the International Atomic Energy Agency's (IAEA) standards for detecting the diversion of significant quantities of special nuclear material (SNM) in a timely manner to minimize the threat of nuclear proliferation[25]. The inherent design of pyroprocessing facilities and the large throughput makes it difficult to use traditional nuclear material accountancy (NMA) to meet detection requirements on SNM[26]. Current pyroprocess flowsheets do not incorporate an input accountability step. This means direct accounting is not done on SNF coming into the facility and the amount of Pu entering the facility is only approximated[4, 9, 12, 23, 24].

1.1.1 Nuclear Fuel Cycle

The nuclear fuel cycle (NFC) consists of industrial processes associated with the production of electricity from nuclear reactions. The NFC starts with the mining of U and ends with the disposal of nuclear waste depicted in Figure 1.1 with the spent fuel reprocessing option creating a complete cycle.

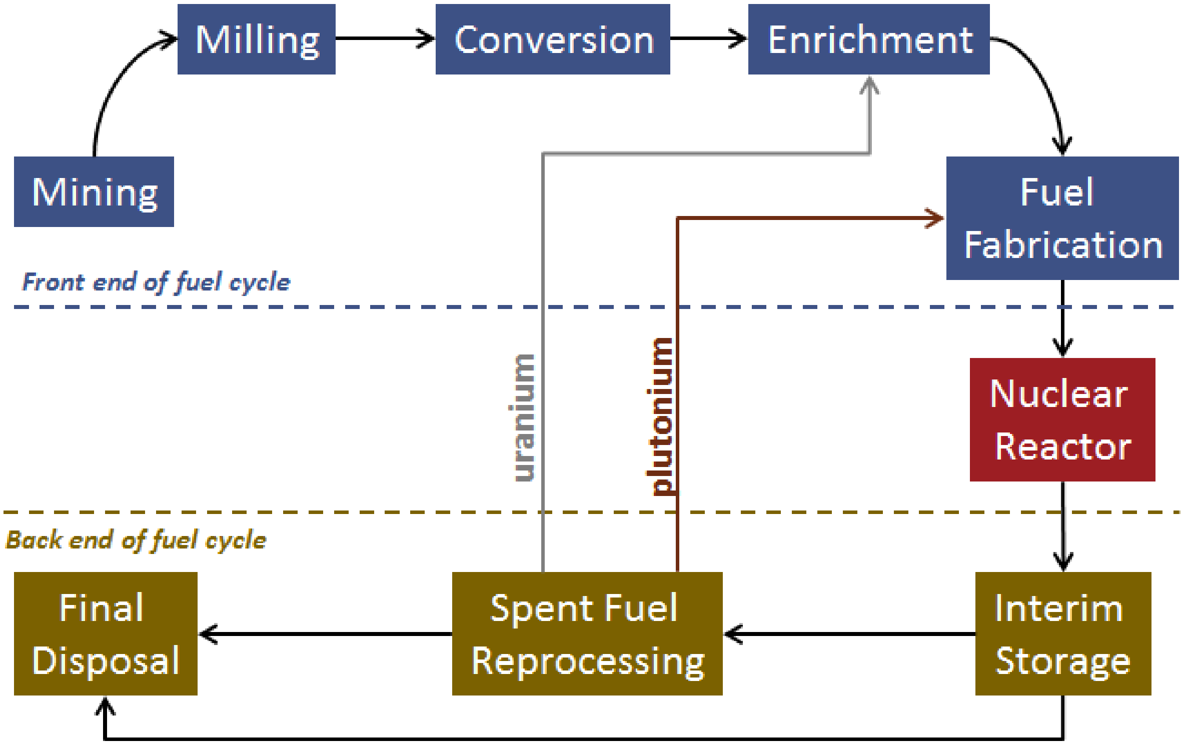

Figure 1.1: The Nuclear Fuel Cycle, adopted from [27]

Proliferation risks exist throughout the NFC depending on the form and type of the material being processed. The IAEA categorizes nuclear material according to its irradiation status and suitability for conversion into components of nuclear explosive devices. Each process in the NFC contains material that can be categorized as unirradiated direct use material, irradiated direct use material and indirect use material[25].

Direct use material can be used for the manufacture of nuclear explosive devices without transmutation or further enrichment. Direct use material includes Pu containing less than

80% 238 Pu, high enriched uranium (HEU), 233 U, chemical compound mixtures of direct use materials (e.g. mixed oxide (MOX)), and Pu in spent reactor fuel. Unirradiated direct use material is direct use material that does not contain substantial amounts of fission products, and irradiated direct use material (e.g. Pu in spent reactor fuel) contains substantial amounts of fission products. Indirect use material is all nuclear material except direct use material. It includes depleted, natural, and low enriched uranium (LEU), and thorium, all of which must be further processed in order to produce direct use material[25]. Processes that separate Pu and HEU, such as enrichment and spent fuel reprocessing, pose particular proliferation risk concerns.

Spent Fuel Reprocessing

Spent fuel reprocessing recovers U and transuranics (TRUs) for new fuel, enables a closed nuclear fuel cycle and reduces the volume and radioactivity of waste. Several European countries, Russia, China, and Japan have policies to reprocess SNF, however, US policy views reprocessing as too large of a proliferation risk[28].

There are two ways to separate SNF: PUREX and pyroprocessing. The PUREX process, which has been used in nuclear energy and weapons programs around the world, dissolves SNF in aqueous nitric acid, U and Pu are transferred to an organic phase by intensive mixing with an organic solvent extraction while the fission products remain in the aqueous nitric phase. Further process steps enable the subsequent separation of U and Pu from one another[29]. Pyroprocessing uses a dry electrochemical separation technique to separate fission products, U, and TRUs in different unit operations. Pyroprocessing differs from PUREX reprocessing because under normal operation the Pu is not separated from other actinides. Advocates of pyroprocessing say the difference makes the process significantly less proliferation-prone than PUREX[30].

1.1.2 Pyroprocessing

Pyroprocessing technology is a dry type of reprocessing technology that recovers nuclear fuel materials using electrochemical methods in molten LiCl and LiCl−KCl eutectic electrolyte. Some of the stated advantages are that pyroprocessing makes high-purity Pu recovery difficult and only a small amount of waste is created. The pyroprocess is simple, uses a small-scale facility and will be a source of nuclear fuel materials for Generation-IV reactors, and sodium-cooled fast reactors. This process also allows for the creation of indigenous technology[22].

This research focuses on the proliferation resistance assertion; pushing back on this claim and offering solutions to help enhance the safeguardability of the pyroprocessing facility.

History of Development

Pyroprocessing has a long history of development[31]. From the 1950s to the 1970s, the technology focused on separating the main fuel constituents, U and Pu, from fission products in both the US and Russia[32]. Pyroprocessing did not completely separate the fissile materials from the fission products, which was thought to be a disadvantage at the time[33]. After PUREX came into use for processing spent fuel from light water reactors, research on pyroprocessing scaled back. However, with increasing nonproliferation interest, the incomplete separation feature of pyroprocessing was recognized to be an advantage to proliferation resistance over the PUREX process.

In the 1980s, Argonne National Laboratory (ANL) used pyroprocessing to treat metallic spent fuel from the Integral Fast Reactor (IFR)[34, 35]. In the 1990s, Idaho National Laboratory (INL, or ANL-West at the time) used pyroprocessing to recycle spent fuel from the Experimental Breeder Reactor-II (EBR-II) and continued into the 2000's[36, 37].

Pyroprocessing was also proposed to separate actinides for recycling in the accelerator-driven transmutation of nuclear waste (ATW) system[38].

The Republic of Korea (ROK) has been developing pyroprocessing since 1997. Their pyroprocess integrated inactive demonstration facility (PRIDE) was developed in the early 2000's and began operation in 2012. PRIDE was developed as a cold test facility to support integrated technology and equipment into one continuous operation to achieve the engineering-scale viability of pyroprocessing above individual unit operation concepts[17, 19].

Since the late 1980s and early 1990s, more countries launched research programs developing molten salt chemistry and technology for pyroprocessing applications including Japan, India, China, England, France, Spain, Italy, Germany, and the Czech Republic. Recent pyroprocessing research activities have been well documented[32]. The pyroprocessing research activities comprise experimental demonstrations of industrial scale applications and the development of plant-level simulation models.

Pyroprocessing Facilities Today

Researchers at ANL have developed a conceptual 100 MT/y pyroprocessing facility. Only one electrometallurgical technique has been licensed for use on a significant scale. The IFR electrolytic process is used to pyroprocess 4.6 tonnes of used fuel from the EBR-II experimental fast reactor, which ran from 1963-1994. The used U metal fuel is dissolved in a $LiCl-KCl$ molten bath, and the U is deposited on a solid cathode, while the stainless steel cladding and noble metal fission products remain in the salt and are consolidated to form a durable metallic waste. The HEU recovered from the EBR-II driver fuel is downblended to $< 20\%$ enrichment and stored for possible future use[36, 37].

GE Hitachi is designing an Advanced Recycling Centre (ARC) that integrates electrometallurgical processing with its PRISM fast reactors. The main feed is used fuel from light water reactors, and the products are fission products, U, and TRUs (Np, Pu, Am, Cm), which become fuel for the fast reactors. The U can be re-enriched or used as fuel for CANada Deuterium Uranium (CANDU) reactors. As the cladding reaches its exposure limits, used PRISM fuel is recycled after the fission products are removed. Waste forms are metallic for noble metal fission products, and ceramic for groups 1 and 2 metals and halogen fission products. A full commercial-scale ARC would comprise an electrometallurgical plant and three power blocks of 622 MWe each (six 311-MWe reactor modules)[39].

The ROK has established three pyroprocessing-related facilities at the Korea Atomic Energy Research Institute (KAERI) site: PRIDE, Advanced Spent Fuel Conditioning Process Demonstration Facility (ACP), and DUPIC Fuel Development Facility (DFDF). The ACP is a technology that KAERI has been developing since 1977 to manage spent fuel. KAERI and Los Alamos National Laboratory (LANL) published a paper on the Safeguardability of the ACP; the general concept used in that paper guides the initial calculations of this work[3]. The ACP involves separating U, TRU (including Pu), and fission products (including lanthanides). The ACP uses a high-temperature LiCl−KCl bath from which U is recovered electrolytically to concentrate the actinides, which are then removed together (with some remaining fission products). The U product is fabricated into fast reactor fuel without further treatment. The process is intrinsically proliferation-resistant because it is so hot radiologically and the Cm provides a high level of spontaneous neutrons. Over 96% of the used fuel is recycled in this process[3].

For NMA, a pilot-scale facility, Korean Advanced Pyro-processing Facility Plus (KAPF+) was designed to analyze the safeguardability of the ACP. The facility stands alone physically (operationally), and is administratively isolated from reactors and interim spent-fuel storage facilities. The main process of the facility is the ER concept. The KAPF+ consists of 2 modules with a capacity of 200 MTHM/year for treating pressurized water reactor (PWR) SNF. Each module consists of 4 ERs processing about 125 kgHM/day operating for 250 days per year[40]. One operation day is 24 hours. The KAPF+ processes PWR SNF cooled for more than 10 years. The fuel referenced is the Hanbit (former Yonggwang) Unit 3 & 4 (PLUS7) which has typical features of 16 x 16 rod array, initial enrichment of 4.5 wt%, and burnup of 55,000 MWd/MTU[3, 20].

Russian pyroprocessing consists of three main stages: dissolution of the SNF in molten salts, precipitation of Pu dioxide or electrolytic deposition of U and Pu dioxides from the melt, and then processing the material deposited on the cathode or precipitated at the bottom of the melt for granulated fuel production. The process recovers the cathode deposits without changing their chemical composition or redistributing the Pu. All used fuel is reprocessed, with the goal of having a complete recycle of Pu, neptunium, americium, and Cm, as well as the U. This process, combined with vibropacking in fuel fabrication will be used to produce fuel for the BN-800 fast reactor. The technologies complement one another well and involve high levels of radioactivity throughout, making them self-protecting against diversion or misuse. At the Mining and Chemical Combine (MCC) Zheleznogorsk, which hosts a pyroprocessing module, civil PuO_2, ex-weapons metal Pu, and depleted uranium (DU) are combined into granulated MOX. The MOX is sent to the Russian Institute of Atomic Reactors (RIAR) at Dimitrovgrad for vibropacking and producing fuel assemblies for the BN-800 fast reactor. The RIAR has substantial experience in reprocessing used fuel from the BOR-60 and BN-350 fast reactors and has developed a pilot scale pyroprocessing demonstration facility for fast reactor fuel[41, 42].

1.1.3 Pyroprocess Flowsheet

Although different pyroprocess programs have varying flowsheets, the key unit operations are similar, as seen in figure 1.2.

Metal or oxide SNF assemblies are received at the facility and are mechanically chopped

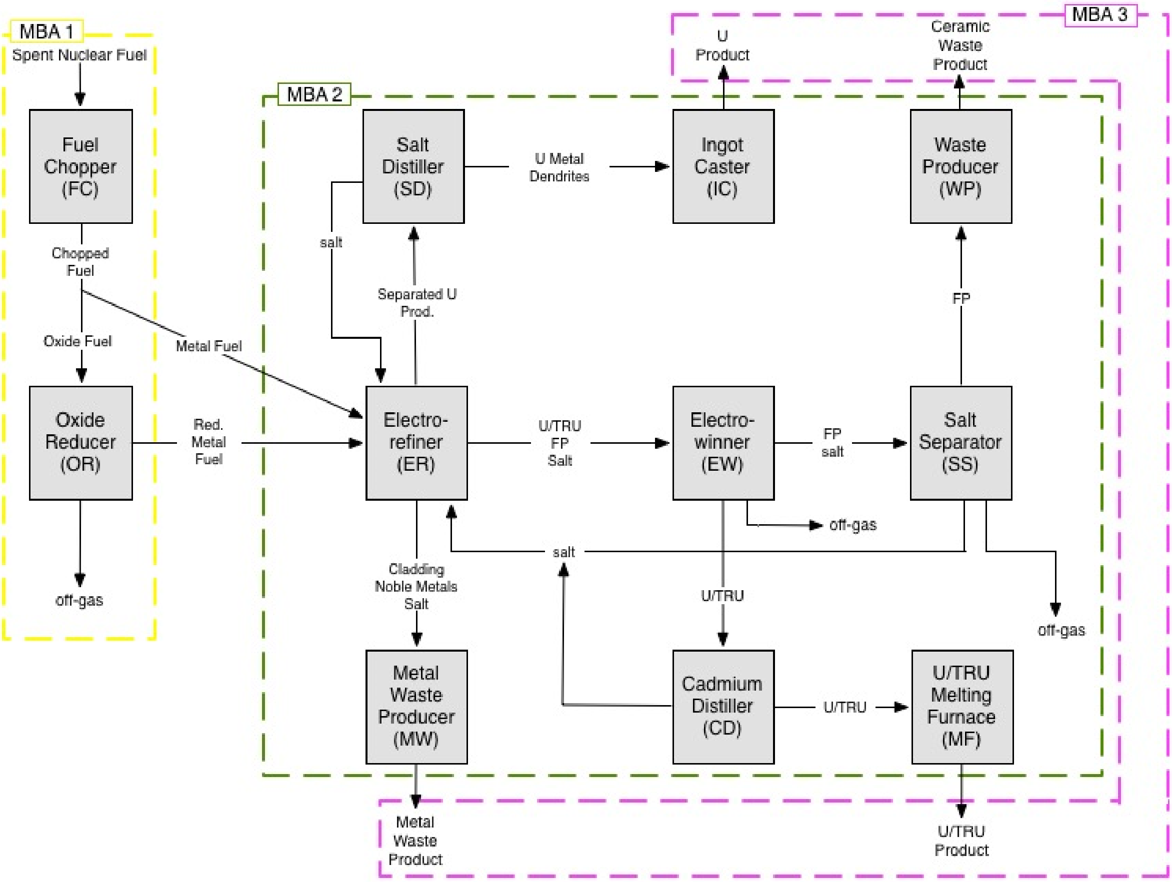

Figure 1.2: Overview of Pyroprocessing Flowsheet

and decladded. Voloxidation removes volatile fission products and cesium. The used oxide fuel is electrolytically reduced to metal. During electrolytic reduction, cesium, strontium, and other Groups I and II fission products form chlorides and partition into the molten $LiCl-Li_2O$ electrolyte. The reduced metal fuel is then transferred to an ER. U and active fission products, including TRU, are electrochemically and chemically oxidized from the anode basket and dissolve as chloride salts into the $LiCl-KCl$ molten salt electrolyte. Simultaneously, either U or a U/TRU alloy is reduced onto the cathode (solid or liquid metal), recovered, and processed into a metal fuel ingot. The cathode processor removes excess salt from the U dendrites that have reduced on the cathode. The fuel fabrication process produces metal slugs containing an alloy of U, TRU, zirconium, and a small weight fraction of rare earth fission products. Electrowinning is used to extract U/TRU metal from the liquid cadmium cathode (LCC) as well as rare earth elements. The undissolved cladding and noble metal fission products in the anode are processed into a metal waste form, whereas lanthanides can be separated from the salt and stabilized into a ceramic waste form using a salt cleanup process. The clean salt (LiCl−KCl) is recycled back into the ER.

Figure 1.2 divides the flowsheet into three logical material balance areas (MBAs) where quantity and physical inventory of nuclear material can be determined for IAEA material accounting purposes. MBA 1 is where the SNF entering the facility is first accounted for and is done in open air atmosphere, MBA 2 is where separation occurs in the argon air hot cell, and MBA 3 contains the product waste materials.

1.1.4 Electrorefiner

The ER is in MBA 2 and is where SNF is electrochemically separated into U, U/TRU, and waste. A molten LiCl−KCl eutectic salt, held at a temperature of 773 K, and enhanced with dissolved UCl_3, serves as the electrolyte for the ER. The U, TRUs, active metal fission products, bond sodium, and some Zr dissolve from the anode basket into the molten salt. Separation occurs by passing a current or potential from the spent fuel anode baskets to the solid cathode. The noble metal fission products and the cladding remain behind in the anode baskets.

Fresh UCl_3 must be supplied to the ER for every batch of spent fuel processed. UCl_3 reacts with bond sodium and TRUs in the incoming fuel to form chloride salts and uranium metal. The reaction of UCl_3 with bond sodium is shown in Eq. 1.1.

$$\mathrm{Na} + \mathrm{UCl_3} \longrightarrow 3\,\mathrm{NaCl} + \mathrm{U} \tag{1.1}$$

Without the addition of UCl_3, the supply of dissolved UCl_3 in the electrolyte would gradually be depleted and the U product produced would become increasingly contaminated with Pu.

The ER unit operation is of particular safeguards significance because the electrolyte contains significant quantities of Pu and depending on how the ER is operated, Pu can perversely codeposit along with U on the steel cathode. It is difficult to determine the isotopic composition in real time because there is limited data on normal operating signatures, the molten salt bath is not necessarily homogeneous, and SNM can get lost in holdup[4].

In the US, two engineering-scale ERs have been used to process SNF, the Mark-IV and the Mark-V[43]. Each contained over 500 kg of molten chloride salt[36]. A diagram of the Mark-IV ER is seen in figure 1.3[43].

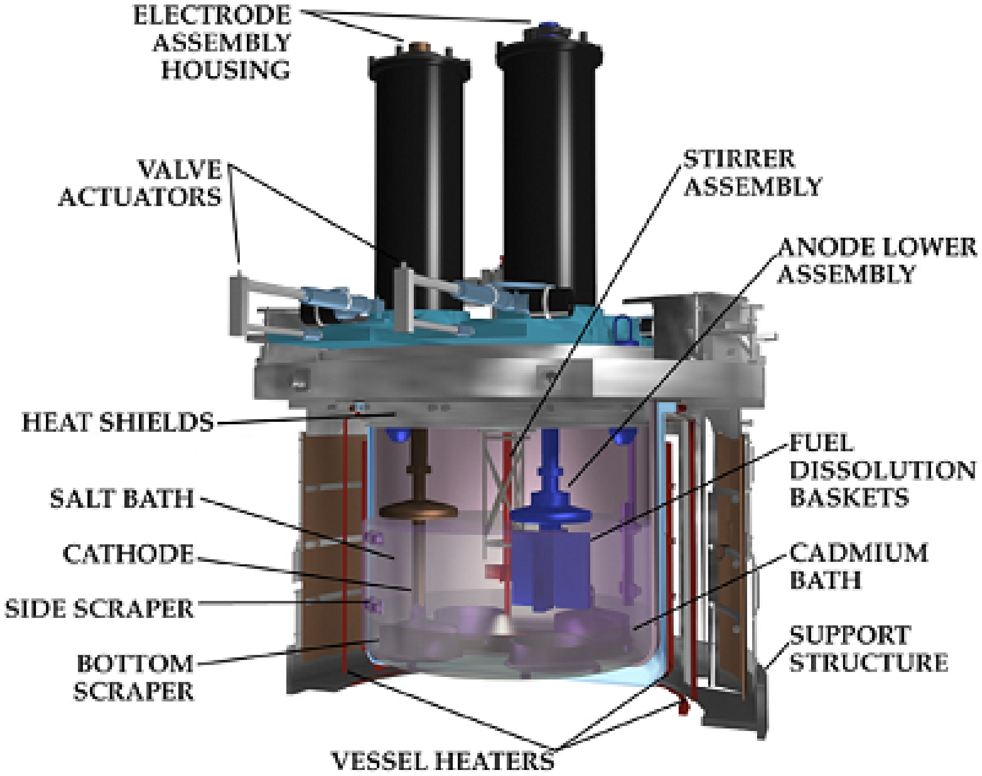

Figure 1.3: Mark IV Electrorefiner

The eletrorefiner was composed of an anode with fuel dissolution baskets, a solid cathode for collecting U, and an electrolyte (LiCl-KCl eutectic) that served as a transport bath heated to 773 K with vessel heaters. In some designs an additional cathode, a LCC, was used to recover U and TRU. For enhancing mass transfer, a stirring mechanism may be installed, as was done in the design of MARK-IV ER[10].

Once the U is deposited on the cathode, the cathode is scraped. Several ER designs incorporate a cathode scraper for in-situ removal of the deposited U dendrites. At times, this scraper can catch on the growing cathode deposits, slowing or stopping the rotation of the electrode[12]. A self-scraping concept using a graphite cathode was introduced in South Korea's PRIDE facility. The ER uses a graphite electrode, U dendrites are deposited and fall down from the electrode spontaneously, and are collected at the bottom of the reactor and withdrawn with a bucket-type transfer for further distillation[37].

Several electrorefining campaigns were conducted using the Mark-IV, having treated about 830 kgHM of driver fuel[36]. The technical issues studied dealt with current efficiency, U recovery efficiency, zirconium recovery, and understanding the interactions of the cadmium pool with the rest of the system.

While valuable information was certainly gained from conducting these campaigns, the experimental studies have significant drawbacks. Large-scale experiments are very expensive and time-consuming and cannot simulate all cases that appear in practical operations. A good simulation model can be much cheaper and less time consuming, and an effective tool to aid in the design and evaluation of electrochemical cells.

1.2 Motivation

The motivation for this research was based on the proposed safeguards approaches for future pyroprocessing facilities all relying on the neutron balance method to track Pu. The neutron balance method requires the mass ratio of Pu and Cm to remain the same in all processing and extraction steps. Researchers at the University of Utah provided an initial computer simulated assessment of the applicability of the neutron balance approach in the pyroprocessing system and determined the Cm did not track with Pu and that experimental verification needed to be conducted[11]. Idaho National Laboratory performed an experimental study on the feasibility of tracking Pu using neutron measurements and a well known Pu/Cm ratio but the Cm levels were too low to detect[9].

1.3 Objective

The objective of this research was to quantitatively determine if the neutron balance method will be a viable safeguards technique. The determination was made by conducting small-scale experiments using a surrogate system of Tb and Gd, performing simulations of the experiments to qualify ERAD as an appropriate model for this work, performing large-scale ERAD simulations of off-normal operating conditions to test the Pu/Cm ratio hypothesis, and finally by providing a safeguards assessment of the scenario results.

1.4 Thesis Organization

The structure of the dissertation follows a methodological progression of chapters. Chapter one presents the introduction and background. It provides the motivation and objective of this research. Chapter two provides a review on international safeguards and past work done on pyroprocessing safeguards. The chapter covers nuclear material accountancy (NMA) and process monitoring (PM), and challenges for pyroprocessing facilities. Chapter three contains the background and review on electrochemistry fundamentals and the mechanics of electrochemical deposition. Chapter four contains the review on modeling and simulation work on pyroprocessing and the ER. Chapter five discusses the experimental methods used in this research. The chapter describes the equipment and chemical used and the test procedures followed for conducting the experiments. Chapter six presents the ERAD qualification analysis. The results of the experiments and Tb/Gd deposition simulations were compared and presented to draw conclusions about ERAD performance and utility in this investigation. Chapter seven contains the safeguards assessment conducted on this work. This chapter draws upon the results from the experiments and ERAD simulations to explore the utility of the neutron balance method as a viable safeguards technique. The conclusions are found in Chapter eight.

Chapter 2

Pyroprocessing Safeguards Background

Safeguards applied by the IAEA are an important element of the global nuclear non-proliferation regime. Safeguards refers to all measures established in a State to prevent the diversion of nuclear material from peaceful uses and to enable the timely detection of diversion of any material to the production of nuclear explosive devices[INFCIRC/153, para. 28][44]. The IAEA applies safeguards to verify that commitments made by States under safeguards agreements with the IAEA are fulfilled.

Safeguards agreements focus on nuclear material and the important element of implementation of safeguards is NMA on unirradiated direct use material, irradiated direct use material and indirect use material[26]. The main technical objectives are the timely detection of the diversion of declared nuclear material, the timely detection of the misuse of the facility to produce undeclared product from undeclared feed, and the timely detection of the misuse of the facility to produce product at Pu concentrations higher than declared[25].

2.1 Nuclear Material Accountancy

The timely detection of diversion of significant quantities of nuclear material is traditionally carried out with NMA[1], which establish the quantities of nuclear material present within defined areas and the changes in those quantities within defined periods[[25], paragraph 6.2]. Significant quantities are defined as 8 kg of Pu or 233 U and 25 kg of HEU with a timeliness goal of one month[25].

Nuclear material is accounted for by balancing the material entering the facility or process with the material leaving the facility or process. The discrepancy between the two transfer points is called material unaccounted for (MUF) described in equation 2.1.

$$MUF = M_{in} + T_{in} - M_{out} - T_{out} \tag{2.1}$$

Where M_{in} is the starting inventory, T_{in} are transfers to inventory, M_{out} is the ending inventory, and T_{out} are transfers from inventory.

Measurement uncertainties create MUF in all bulk facilities. Measurement precision is based on the standard deviation of MUF, σ_{MUF}. If MUF is greater than some threshold, usually 2-3 σ_{MUF}, the IAEA rejects the hypothesis that real MUF is zero and investigates the possibility that diversion has occurred. Considerable effort is aimed at assessing measurement uncertainties to estimate σ_{MUF}.

For large throughput nuclear facilities, such as commercial reprocessing plants, it is difficult to satisfy the IAEA safeguards accountancy goal for detection of diversion. The inherent design of pyroprocessing facilities makes it difficult to close out the mass balance with low uncertainty using NMA alone since there is less safeguards experience with these facilities. High temperature salt and metal solutions are highly corrosive; such an

---

[1] Also referred to as Material Control and Accountancy (MC&A)

environment will be challenging for safeguards equipment and instruments[4, 45]. Unlike aqueous reprocessing, pyroprocessing facilities do not have an input accountability tank (IAT), which causes high uncertainty for the initial inventory measurement and generates problems for calculating an accurate mass balance causing large measurement uncertainties of feed, product, waste and in-process material.

In addition, the need to keep the ER at a steady state prevents periodic plant flushouts from being a feasible option for material accounting[16]. Sampling procedures, destructive analysis (DA) and non-destructive analysis (NDA) for feed, product, waste and in-process materials are not yet established, process parameters are not well established, and signatures and indicators of the physical model need to be updated.

Several publications have demonstrated benefits from using PM on nuclear facilities as a complementary safeguards measure to NMA[16, 23, 29, 46]. More recently, this concept has been expanded and preliminarily demonstrated for pyroprocessing technology. The Signature Based Safeguards (SBS) concept is part of this expansion and is built around the interpretation of input from various sensors in a declared facility coupled with complementary NMA methods to increase confidence and lower SEID[36, 47].

One proposed solution to track Pu throughout a pyroprocessing facility is the neutron balance method, which tracks the Pu/Cm ratio throughout processing by measuring spontaneous fission neutrons from 244 Cm. The basis for this suggested method is that Cm and Pu have similar properties in nonaqueous, high-temperature systems which suggests the neutron balance method may work in pyroprocessing facilities. Safeguarding is essentially implemented by verifying that the neutrons per second entering the process are equal to the neutrons per second leaving the process. As long as Cm tracks Pu throughout the process, this is a logical and accurate safeguards method[1–8, 10, 11].

2.2 Pyroprocessing safeguards studies

Concepts and approaches for safeguarding pyroprocess facilities are currently being developed and neutron-based techniques are a significant part of those developments. The Office of Nuclear Energy's Fuel Cycle Technologies' Materials Protection, Accounting and Control Technologies (MPACT) Campaign is pursuing advanced instrumentation, analysis tools and integration methodologies to support safeguards applications in future advanced fuel cycle processes. The MPACT campaign is supporting the development of a high-dose neutron detector to assay product ingots from the ER[48].

Sandia National Laboratory (SNL) conducted an integrated safeguards and security study of a pyroprocessing facility[16]. Cipiti et al., used a model of a commercial-scale electrochemical plant developed in Matlab Simulink to track the mass flow rates of the fuel and salt through the various unit operations. The model also simulates materials accountancy, process monitoring measurements, and physical protection. These measurements are then used to calculate inventory balances during normal operation and diversion scenarios, which allow for the development of strategies and options for safeguarding nuclear material, contingent upon the feasibility of the measurement technology.

The study identified four challenge areas and suggested new approaches or new technologies for meeting NMA goals. The inability to flush out the plant requires a move to a near real time accounting (NRTA) regime where plant inputs, outputs, and full inventory measurements are made once per day with and optimized timing sequence to minimize the burden to the operator. The lack of an accountability tank requires an alternative input measurement of the incoming SNF, which could involve measuring the full fuel assemblies, the voloxidation powder, the shredded fuel, or the melted reduction product. The third challenge area is inventory measurement of the ER. Salt sampling and analytical techniques will most likely be required to achieve low uncertainty measurements, but other process monitoring techniques may be examined. Sampling will be required at a pause in the process to ensure a representative sample. Finally, the U and U/TRU metal products will need to be measured with low uncertainty to close out the inventory balance. The melted dendrite phase was identified as a good point to take a sample for accountancy, but other NDA techniques should be considered as well[16].

The ASA-100 Project, Advanced Safeguards Approaches for New Nuclear Fuel Cycle Facilities, commissioned by the NA-243 Office of NNSA, reviewed and developed advanced safeguards approaches for three demonstration facilities, the Advanced Fuel Cycle Facility (AFCF), the Advanced Burner Reactor (ABR), and the Consolidated Fuel Treatment Center (CFTC). The ASA-100 Project determined there were four prospective safeguards approaches for a pyroprocessing facility, neutron balance - Cm accounting, electrorefiner assay, homogenized input, and assay of Pu in spent fuel via Pu/Cm ratio and DA. All of the options rely on the assumption that the Pu/Cm ratio remains constant throughout all unit operations in the facility[4].

Acquisition path analysis studies were conducted using two of the safeguards options, homogenized input, and assay of Pu in spent fuel via Pu/Cm ratio and DA. The studies concluded that ultimately the accuracy of the Pu input accountancy measurement dictates the ability to detect an 8 kg diversion using traditional NMA or the use of additional measures to supplement the safeguards. Anomalous activities can be detected with NRTA on a on a batch-by-batch basis, but at cost of considerable complexity. The neutron balance method did provide some accountancy data, but relied on homogeneity of the ER, the electrolysis TRU separations unit and the U/TRU product. The study indicated adding a neutron source, such as 252 Cf or other neutron sources, as a way to fool the neutron assay equipment. The possible use of absorbers and shielding to conceal the possible diversion of Pu and other actinides would need to be considered[4].

The integrated video/neutron monitoring and PM (including UCl_3 and Cl_2 monitoring) were determined to be timely detection systems. PM for measuring low UCl_3 concentration in the salt and for low threshold detection of Cl_2 gas production would detect several diversion scenarios. Although time consuming and expensive, DA of salt samples also helps to detect the addition of a neutron emitter (such as 252 Cf) to spoof the Pu/Cm ratio. However, homogenization of the ER and other containers must be assured. The report determined that conceptually, it appears feasible to use traditional NMA and other safeguards measures to safeguard at least a small pyroprocessing facility. The determining factor will most likely be whether the DA and NDA analytical techniques and tools can be improved to the level of accuracy required[4].

The applications of Cm measurements for safeguarding in aqueous reprocessing plants for high-level liquid waste, spent fuel assemblies, and leached hulls have been theoretically studied by researchers from LANL[2, 5]. It was concluded that the neutron balance method could be applied to the head end of an aqueous reprocessing facility to determine if any Pu was diverted between the receipt of the SNF and dissolution in the IAT, where about 99.9% of the SNF is dissolved. Application of the neutron balance method further into the process requires that Pu and Cm behave identically in all of the extraction and product recovery steps.

The ER poses particular safeguards concerns because under certain operating conditions Pu can be separated from other TRUs and should be closely monitored using real time or NRTA[16]. While Pu and Cm exhibit similar electrochemical behavior [49, 50], previous studies have shown that certain off-normal operating conditions in the ER may lead to the co-deposition of Pu on the cathode causing it to separate from the other TRUs[11–13].

INL performed a study on the feasibility of tracking Pu using neutron counts and a well known Pu/Cm ratio[9]. The study measured the Pu and Cm content in the SNF and the ER salt using inductively coupled plasma mass spectrometry for both fast reactor and light water reactor (LWR) fuel. The Cm level in fast reactor fuel was below the detection limit. The Pu/Cm ratio was found to be 1.16104 for the LWR fuel sampled. In both cases, the Cm content in the electrorefiner salt was below detection limits. The INL study demonstrates the extreme difficulty involved with quantifying 244 Cm concentrations, especially if the goal is to quantitatively track Pu. The results of these salt and fuel analyses do not refute the concept of using 244 Cm concentration to track Pu through the electrorefining process. However, they do demonstrate the difficulty involved with validating this method because the samples of spent LWR fuel need to have significant accumulation from processing multiple batches in order to have enough 244 Cm to detect via chemical analysis. The large scale pyroprocessing activities at INL are currently limited to spent metal fuel, and there is no quick or cheap path to obtaining samples affected by processing large quantities of oxide spent fuel.

2.3 Neutron Counting

For safeguards purposes, detection of spontaneous fission (SF) neutrons from cm is an accepted, NDA technique that has been applied to verify SNM content in used fuel and other safeguards activities[1, 2, 5]. The 244 Cm isotope is used because it is the dominant source of SF neutrons in the SNF after a standard cooling period[2]. Neutrons are highly penetrating with a low rate of interaction with matter and are insensitive to interference by other gamma-emitting radionuclides. Neutron rates are related to the amount of fissionable material, such as Pu and U. The amount of fissionable material is related to the α-decay rate, which is often the key quantity for waste measurements. Neutron signatures are sometimes the only way to rapidly assay large, dense samples, but isotopic information is needed to interpret the data correctly and this adds more time to the

---

[2] There are two kinds of fission, spontaneous and induced. Spontaneous neutron emission is a primary signature of even isotopes, occurs all by itself and is random, fertile isotopes are ^{238}U, ^{238}Pu, ^{240}Pu, ^{242}Pu, 244Cm, and 252 Cf. Induced fission occurs with multiplication and is the basis for weapons and reactors. Fissile isotopes are ^{235}U, ^{239}Pu, and ^{233}U.

assay[51].

Neutron detection is done using a passive neutron counter consisting of 3 He tubes embedded in moderating material surrounding a fissioning source. They detect prompt multiple neutron emissions as coincidence neutron events. The reaction,

$$n +^3 He \longrightarrow p +^3 He + 765\,\mathrm{keV}$$

releases charge that is collected by the gas tube. Detectors produce a distribution of electrical pulses, electronics amplify the pulses and set a threshold, and converts pulses above the threshold to digital pulses, which are used to calculate the mass of fissioning isotopes[51].

Neutron coincidence counting has had wide application for international safeguards focused on verifying declared materials. Standard neutron coincidence counting provides information for singles and doubles (or totals and coincidences)[51]. Pu measurements are performed passively due to the large emission rate of neutrons from spontaneous fission. The Pu content in the SNF can be obtained by multiplying the doubles (D) or singles (S) counts of SNF by the Pu/Cm ratio. D are preferred to avoid the effect of (α,n) neutrons; however in the metal samples, (α,n) neutrons should be negligible. The Pu/Cm ratio can be determined by DA of small samples taken from the feed materials, or from the salt, or even the cathode deposit. Although DA is accurate it is more expensive and is used to verify the results of NDA that would be done more frequently[1].

2.3.1 Curium measurements study

Rinard and Menlove published an extensive study on the application of Cm measurements for safeguards at aqueous reprocessing plants[2]. Cm enters the plant through the spent fuel assemblies and leaves the plant through the waste streams. One complete batch consists of a reactor's core discharge and tanks and process lines are cleaned between batches to prevent any mixing of materials between batches.

The safeguards scheme for a plant's head-end based on Cm measurements has three key measurement points (KMPs): the Cm entering through the spent-fuel assemblies, the Cm leaving through the accountability tank, and the Cm leaving through the leached hulls. By also measuring the Cm masses in the accountability tank, plant operators and inspectors close the Cm balance for the plant's head end. Cm measurements are also made on the high-level liquid waste at the end of the process. These measurements could establish a balance between the Cm entering the vitrification facility and the Cm leaving in the canisters. The Cm amounts can be converted into Pu masses from a measurement of the Pu/Cm ratio before vitrification[2].

Neutrons are counted on the spent fuel assembly entering the facility. The neutron rate from (α,n) reactions is usually ignored as a minor contributor for LWR fuel with normal exposures and the neutron count rates are correlated with the mass of Pu using the Pu/Cm ratio. Cm is the dominant source of neutrons in each SNF assembly and in the ER salt so neutron measurements are made on Cm. The neutron balance method works is because Cm and Pu are not separated during processing, and Cm is able to serve as a surrogate for Pu. If the neutron count changes, this assumes that the amount of Cm has changed, which also assumes the amount of Pu has changed with the same ratio of Pu/Cm. Figure 2.1 shows a plot of the neutron count per Pu/Cm relationship per gram of Pu.

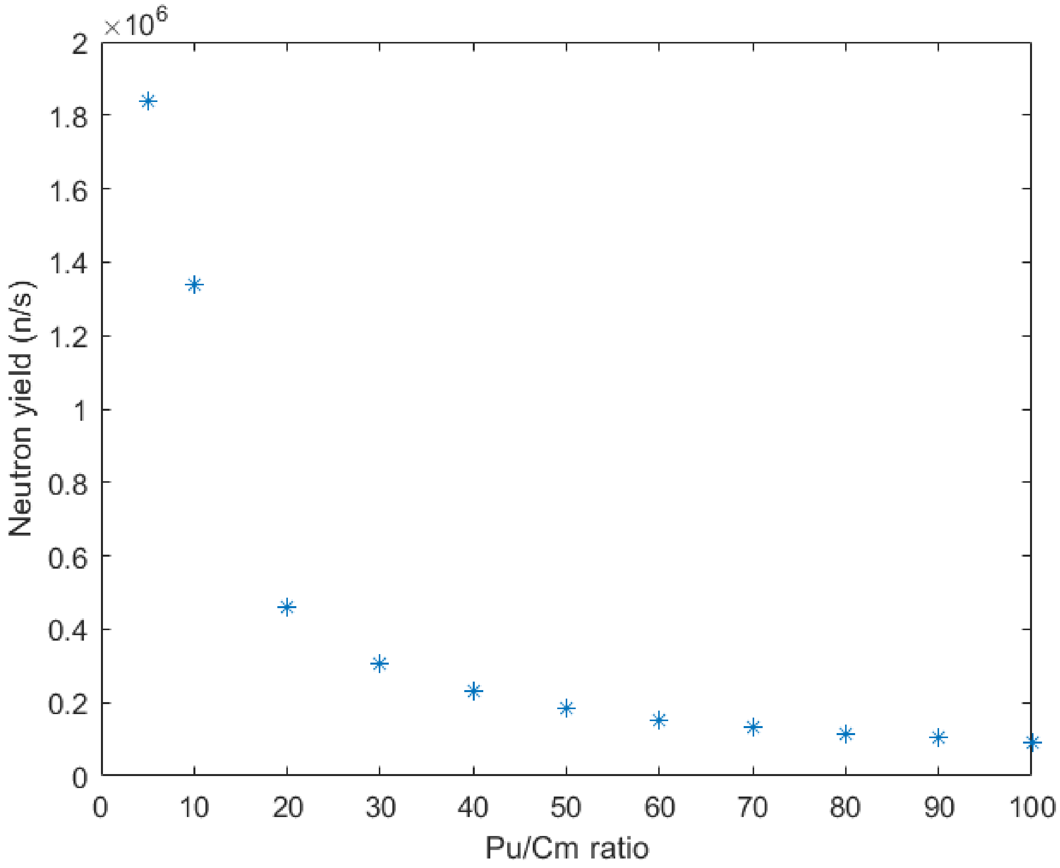

Figure 2.1: Neutron yield versus Pu/Cm ratio

Adapting this logic for the pyroprocessing facility, the neutrons coming into the ER would be measured using the following scheme:

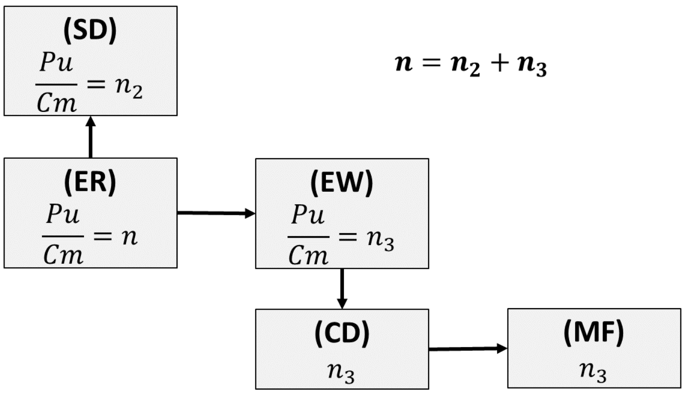

Figure 2.2: Neutrons moving through the pyroprocessing sensor network during a misuse scenario

Chapter 3

Electrochemical Deposition Background

This chapter provides the background and review on electrochemistry fundamentals and the mechanics of electrochemical deposition. The main concepts of electrochemistry, reaction kinetics, thermodynamics, and mass transport are reviewed in this chapter.

Electrochemistry combines Electrochemistry combines to describe the behavior of ions in electrochemical cells to describe the behavior of ions in electrochemical cells

3.1 Overview of Electrode Processes

Electrochemical studies are usually carried out in an electrochemical cell that contains a power supply, an anode, a cathode, and an electrolyte. The power supply drives the reaction, material is oxidized at the anode and reduced at the cathode, and the electrolyte serves as a conducting medium made of either molten salt or an aqueous solution of salts that allows the flow of ions in the cell. In electroanalytical work, a potentiostat manipulates and measures the potential and current at an electrode, which is called the working electrode (WE) and can function as either the anode or cathode depending upon the conditions imposed. A counter electrode (CE) serves as the other electrode to close the electrochemical circuit and an additional electrode called a reference electrode (RE) is commonly used to provide a stable potential to which the WE can be compared or referenced. In molten LiCl-KCl eutectic, the RE is commonly based on the silver-silver chloride (Ag|AgCl) redox couple or a chlorine ion and gas ($Cl^-|Cl_2$, (1 atm)) redox couple. Typically, electroanalytical techniques are interested in the reaction of a certain species, called an analyte, that liberates (oxidation) or consumes (reduction) electrons at the WE.

Electrochemical deposition of metals and metal oxides typically proceeds by oxidation or reduction of species in a solution. When an oxidation and a reduction are paired together in a redox reaction, electrons can flow from the oxidized species (O) to the reduced species (R).

This work is primarily concerned with the reduction of metal ions to metal in the zero valance state or the reverse reaction of oxidation from metal to a metal ion, and these reactions are generally represented by the following reaction and written so that the forward reaction is the reduction reaction:

$$\mathrm{O}^{n+} + \mathrm{ne}^- \rightleftharpoons \mathrm{R} \tag{3.1}$$

The electron flow can either be spontaneously produced by the reaction and converted into electricity, as in a galvanic cell, or it can be imposed by an outside source to make a non-spontaneous reaction proceed, as in an electrolytic cell[52]. Electrorefining is a process by which materials, usually metals, are purified by means of an electrolytic cell. The anode is the impure metal (SNF) and the cathode is a very pure sample of the metal (U)[53].

Figure 3.1 shows the cell schematic where both electrodes are placed in the same solution of a LiCl−KCl eutectic molten salt electrolyte connected by a power source. Current is defined as the flow of positive charges and moves in a direction opposite to the electrons in the external circuit. During operation, anions move to the positive anode, lose their electrons and oxidize to atoms. Cations move toward the negative cathode, gain electrons and reduce to atoms.

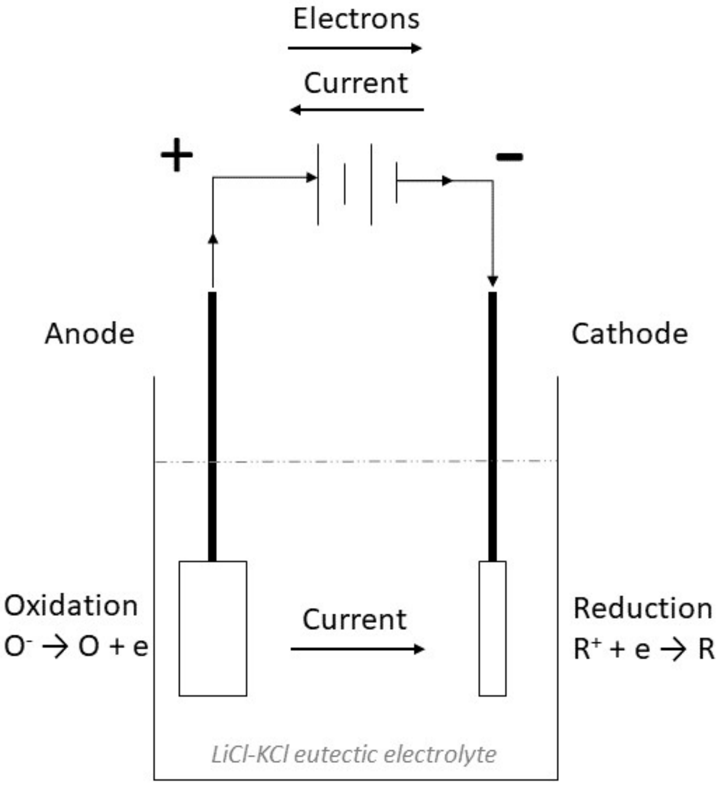

Figure 3.1: Electrolytic cell schematic with two electrodes attached to a power supply immersed in LiCl−KCl molten salt electrolyte.

Two main factors influence the selective redox reactions of a species at the electrode, the standard reduction/electrode potential (E^0) of the species and the concentration of the species in the electrolyte. If there is more than one reducible species in the electrolyte, the species with the more positive E^0 is preferentially reduced at the cathode. At the anode, the species with the more negative E^0 is preferentially oxidized. The increase of concentration of an ion in the electrolyte tends to promote its discharge.

3.2 Reaction Kinetics

The Butler-Volmer equation describes the kinetics of electrochemical reactions by relating the current density to the surface area and potential of the electrode. Most rate constants for reactions, k, have an Arrhenius relationship with temperature where ln(k) varies as 1/T, described by the following equation,

$$k = Ae^{-E_a/RT} \tag{3.2}$$

If the reaction is occurring in a condensed phase, then the activation energy, E$_a$, can be related to a standard Gibb's free energy of activation that can be related to potential, as expressed in the forward rate relationship (3.3) and the backwards rate relationship (3.4):

$$k_f = k^0 \text{exp}\left[-\frac{\alpha nF}{RT}(E - E^{0'})\right] \tag{3.3}$$

$$k_b = k^0 \text{exp}\left[\frac{(1-\alpha)nF}{RT}(E - E^{0'})\right] \tag{3.4}$$

The amount of the potential that induces the reduction reaction is referred to as the transfer coefficient, α, and is often assumed to be 0.5. The standard rate constant (k^0) is the forward and backward rate constants at equilibrium under the special conditions that $E = E^{0'}$ and the bulk concentrations are equal ($C_O^b = C_R^b$).

The reaction rate for a single-step reaction is described as,

$$r = k_f C_{O^{n+}} - k_b C_{R^{P+}} \tag{3.5}$$

If (3.3) and (3.4) are substituted into (3.5) and Faraday's law is applied ($I = nFAr$), then the faradaic current related to the reaction in (3.1) is given by (3.6)

$$I = nFAk^0 \left(C_O \text{exp} \left[-\frac{\alpha nF}{RT}(E - E^{0'}) \right] - C_R \text{exp} \left[\frac{(1-\alpha)nF}{RT}(E - E^{0'}) \right] \right) \tag{3.6}$$

Introducing the term, exchange current density, i_0, simplifies (3.6), by evaluating it at equilibrium (i.e., $I = 0$) and results in the equation below,

$$i_0 = nFAk^0 (C_O^b)^{1-\alpha} (C_R^b)^{\alpha} \tag{3.7}$$

Substituting (3.7) into (3.6) and multiplying by negative one yields the *current-overpotential* relationship[54],

$$I = i_0 \left(\frac{C_R}{C_R^b} \text{exp} \left[-\frac{(1-\alpha)nF}{RT} \eta \right] - \frac{C_O}{C_O^b} \text{exp} \left[\frac{\alpha nF}{RT} \eta \right] \right) \tag{3.8}$$

The first term describes the cathodic component current at any potential, and the second gives the anodic contribution. If the surface and bulk concentrations are assumed to be equal, (3.8) simplifies to the more common Butler-Volmer equation. The overpotential, η, is defined as the additional potential needed on top of the equilibrium potential to drive the reaction at a specific rate,

$$\eta = E - E^{0'} + \frac{RT}{nF} ln \left(\frac{C_R^b}{C_O^b} \right) \tag{3.9}$$

3.3 Thermodynamics

Thermodynamics deals with equilibrium cell potential and how differences in potentials relate to free energy changes in an electrochemical system. The probability of a particular reaction occurring is determined by the change in Gibbs free energy, ΔG, described by the following equation,

$$\Delta G = \Delta G^0 + RTln(Q) \tag{3.10}$$

which relates the standard-state free energy of a reaction with the free energy of a reaction at any moment in time during the reaction. ΔG is the free energy at any moment, ΔG^0 is the standard-state free energy, R is the ideal gas constant, T is the temperature in Kelvin, and ln(Q) is the natural log of the reaction quotient at that moment in time.

The free energy of a reaction is related to the cell potential and charge passed in a reaction such that,

$$\Delta G = -nFE \tag{3.11}$$

The Gibbs free energy equation can be written as,

$$nFE = nFE^0 - RTln(Q) \tag{3.12}$$

which can be rearranged to yield the Nernst equation.

$$E = E^0 - \frac{RT}{nF}ln(Q) \tag{3.13}$$

The Nernst equation describes the relationship between the equilibrium potential of a redox couple and the concentration.

The Nernst equation is often written in terms concentrations, C_O and C_R that are adjacent to the surface of the electrode.

$$E = E^{0'} + \frac{RT}{nF} ln \frac{C_0}{C_R} \tag{3.14}$$

$E^{0'}$ is the redox potential for the couple involving O and R, C_O is the concentration of the oxidized half of the couple, and C_R is the concentration of the reduced half.

3.4 Mass Transport

The consumption of species during the reduction at the working electrode gives rise to a concentration gradient in the solution outside the electrode surface. The kinetic expression in (3.8) have two separate terms for the concentrations in the bulk and at the electrode surface illustrating that the conditions are different at the surface of an electrode than in the bulk solution. These differences are the result of mass transport mechanisms, namely diffusion, convection, and migration. All of these mechanisms are encapsulated in the flux (J) of an ion.

The flux is driven by the difference in the electrochemical potential, $\bar{\mu}$, which is related to the chemical potential, μ.

$$\bar{\mu} = \mu^0 + RTln(a) + nF\phi \tag{3.15}$$

The last term accounts for electrical properties of the ion's environment and is related to the charge of the ion and absolute potential, ϕ, of the ion's location. Ions in a solution will move or generate a flux to relieve gradients in the electrochemical potential. Molar flux can be calculated from the gradient of electrochemical potential and any convective flow.

$$J = -\frac{CD}{RT}\nabla\bar{\mu} + C\nu \tag{3.16}$$

Substituting (3.15) into (3.16) yields this general equation,

$$J = -CD\nabla ln(a) - CD\frac{nF}{RT}\nabla\phi + C\nu \tag{3.17}$$

By introducing a few assumptions to (3.17), it simplifies to the Nernst-Planck equation,

$$J = -D\frac{dC}{dx} - CD\frac{nF}{RT}\frac{d\phi}{dx} + C\nu \tag{3.18}$$

The assumptions in (3.18) include one-dimensional transport and the equivalence of activity and concentration. The three terms in equations (3.17) and (3.18) represent the contributions of diffusion, migration and convection, respectively. Using Faraday's law ($I = nFAj$), the flux can be related to current.

Electrochemical systems are frequently designed so that one or more of the contributions to mass transfer are negligible. The migration component can be reduced by the addition of an inert electrolyte at a concentration much larger than that of the electroactive species. Supporting electrolytes can also reduce the effects of ohmic drop in the solution. In addition, the migration term is less significant at low currents due to a weaker electric field (i.e., lower overpotentials). Convection can be avoided by preventing stirring and vibrations in the electrochemical cell. If the convection and migration terms are neglected, then the Nernst-Planck equation reduces to Fick's first law, which states that material will diffuse from a region of high concentration to one of low concentration,

$$J = \frac{dN}{Adt} = -D\frac{dC}{dx} \tag{3.19}$$

Fick's second law is derived from the first law and is the origin of almost every electroanalytical expression derivation,

$$\frac{dC}{dt} = D\frac{d^2C}{dx^2} \tag{3.20}$$

This work follows the conventional assumption that the migration and convection terms were reduced since reactions occurred in a large inert electrolyte and stirring was eliminated.

3.5 Electrochemical Deposition

Electrochemical deposition, or electrodeposition, also known as electroplating, is the process of depositing material onto a conducting surface from an electrolyte. This technique is commonly used to apply thin films of material to the surface of an object to change its external properties such as to increase corrosion protection, increase abrasion resistance, improve decorative quality, or simply to deposit a layer which is part of a more complicated device.

An example of electrolytic reduction is illustrated in Figure 3.2. At the anode Pu metal is oxidized into the LiCl−KCl eutectic electrolyte forming Pu^{3+} cations. The half reaction $Pu^{3+} + 3\,e^{-} \longrightarrow Pu_{(s)}$ occurring at the cathode.

The electrolysis of species can be performed using a constant current forced through the electrochemical cell, while the electric potential is monitored. Alternatively, a desired potential can be chosen, which is then maintained by the potentiostat while the current

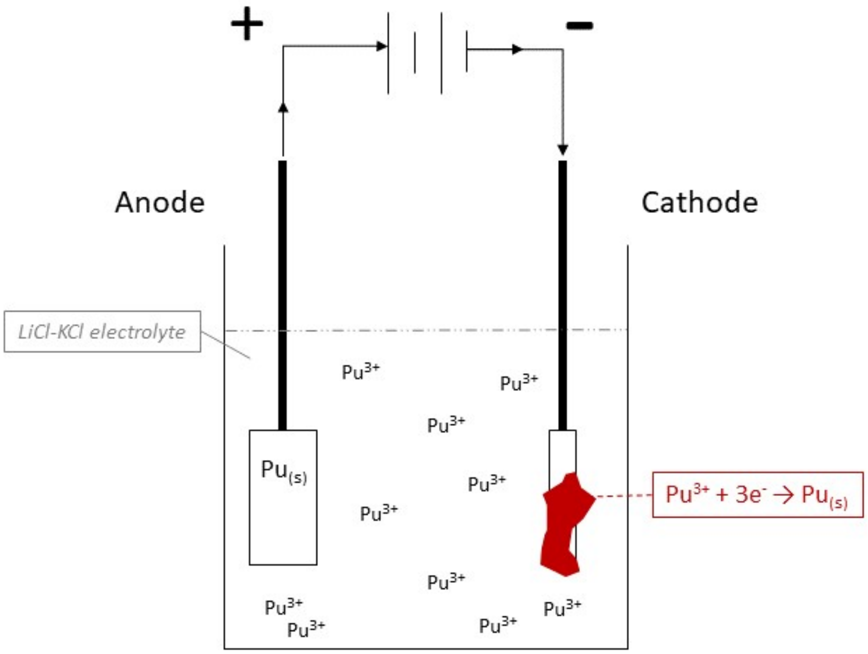

Figure 3.2: Electrolytic cell schematic of the half reaction of Pu^{3+} cations reducing on the cathode and forming a Pu metal deposit.

used to maintain that potential is monitored.

3.5.1 Controlled current

Constant current electrolysis is based on Faraday's law, which relates the total charge passed in an experiment (Q) to the number of molecules electrolyzed, N, and the number of electrons involved in the electron transfer reaction, n[55],

$$Q = nFN \tag{3.21}$$

where F is Faraday's constant.

When an electrochemical experiment is performed using a constant current, the potential shifts to the value required to maintain that current. Under conditions of mass transfer control (i.e. when the kinetics of the electrode reaction does not limit the current), the potential shifts to the redox potential of another electron transfer reaction when the concentration of first electroactive species at the electrode surface is reduced to zero. If no other analyte has been added to the solution, the second electron transfer reaction will involve reduction of the electrolyte, which will result in a large shift in potential.

3.5.2 Controlled potential

In a controlled potential experiment, the potential is set at a constant value sufficiently negative to cause reduction (measured by e.g., cyclic voltammetry (CV)) and is maintained at this value until only the reduced species is present in solution. Farady's law can be used to estimate the amount of species reduced on the cathode.

3.5.3 Electroanalytical Methods

Electroanalytical methods are techniques that investigate the behavior of an ion of interest called an analyte by manipulating potential or current and measuring the other. Four terms are frequently used when describing electroanalytical techniques: amperometry, potentiometry, voltammetry, and coulometry. Amperometry controls the potential, usually holding it steady at one setting, and measures the current. It can be considered a subclass of voltammetry. Potentiometry measures potential while controlling the current. Voltammetry, like amperometry, measures current and controls potential, but voltammetric techniques involve more than fixing the potential at a set value. It can include scanning the potential or a series of potential steps with a certain pattern. Coulometry measures the charge under potential controlled conditions and can affect the bulk characteristics of the electrochemical solution. The electroanalytical technique of interest in this project is open-circuit potentiometry (OCP).

There are generally three different potentials of interest when studying the electrochemical methods, the standard cell potential E^0, which is the theoretical Nernst potential for a redox reaction when the activities of all the reactants and products are 1, the equilibrium potential $E^{0'}$ which is the potential of the cell taking into account the activities according to the Nernst equation, and the OCP which is the experimental potential observed when no current is externally driving the the system[52].

Open-circuit potentiometry

The OCP is measured with a high impedance voltmeter placed across the cell during equilibrium conditions. When a redox couple is present at each electrode and there are no contributions from liquid junctions, the OCP is also the equilibrium potential[52]. The equilibrium potential between a metal and a solution of its ions is given by the Nernst equation (3.13). In the case of metal deposition, some metal needs to be initially present on the electrode in order to record its open circuit potential with its ion. This could be done by using an electrode made of the metal of interest or by predepositing some metal on an inert electrode, then enforcing an open-circuit. The measured potential at open-circuit should vary logarithmically with concentration or mole fraction. If this behavior can be verified for molten salt mixtures of interest, then it could be used to determine concentration[56].

The OCP may show contributions from different processes, therefore it doesn't necessarily correspond to any fixed equilibrium potential value and it can change over time as the conditions in the cell change, which would make OCP measurements very specific to each electrochemical system.

Cyclic voltammetry

Cyclic voltammetry is an electrochemical technique that measures the current that develops in an electrochemical cell under conditions where voltage is in excess of that predicted by the Nernst equation. CV is performed by cycling the potential of a working electrode and measuring the resulting current as the different species in the electrolyte solution reduce and oxidize. By applying a range of voltage, current generated in the system due to the voltage is plotted on the graph. Depending on what is already known about a given system, the concentration, the diffusion coefficient, the number of electrons per molecule of analyte oxidized or reduced, and the redox potential for the analyte could be determined from a single experiment. For example, when the scan rate, area of electrodes, and diffusion coefficients are fixed in the system the current information can reflect the concentration of input elements. However, when there are multiple elements in the system the CV diagrams tend to overlap[57].

Chapter 4

Modeling and Simulations Background

There is a long history of using computer simulations to study pyroprocessing and the ER. Simulations are useful for understanding complex systems that are not easily accessible, expensive to operate, or only theoretical. Extreme conditions and off-normal events can be explored in simulations without destroying existing equipment or stopping regular operation of industrial facilities. Computer simulations are used in this research to explore off-normal operating conditions of a process in a facility that is still in the research and development phase.

The chapter provides a review of ER modeling through the years, work done on failure mode modeling, and provides an overview of how ERAD works.

4.1 Review of electrorefining modeling work

Many models have been developed over the years to describe the ER process. Initially the models were relatively simple and were based on the concepts of thermodynamics and diffusion. Over time the models have become more advanced to handle other phenomena.

An ER model based on the equilibrium of the reactions at the electrode/salt interface, for example,

$$UCl_3(salt) + Pu(electrode) \leftrightarrow PuCl_3(salt) + U(electrode) \tag{4.1}$$

was first developed by Johnson at at Argonne National Lab (ANL)[58], and improved by Nawada and Bhat[59]. The model was reanalyzed by Ghosh et al.[60], who claimed that the simulation model can treat 16 possible conditions of U-Pu alloy electrorefining that could be envisaged with respect to solubility of U and Pu at the liquid anode and cathode. However, the thermodynamic model does not capture the kinetic features related to the evolution of the variables, for example the partial current of each element.

The majority of published work on ER modeling has been based on the Mark-IV ER design to further enhance the understanding of the fundamental chemical and physical processes[10, 61–65]. The authors claimed that the model reduced the guessed parameters to only one. However, the model led to some unreasonable results because the over potential was not used properly. The diffusion controlled model, which can study the process kinetics, was first developed by Kobayashi and Tokiwai[66]. This model was improved to include multicomponent electrorefining processes[67]. Comparisons between the modeling results and experimental data showed that the model had high accuracy. However, the model did have some deficiencies. For example, the activity coefficients of all the elements considered in the model were assumed to have a value of 1. Further, the model used the same thickness for the mass transfer boundary at the salt/electrode interface for all elements and cases. Considering that the thickness will change when the flow conditions of the molten salt and liquid electrodes are changed, this assumption is not reasonable.

These models determined the segregation of species between phases in the ER but did not provide information regarding process dynamics such as electrode potentials or cell current. Both the kinetics of electron transfer and the mass-transport of ions in molten salt affect the partitioning rates of elements in the ER. These time-dependent effects are captured in the code, REFIN, developed at Seoul National University (SNU)[68]. Iizuka et al. developed a model which captures the dynamic behavior of U, Pu and Zr during electrorefining, but only for anodic dissolution[69].

Two and three-dimensional models have been developed by coupling computational fluid dynamics (CFD) model with REFIN to model electrochemical reactions and behavior, and current and potential distributions at and near the electrode surfaces[62, 68, 70]. Li uses a three-dimensional CFD model which calls a FORTRAN model to calculate and set the boundary conditions based on electrochemical calculations. The model accounts for four species (U, Pu, Nd, and Zr) and calculates the current density at the electrode-salt and cadmium pool-salt interfaces[71].

Zhang developed a general model to predict the critical current or bulk uranium concentration at which co-deposition of Pu begins in an ER at LANL. The model included mass transfer kinetics and electrochemical kinetics at the electrode surface to show the evolution and distribution of the concentration partial currents of each element in the system as functions of time and operating conditions. The effects of flow dynamics and the activity coefficients of the elements at the electrodes and in the molten salt are incorporated into the model simulations[72–74].

ERAD is another general ER model that can be applied to various ER configurations by adjusting various geometric parameters such as electrode areas and diffusion boundary layer thicknesses[75, 76]. ERAD was developed by modifying REFIN to dissolve SNF from a solid anode, to include solubility limits at the anode surface, and the geometry of the anode was altered to account for a porous layer of noble metals, the differential equation solver was replaced, and a package was inserted to account for fast reactions occurring before the application of an external power source[69, 77].

Modeling Failure Modes

The study of failure modes was developed in the 1950s by reliability engineers to study problems that might arise from malfunctions of military systems. They used Failure mode and effects analysis (FMEA) which was one of the first highly structured, systematic techniques for failure analysis. This concept was adopted and coupled with SBS to study failure modes in the pyroprocessing system with the use of computer models and simulations[78].

Signature based safeguards involves identifying anomalous scenarios, determining which PM measurement signatures would arise (i.e. temperature, electric potential, stir rate, etc.), and detecting them using a network of sensors[24]. Current and past research in SBS involves the identification of failure modes and modeling their detection computationally.

Failure modes are significant because they can lead to the transport of materials to unexpected locations in the material flow sheet[12, 13, 79]. For example, a cathode that is not submerged properly in the salt bath in the ER could result in codeposition of Pu at that cathode resulting in Pu being erroneously consolidated within the final fuel product[13].

Previous simulations of identified failure modes and their detection have been performed using the coupling of two computer codes, ERAD and Monte Carlo Neutron Transport (MCNP). ERAD was used to produce a simulated cathode product under off-normal operating conditions. MCNP modeled a JCC-31 High Level Neutron Coincidence Counter (HLNCC). The cathode product was analyzed as a cylindrical metal ingot by the HLNCC for both singles and doubles rates. In the cases where Pu codeposited on the cathode, there was a significant increase in neutron counts and calculated potential by ERAD[13].

To further develop SBS and evaluate the effectiveness of the network of sensors and their ability to detect off-normal operations, the pyroprocessing facility must be modeled and analyzed at the system level integrating previous information from subsystem models such as the coupled codes used in previous work. System models allow the researcher to determine the effectiveness of a developed safeguards system in the context of meeting IAEA goals.

Currently, two major pyroprocessing safeguards system models have been developed. The first is a code solely for the analysis of PM safeguards methods developed in ExtendSim by INL[23]. This model was developed specifically to test sensor networks for PM applications, in particular SBS. The second model is known as the Echem SSPM developed in SimuLink[16]. This model calculates the material balance and its associated uncertainties. It also allows for the integration of PM technologies within the model; however, the focus of the work has been on determining the NMA measurement uncertainty required to reach the IAEA target uncertainty for the material balance.

The issue that arises with both of these models is that the unit operations throughout the facility such as the ER and the salt waste purification process are based off of well-established assumptions that only accurately reflect transport during normal operation and do not allow for the possibility of failure modes upsetting the material balance[16, 23].

Identification of off-normal operational scenarios begins by understanding the fundamental aspects of each unit operation. Knowing how the unit operation works from a fundamental level leads to an understanding of how the process can be changed in such a way that leads to safeguards significant events. These scenarios will occur under specific operating conditions and those operating conditions can be monitored with specific PM technology. Knowing which conditions will lead to safeguards significant events allows for an SBS methodology to be built.

Similar to past failure mode evaluation efforts, ERAD is used in this work to examine an incomplete salt-cleanup failure mode and how PM techniques can be used to detect safeguards significant events.

4.2 Enhanced REFIN with Anodic Dissolution

ERAD is a FORTRAN computer code chosen to carry out the electrodeposition simulations for this work. ERAD depicts anodic dissolution of SNF, mass transport effects in molten salt electrolytes, and cathodic deposition. ERAD has the capability to account for up to 10 elements including those present in the eutectic LiC-KCl melt. ERAD is spatially one-dimensional and it assumes a uniform potential distribution and current density at the surface of the electrodes. ERAD performs well in the geometric configuration of concentric cylinders[80]. Despite the availability of three-dimensional codes, a detailed one-dimensional model is the best way to quickly test assumptions on electrochemical behavior, perform fits to data, and effectively model the mass transfer between the anode and cathode without heavy computational burden.

ERAD's calculations were compared to experimental data from CRIEPI[81]. ERAD demonstrated good agreement in electrode potentials, but it over-predicted the rate of Pu transport and under-predicted rate of U transport. In addition, the time of Zr dissolution commencement did not agree with the experimental data. Further validation work was performed in which ERAD's simulation results compared favorably to several U and Pu cyclic voltammograms from open literature[75, 82]. The electrorefining feature has also been benchmarked with gram-scale ER tests[75, 81]. Similar to this research, ERAD was successfully used in other studies of multi-component electrochemical systems for SBS development[56, 77–79, 79, 82].

Cumberland et al. [80, 83] provides great detail on how ERAD was made and how it works and a concise overview is provided here. When ERAD first starts, it is provided with operating conditions and concentrations of every species inside the anode, electrolyte and cathode.

ERAD uses the fundamental equations of electrochemistry (3.1) to calculate mass transfer in the diffusion layers and concentrations at electrode and electrolyte surfaces by simulating material moving through different phases of the ER. Active elements in the SNF diffuse through the bulk anode and the depleted, porous layer consisting of noble metals to the anode surface where they are oxidized into the anode diffusion layer. The oxidized elements diffuse to the bulk solution which is well-mixed and assumed to be homogenous. Then the oxidized elements diffuse through the cathode diffusion layer and are reduced at the cathode surface.

For chemical reactions at electrodes, ERAD uses the Nernst equation, Eq. 3.13, to account for thermodynamics of electrochemical reactions. In multi-reaction systems the the electrode's zero current potential will not be the equilibrium potential for any given element. Also, the activity coefficient for molten salt is lumped in with the standard potentials.

Reaction kinetics are accounted for by the Butler-Volmer equation (3.8). At the electrode surfaces, the rate of mass transfer into and out of the mesh cells depends on the reaction rates of the various electrochemical reactions and the reaction rate is dependent on the current density created by each reaction. Those current densities are functions of electrode potential (E_{el}) as described by (3.8) describing the current density of reaction r:

$$i_r = B_r(\eta_r, \vec{y}) \tag{4.2}$$

$\vec{y}$ is the vector of concentrations or inventories at every mesh cell. The overpotential (η_r) is computed from the electrode potential using a modified form of the Nernst equation,

$$\eta_r = N_r(E_{el}, \vec{y}) \tag{4.3}$$

The current densities must sum to the operating current density specified by the user. When all equations are combined, the total current density I_{tot} is dependent on species concentrations and electrode potential.

$$I_{tot} = \sum B_r(\vec{y}, N_r(E_{el}, \vec{y})) \tag{4.4}$$

The potential gradient $\frac{\partial \phi}{\partial x}$ is also a function of concentration and current density. It is defined by Equation 4.5

$$\frac{\partial \phi}{\partial x} = -\frac{I_{tot} + \sum(D_i n_i F \frac{\partial y_i}{\partial x})}{\sum(\frac{F^2 n_i^2 D_i}{RT} y_i)} \tag{4.5}$$

Equation 4.5 is derived by summing the total mass fluxes given in Equation 3.18 equating it to the total electrical current density (I_{tot}) through the salt, and applying the electroneutrality condition.

Mass transfer in the diffusion layers adjacent to the electrodes is governed by the Nernst-Planck equation written for one-dimensional mass transfer along the x-axis in (3.18). ERAD uses the differential equation solver package, DLSODE, using the backwards differentiation method to solve (3.18).

Chapter 5

Experimental Methods

To streamline the experimental procedures, the experimental methods and techniques used in this research were based on previous work in this area[56]. The methods were largely developed and tested at the University of Utah's department of metallurgical engineering, where these methods were fined tuned and proven to be accurate and reliable.

For the most part, procedures and methods could be easily adapted to conduct these studies, but some new designs were implemented as well. This chapter provides information on the experiments conducted for this research. Details on the equipment and design of the electrochemical cell are provided. The chemicals used and how the surrogates were selected are also explained. This chapter then describes how the samples were collected and analyzed at the end of each experiment. And finally, this chapter details the test matrix and experimental procedures followed to conduct the experiments in a consistent manner.

5.1 Equipment and Design

The electrochemical studies in this work were carried out in a PureLab HE glovebox obtained from Innovative Technologies, as pictured in Fig. 5.1. Ultra-high purity argon was used as the working gas. The glovebox, Fig. 5.1, was equipped with a gas purification module to scrub out O_2 and H_2O, which were maintained below 1 pmm.

Figure 5.1: Photograph of glovebox used for electrochemical tests

A potentiostat is a device used to keep a WE at a desired potential with respect to a RE. This is done by passing a current from the WE to a CE. The potentiostat used in this work was an Autolab PGSTAT302N potentiostat/galvanostat run by a PC through Metrohm Autolab B.V.'s NOVA 1.11.2 commercial sofware.

Connections were drilled and installed into the side of the glovebox to connect the leads coming from the electrochemical cell to the back of the glovebox and out to the poten-

(a) Brackets used to connect the wire leads

(b) Connections for the potentiostat

(c) Connections going into the glovebox to the electrochemical cell

Figure 5.2: Photographs of the potentiostat lead configuration

tiostat as shown in Fig. 5.2.

5.1.1 Electrochemical Cell

The electrochemical cell consisted of a large alumina crucible inserted into a graphite crucible that sat in a Kerr Lab Large Automatic Maxi Electro-Melt™Largest capacity hand melter. An electronic controller with digital display held the temperature at 773 K. The temperature was set to 573 K and then slowly increased to 773 K over the course of two hours to slowly melt the salt and not crack the alumina crucible. The working temperatures were measured with a Omega KQXL-116G-12 thermocouple. Figure 5.3 shows the three-electrode cell used for all measurements.

The RE consisted of a closed-end mullite tube, in which 5-mole % of AgCl (Alfa Aesar 95%) was placed. An Ag wire (Alfa Aesar 99.999%) of 1 mm diameter served as electrical contact, as well as to establish the inner Ag|AgCl reference. Unless otherwise stated, all the potentials are referred to this reference. Figure 5.4 shows the RE being put together.

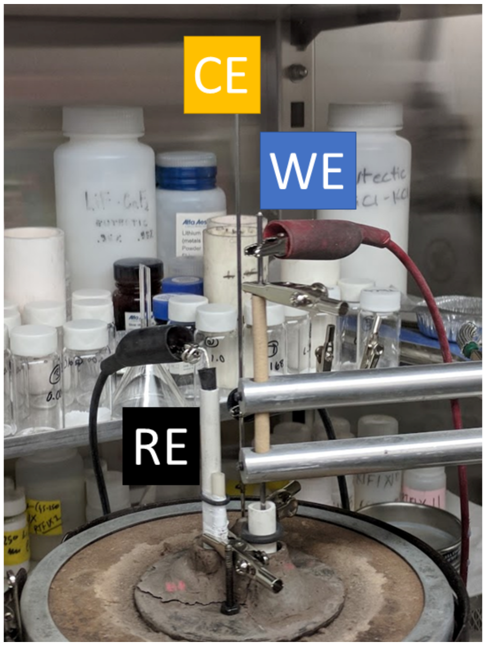

Figure 5.3: Photograph of the three electrode setup

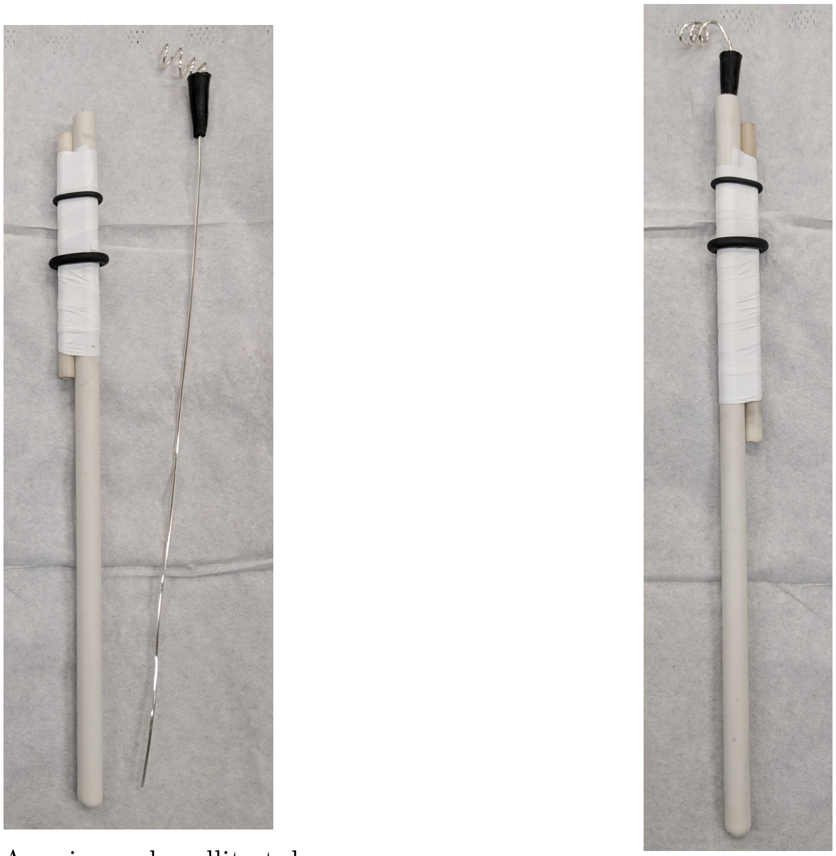

(a) Ag wire and mullite tube

(b) Complete RE

Figure 5.4: Photograph of the 5-mol.% Ag|AgCl reference electrode

Tungsten rods (Alfa Aesar 99.95%) of 2.0 mm diameter were used for the WE and CE. The lower end of the electrodes were polished thoroughly by using SiC paper to increase the surface roughness and then cleaned in HNO_3 and dried in the oven at about 120 °C. Polishing the electrodes ensures better adherence of the electrodeposited metal on the surface of the cathode and removes any oxide or contaminant layer formed on the surface.

For electrodeposition experiments the anode, shown in Fig. 5.5, was a 6.35 mm diameter Tb metal rod (Beijing Goodwill Metal Technology CO LTD, 99.9%) and the cathode was a W rod (Alfa Aesar 99.95%) of 2.0 mm diameter.

Figure 5.5: Photograph of Tb rod anode secured in a custom Swagelok

5.2 Experiment Chemicals

A surrogate system using a $TbCl_3-GdCl_3-LiCl-KCl$ salt mixture was chosen to conduct a series of Tb and Gd metal electrodeposition experiments. The electrolytic bath was a mixture of $LiCl-KCl$ (Sigma-Aldrich, 99.99%), $TbCl_3$ (Sigma-Aldrich, 99.9% metal basis), and varying concentrations of $GdCl_3$ (Sigma-Aldrich, 99.99% metal basis).

The experiments are designed to reduce Tb on a W cathode with the same potential and with each subsequent experiment, increase the concentration of Gd^{3+} in the electrolyte in order to test whether or not Gd metal codeposits on the cathode and with what Tb/Gd ratio. Tb was used as the surrogate for Pu, and Gd served as the Cm surrogate.

5.2.1 Surrogate selection

The behavior of the Pu and Cm in the molten salt system can be mirrored via surrogate elements exhibiting a similar chemical potential difference. Several candidate surrogates for Pu and Cm were reviewed[84]. The electrochemical parameters of interest for choosing the appropriate surrogates were the valance state of the ion undergoing the reaction and the reduction potential difference of the two elements.

Studies show that Pu^{3+} is reduced to Pu metal by a single step mechanism in LiCl-KCl eutectic,

$$Pu^{3+} + 3\,\mathrm{e}^- \rightarrow Pu_s$$

and the apparent standard potential is -2.77 V vs. $Cl_2|Cl^-$[49]. Studies also reveal that Cm^{3+} is reduced to Cm metal in LiCl-KCl eutectic in a single step,

$$Cm^{3+} + 3\,\mathrm{e}^- \rightarrow Cm_s$$

with an apparent standard potential is -2.86 V vs. $Cl_2|Cl^-$[50, 85].

Of the candidates for surrogates, Tb and Gd matched the best. Electrodeposition of Tb and Gd at the inert electrode takes place in a single electrochemical step with a global

Table 5.1: Surrogate materials and their standard potentials

Redox Couple	**Potential (V)**	**Surrogate Redox Couple**	**Potential (V)**
Pu(III)/Pu(0)	-2.77[49]	Tb(III)/Tb(0)	-2.78[86]
Cm(III)/Cm(0)	-2.86[50]	Gd(III)/Gd(0)	-2.95[87]
%Δ	4.0	%Δ	6.0

exchange of three electrons[86–88]. The reactions are as follow:

$$Tb^{3+} + 3\,\mathrm{e}^- \rightarrow Tb_s$$

$$Gd^{3+} + 3\,\mathrm{e}^- \rightarrow Gd_s$$

Tb and Gd were chosen based on their differences in reduction potentials, their valence state, their one-step reduction process, and their availability. The reduction potentials of Pu, Cm, Tb, and Gd are compared in Tab. 5.1.

Table 5.1 displays the potentials and the percent change between Pu and Cm and Tb and Gd. They are not perfectly aligned, but for the purpose of this experiment they are suitable. Because the percent difference, %Δ, is larger for Tb and Gd, if codeposition occurs, then it will likely occur for Pu and Cm. The more positive electroactive species is preferentially reduced on the cathode, and Cm is more positive than Gd. If electrolyte concentration conditions allow for Gd to reduce, then it can be assumed Cm will likely reduce under the same conditions.

Working with Pu and Cm discussion

The experimental component of this dissertation tests the working assumption that Cm and Pu behave similarly during the electrorefining process. The INL tests concluded that to examine this hypothesis directly, there needs to be a lot of LWR spent fuel to get enough Cm for it to be detected in the salt and at the cathode with inductively coupled plasma mass spectrometry (ICP-MS) or Inductively coupled plasma optical emission spectrometry (ICP-OES)[9]. Working with that much material presents a variety of problems for basic research and development (R&D) experimental work. First, a large facility with well shielded hot cells would be required. The hot cells would need to be fully automated and have either large windows to see inside, or a highly detailed digital interface to be able to move material and electrodes in and out of the electrochemical cell easily and precisely. Due to the cost and scarcity of the required chemicals alone, it would be difficult to conduct fundamental R&D experiments in such an environment because there would be little room for error. The Cm contamination alone would make it impossible to make easy changes to the electrochemical cell design. The electrodes would have to be disposed of to avoid contamination in successive experiments. It is inevitable that electrodes (particularly the RE) or the crucible containing the molten salt will break during the course of the experimental campaign. Such an event would cost hundred of dollars in resources and time lost if and when this would offer. So much would have to be known beforehand to set up the cell perfectly, to know exactly how much salt was being added to each run and how it will happen. Such precise level of detail can really only be gained from conducting multiple experiments. Such a system would really only allow for one perfect experiment, and it is not clear that is possible to achieve.

5.3 Test Matrix

This work examines electrodeposition under different electrolyte concentrations using the constant potential method. To select the appropriate potential for the electrodeposition tests, single-analyte molten salt mixtures were first analyzed using CV. which scans the electrode over a range of potential values at a certain rate and measures the current response. Two electrolyte mixtures were made to measure the potential at which Tb and Gd react, one contained 1 wt.% Tb^{3+} in $TbCl_3-LiCl-KCl$ and the second one contained

1 wt.% Gd^{3+} in $GdCl_3-LiCl-KCl$. The CVs are shown in the same plot in Figure 5.6.

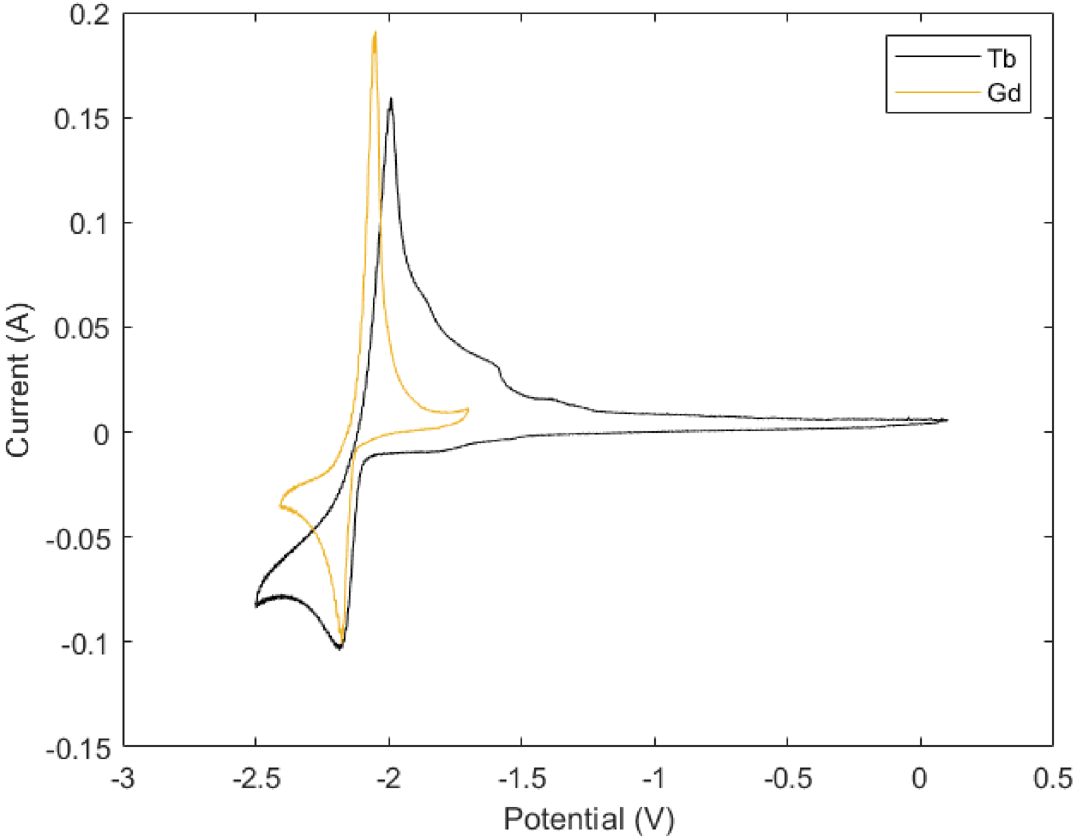

Figure 5.6: CVs of 1 wt.% Tb and 1 wt.% Gd at 200 mV/s, T = 773 K, 5-mol.% Ag|AgCl RE

The reduction potentials overlap but Tb^{3+} starts to reduce a little before Gd^{3+}. To ensure reduction of both species, a constant potential of -2.13 V was chosen. It is sufficiently negative for Tb^{3+} to be reduced and the current is considered to be limited by the mass transfer of Tb^{3+} and Gd^{3+} ions to the W electrode surface.

The electrolysis was conducted until the total electric charge reached approximately 365 C, which was approximated as the equivalent of 200 mg of metal liberated according to Faraday's law of electrolysis. A total of 0.5 g of Tb^{3+} (158.93 g/mol) was dissolved in $LiCl-KCl$ eutectic. The Tb^{3+} concentration was held constant at 1.0 wt.% for all runs

Table 5.2: Test matrix of Tb-Gd electrodeposition experiments

Test No.	**Tb:Gd**	**Tb^{3+}(wt.%)**	**Gd^{3+}(wt.%)**
1	undefined	1.0	0
2	100:1	1.0	0.01
3	75:1	1.0	0.013
4	50:1	1.0	0.02
5	25:1	1.0	0.04
6	10:1	1.0	0.10
7	5:1	1.0	0.20
8	1:1	1.0	1.0

and Gd^{3+} was added to the electrolyte salt mixture for each experiment. The test matrix for the electrodeposition experiments is displayed in Table 5.2 showing the Tb/Gd ratio and the weight percents of Tb^{3+} and Gd^{3+} for each test. The weight percents are based on mass measurements.

The experiments tested the codeposition of Tb and Gd using eight different ratios of Tb^{3+} to Gd^{3+} in the electrolyte salt. All tests were performed at 773 K. Two electrodeposition experiments were performed for tests 1, 5 and 8 to test reproducibility utilizing two sample analysis methods, ICP-OES and SEM-EDS.

5.4 Sample Analysis

Molten salt samples were collected by dipping a threaded rod in the molten salt and immediately removing it. The frozen salt was collected in a bottle and weighed. The cathode deposit samples were slowly removed from the furnace, carefully weighed and placed in plastic bags. All samples were weighed using a Mettler Toledo ML204 New-Classic Analytical Balance equipped with a draft shield, a capacity of 220 g, and 0.0001 g readability.

The W rod cathode and mullite tube were removed from the electrochemical cell when the constant potential runs reached a total charge of approximately 365 C. Samples of the electrolyte salt were taken after each experiment by dipping a threaded stainless steel rod into the crucible and quickly removing it allowing the salt to freeze. The frozen salt was then broken off of the threaded rod and placed in a sample bottle. Figure 5.7 shows photographs of both the the resulting mullite tube with electrolyte salt and some of the metal deposit that adhered to it in Fig. 5.7a, the frozen salt sample appears in Fig 5.7b.

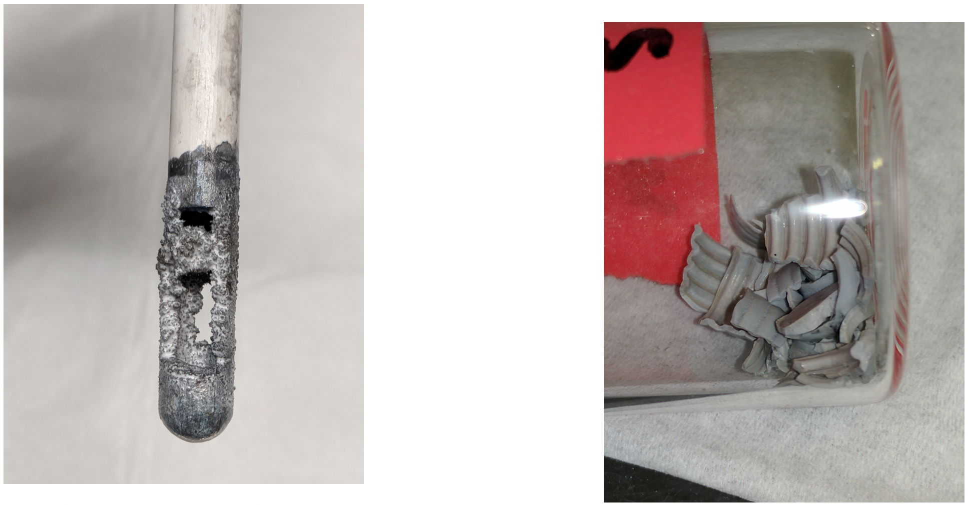

(a) Frozen salt and metal deposit on mullite tube

(b) Frozen electroylte salt sample

Figure 5.7: Photographs of samples from electrochemical cell for ICP-OES

All of the deposits were then dissolved in 10% volume HNO_3 and if needed, further dilutions were performed using pipettors (Ependorf) so that the analyte concentration would be between 1 and 100 ppm.

Calibration solutions were created using ICP standards purchased from Inorganic Ventures. After the solutions were made and dilutions performed, their concentrations were analyzed using a Spectro Genesis FES (Model No. 20.05.2009) ICP-OES machine shown in Fig. 5.8a. ICP-OES analysis returned concentrations in ppm which were converted to weight fraction (w_{MCl_n}) in the salt using the following equation:

$$w_{MCl_n} = (ppm)\frac{mg_M}{kg_{soln}}\frac{g}{10^3 mg}\rho_{soln}V_{soln}\frac{kg}{10^4 g}\frac{MW_{MCl_n}}{MW_M \cdot m_{sample}} \tag{5.1}$$

where ppm is the ICP measured concentration value in ppm (mg/kg) for one of the metal analytes in nitric acid solution, converted to g/kg. The density of HNO_3 is $1.05\,\mathrm{kg\,L^{-1}}$ The volume of the solution (V_{soln}) in L was known from the dissolution and dilution of samples. The molecular weights (MW_MCl_n) of the salt molecules $GdCl_3$ and $TbCl_3$, and the molecular weights (MW_M) of Gd and Tb are all known from the periodic table. The mass of the sample m_{sample} in g was measured for each test and placed in the denominator to yield weight fraction.

The uncertainty for these measurements were propagated using the standard deviation of each ICP-OES measurement and the error propagation formula for division, substituting the variables as needed:

$$\delta R = \sqrt{\left(\frac{\delta w_{MCl_n}}{w_{MCl_n}}\right)^2 + \left(\frac{\delta m_{sample}}{m_{sample}}\right)^2} \times R \tag{5.2}$$

The cathode deposit samples includes both the metal deposit and adhered electrolyte salt as seen in Figure 5.7a. For the cathode samples, dilution steps were taken into account using the following formula:

$$C_f V_f = C_i V_i \tag{5.3}$$

where C_f is the final concentration of the analyte in ppm and V_f is the final volume of the total solution in L. The density and volumes are used to find the total amount of analyte in the sample, M. C_i is the initial concentration of the analyte in ppm and V_f is the amount of the dissolved sample that was originally removed for dilution in L. The amount of metal in the cathode sample, $m_{M_{metal}}$, was determined by multiplying the weight fraction of the chloride analyte, w_{MCl_n}, by the total weight of the sample m_M and then subtracting the mass of chloride analyte, $m_M Cl_n$, from the total amount of analyte in the sample, m_M.

$$m_{M_{metal}} = m_M - (w_{MCl_n} \times m_{sample}) \tag{5.4}$$

The second cathode deposits from tests 1, 5, and 8 were washed with ethanol to remove the salt from the surface of the deposit for SEM-EDS analysis. The SEM used in this work is the Hitachi S-4800 shown in Fig. 5.8b. The machine is equipped with an EDS system that enables elemental analysis of the sample.

(a) SPECTRO GENESIS ICP-OES spectrometer at University of Utah

(b) Hitachi S-4800 Field Emission SEM with Energy Dispersive X-ray Spectroscopy

Figure 5.8: A figure with two subfigures

5.5 Experimental Methods

The following methods are largely adopted from the research done at the University of Utah[56].

5.5.1 Surface Area Measurement

The WE area was determined by using the vertical translator method as described by Rappleye[56]. The method involves fixing the WE to an arm that moves vertically along a ruler, incrementally increasing the depth of the WE in the molten salt. At each immersion depth, CV was performed. Linear plots of peak height versus the change in immersion depth of the WE in the molten salt, similar to the one shown in Figure 5.9, were obtained using this technique.

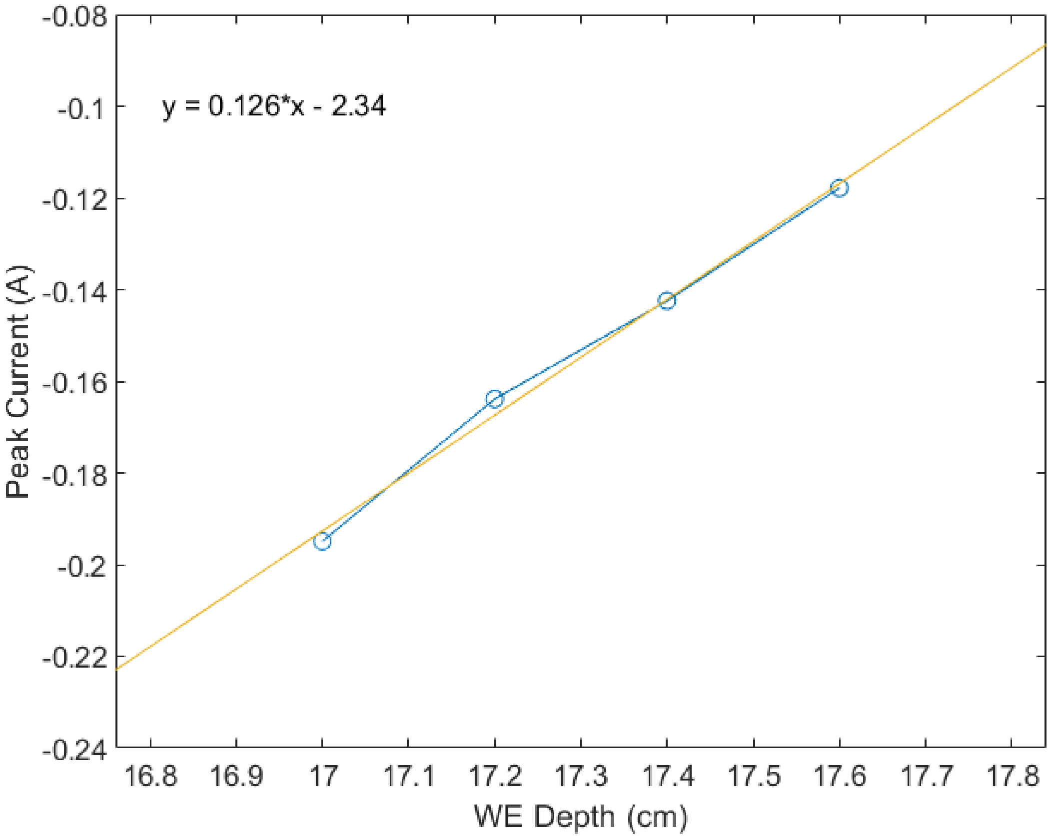

Figure 5.9: Immersion depth calibration curve.

The immersion depth of the WE is obtained from the y-intercept of the linear regression of the change in the WE depth with respect to peak height, the y-intercept in Fig. 5.9 was 2.34 cm.

5.5.2 Salt additions

Salt mixtures were made by initially introducing $TbCl_3$ into eutectic LiCl-KCl, then progressively adding $GdCl_3$ before each new experiment. Since multiple experiments were run consecutively, the $GdCl_3$ was often added while the furnace was hot and the salt mixture still melted. The furnace lid was carefully removed from the furnace exposing the crucible and the weighed $GdCl_3$ samples were carefully poured into the crucible from an aluminum weigh boat. A wax paper sheet was used at first, but the high temperatures caused the ends of the paper burn and curl up. After adding an analyte, the salt would be stirred and then allowed to settle for 1-2 hours. CVs were recorded and when 3 or more CVs overlapped, the salt would be considered well mixed and tests resumed.

Challenges and solutions

In early experiment designs, the anode was going to consist of Tb powder that would be put inside of a stainless steel mesh basket shown in Figure 5.10.

Figure 5.10: Photograph of first anode basket design

The basket was really large and there was little room in the crucible. It would have required a lot of Tb metal to fill the basket and there was not enough. It was also unclear if the mesh size of the metal powder was too small for this stainless steel mesh. Material loss was a concern.

The experiments relied on electrodepositing significant amounts of metal onto the W cathode and collecting those samples for analysis. It is common for dendrites to form as the metal deposits and these often fall off of the electrode. To obviate this problem, a mullite tube served as a basket that surrounds the W rod to catch any metal deposits that fall off the cathode during the electrodeposition run. Two windows were cut out of the mullite tube using a circular saw to make the openings wide enough to not interfere with the electrodeposition. A photograph of the custom mullite tube basket is shown in Fig. 5.11.

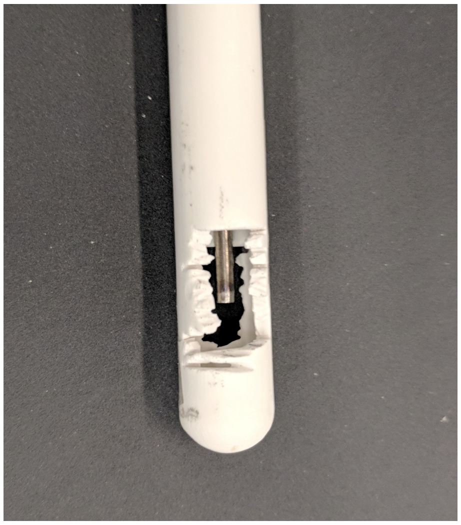

Figure 5.11: Photograph of custom mullite tube basket

While the basket did help to capture the metal deposits, it also added a very large surface area for the molten salt to adhere to. The very large salt concentrations found in the cathode samples are largely attributed to the salt adhered to the mullite tube basket.

It was important to setup each experiment the same way, limiting the number of times electrodes were moved in and out of the cell would have helped maintain consistency. The main problem arose when $GdCl_3$ was added before each experiment. All of the electrodes had to be removed in order to take the lid off the furnace. The $GdCl_3$ powder was very fine and only small amounts were added at a time. Adding the $GdCl_3$ powder through a glass funnel through one of the holes in the lid was tried but the powder ended up sticking to the sides of the funnel stem and it was unclear how much powder went into the crucible and how much just stuck to the funnel. This could be weighed and the missing amount could be re-added, but the same problem would just keep occurring and with smaller and smaller amounts, the uncertainties would just be driven up.

Removing the lid was the best way to ensure the right amount of salt was being added to the crucible. If the lid and intact electrodes could be removed all in one piece and held up above the furnace, this could have helped reduce any setup error, but the height of the glovebox and the length of the electrodes prohibited this option.

Inserting the thermocouple after all the electrodes were in place proved to be a problem because there was very little space in the cell for the thermocouple to go. It had to be squeezed in between electrodes and while care was taken to make sure it was not touching anything else while in the cell, there was no way to tell. Most of the temperature readings were done before electrodes were placed in the cell, so any temperature fluctuations that happened right before and or during electrolysis were not recorded. An additional hole in the lid dedicated to the thermocouple could have been useful, but due to this experimental setup, space in the crucible was very limited.

5.6 Experimental Test Procedures

Electrochemical measurements were performed using Autolab NOVA (version 2.1) software. The general procedure is as listed:

1. Anodically clean WE
2. Run full CV from dissolution to Li deposition
3. Run CV at 5 or more scan rates (75-500 mV/s)
4. Run NPV with a step potential of 5 mV, pulse time of 0.3 s, interval time of 15 s
5. Run CA at -2.13 V until 365 C is passed
6. Measure OCP

After these electrochemical tests were performed, a sample was taken, $GdCl_3$ was added, and the tests were repeated.

Chapter 6

ERAD Qualification

Two component electrodeposition experiments were conducted to validate ERAD, a tool which was planned to be used to simulate Pu/Cm separation behavior in an electrorefiner and test the validity of the neutron balance safeguards approach. The qualification process allows defensible claims to be made about ERAD results when used to simulate various types of operations. To qualify ERAD as a suitable model to make safeguards conclusions, it was necessary to conduct small-scale experiments and compare them with small-scale ERAD simulations using the same electrochemical system.

This chapter documents the results of the electrochemical deposition experiments using the $TbCl_3-GdCl_3-LiCl-KCl$ electrolyte mixture and compares those results with the ERAD simulations of those same experiments. The details of the simulations and input parameters used are also detailed in this chapter. The comparison of the experiments and simulations provide a tenable claim about how ERAD performs with regard to real world processing.

6.1 Constant Potential Electrolysis

Electrodepostion runs with a constant potential set at -2.13 V (vs. 5-mol.% Ag|AgCl) were conducted to examine the Tb-Gd co-deposition behavior with various Gd^{3+} concentrations.

6.1.1 Reproducibility

To establish the analysis method is accurate, the results using two different analysis techniques are presented first. From the test matrix, 5.2, experiments with Tb/Gd ratios of only Tb, 25, and 1 were repeated and the results were analyzed with both ICP-OES and SEM-EDS to assure a robust experimental campaign was used.

Photographs of the deposits obtained from both of the 1:1 ratio tests, labeled A and B respectively, are shown in Fig. 6.1. Figure 6.1a shows a picture of the metal and salt deposit on the W rod electrode from test A after it was removed from the electrochemical cell. The deposit from test B is shown in Fig. 6.1b in the ethanol wash.

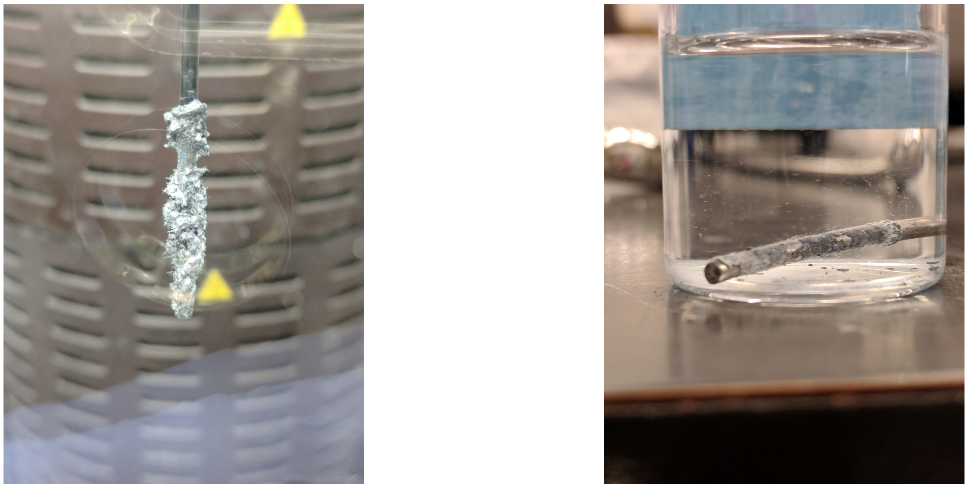

(a) Cathode deposit from test A

(b) Cathode deposit from test B in ethanol

Figure 6.1: Photographs of cathode deposits obtained by CA at -2.13 and temperature of 773 K (a) of test A with a duration of 2429 s, total electric charge passed 367 C and (b) of test B with a duration of 200 s, total electric charge passed 14 C.

The test A sample was dissolved, diluted and analyzed with ICP-OES. The test B sample was dried and analyzed with SEM-EDS.

Surface analysis

The SEM-EDS analysis was done on the samples before and after they were washed in ethanol. Photographs from the SEM were taken and EDS analysis maps were conducted on different points throughout each sample. One of the photographs from the surface scan by SEM for the unwashed sample from Test 5 with a 25:1 ratio, $Tb_3{}^+ = 1.07$wt.%, $Gd_3{}^+ = 0.037$wt.%, is shown in Figure 6.2.

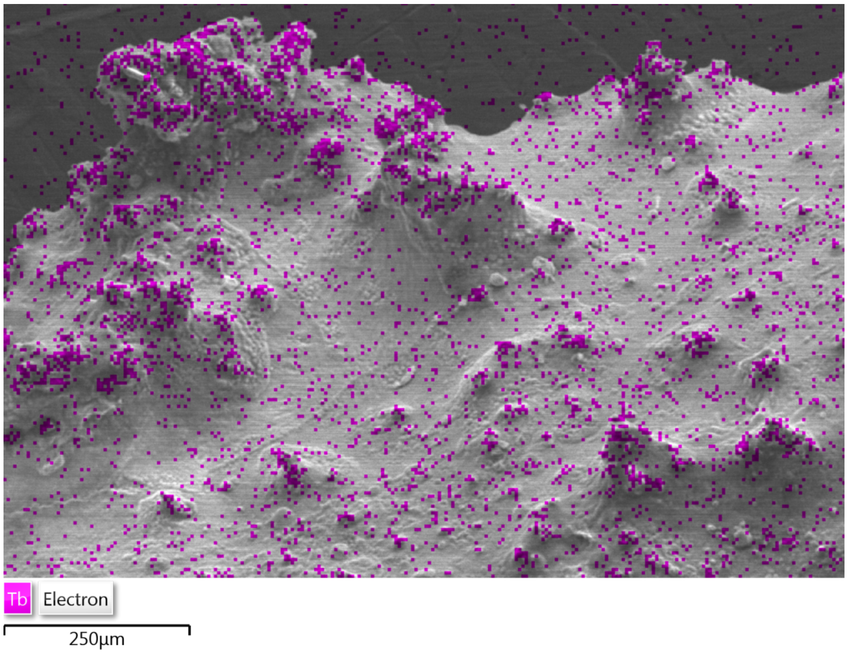

Figure 6.2: SEM-EDS image map of Tb in the cathode deposit from test 5 25:1 sample, $Tb_3{}^+ = 1.07$wt.%, $Gd_3{}^+ = 0.037$wt.%, distance of 15 mm, current at 15 μA, acceleration 20.0 kV.

The image and EDS results show only Tb and not Gd on the sample surface. The charts shown in Figures 6.3 and 6.5 reveals the other elements found in the sample, notably, the dominating Cl peaks.

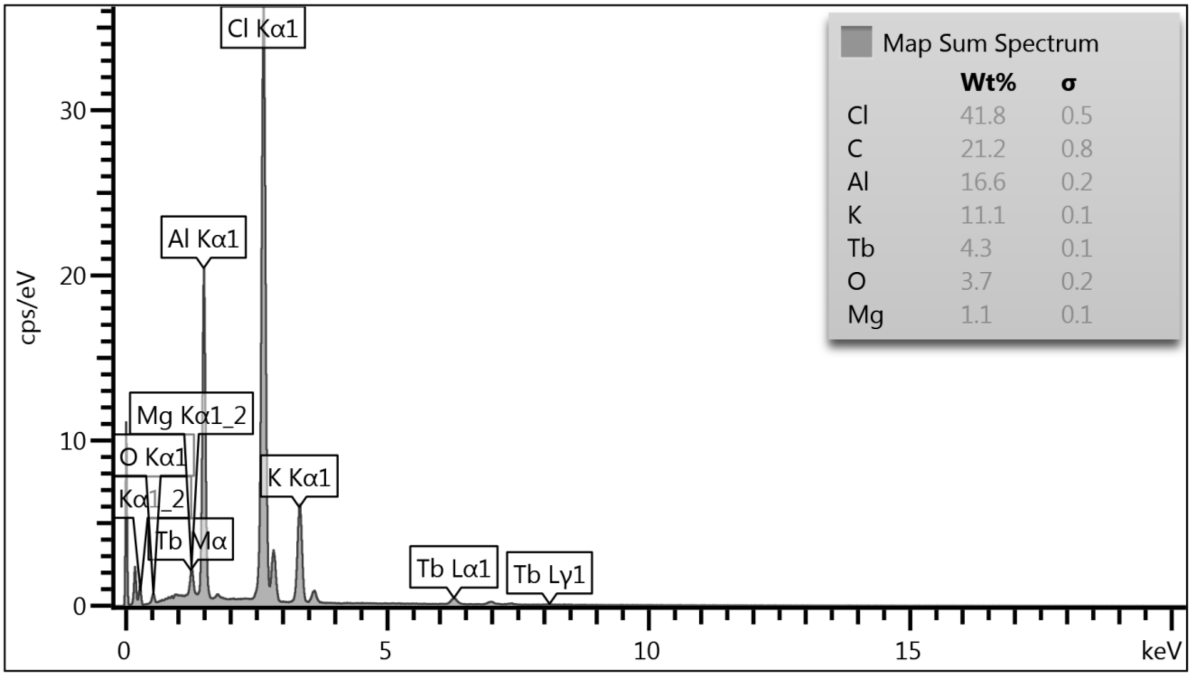

Map Sum Spectrum

	Wt%	σ
Cl	41.8	0.5
C	21.2	0.8
Al	16.6	0.2
K	11.1	0.1
Tb	4.3	0.1
O	3.7	0.2
Mg	1.1	0.1

Figure 6.3: Spectrum of elements in Test 5 25:1 sample, $\text{Tb}_3{}^+ = 1.07$wt.%, $\text{Gd}_3{}^+ = 0.037$wt.%

One of the SEM-EDS surface images from the cathode deposit from test 8 with a 1:1 Tb to Gd ratio, also unwashed, is shown in Figure 6.4

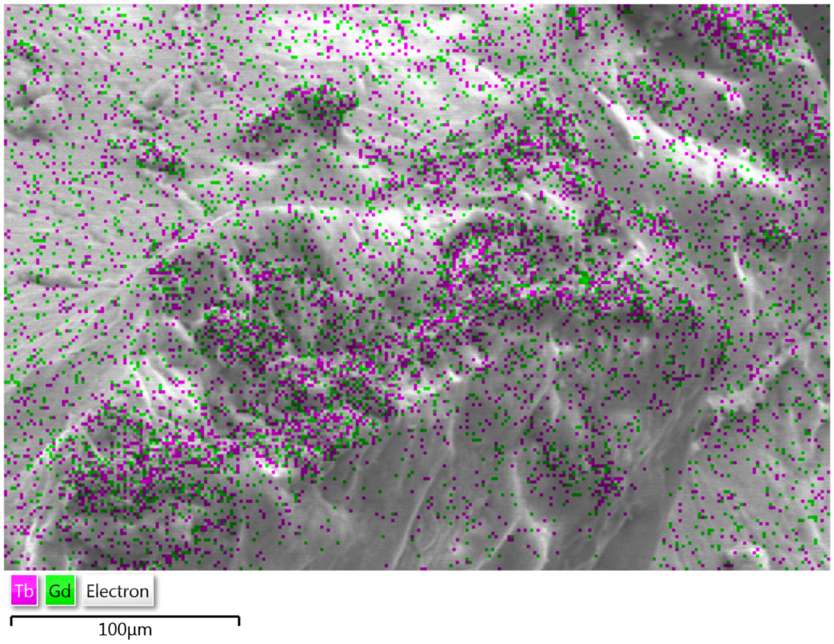

Figure 6.4: SEM-EDS image map of Tb and Gd in the cathode deposit from test 8 1:1, $Tb_3{}^+ = 1.17$wt.%, $Gd_3{}^+ = 1.00$wt.%, distance of 15 mm, current at 15 μA, acceleration 20.0 kV.

The Gd^{3+} concentration in the salt was increased to 1.0 wt.% for this test, and Gd and Tb were both identified on the sample surface by EDS.

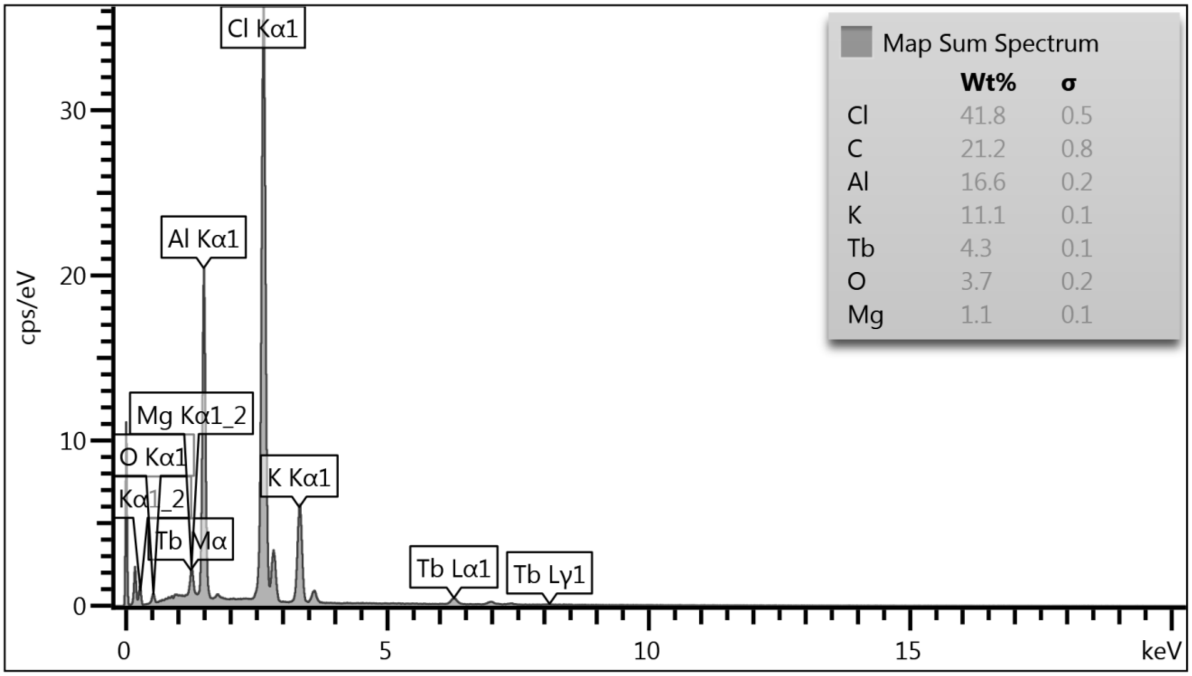

Figure 6.5: Spectrum of elements in Test 8 1:1 sample, $\text{Tb}_3{}^+ = 1.17$wt.%, $\text{Gd}_3{}^+ = 1.00$wt.%

Maps of Tb and Gd were done at different points along the sample surface to determine their presence and concentrations in the sample. Cl was also mapped to calculate the amount of salt on the sample before and after the ethanol wash. The molar ratio of Cl to Tb in TbCl_3 and the Cl to Gd in GdCl_3 is 3 to 1. If the Cl/Tb and Cl/Gd ratios are less than 3, the EDS is likely analyzing metal. If the ratios are higher 3 or higher, then the EDS is likely only measuring salt.

The EDS results of the unwashed deposit samples are displayed in Tables 6.1, 6.2, 6.3. The tables show the elemental weight percents, Cl/M ratio, and uncertainties.

Table 6.1: SEM-EDS points of unwashed deposit from the Tb-only test (Tb^{3+} = 0.80wt.%, Gd^{3+} = 0.005wt.%)

Point No.	**Cl (wt.%)**	**Tb (wt.%)**	**Cl/Tb**
1	66 ± 0.9	34 ± 0.6	2.0 ± 0.04
2	87 ± 1	13 ± 0.3	7 ± 0.2
3	88 ± 2	12 ± 0.4	7 ± 0.3
Avg.	81 ± 12	19 ± 12	5 ± 3

Table 6.2: SEM-EDS points of unwashed deposit from the 25:1 test (Tb^{3+} = 1.07wt.%, Gd^{3+} = 0.037wt.%)

Point No.	**Cl (wt.%)**	**Tb (wt.%)**	**Cl/Tb**
1	94 ± 2	6 ± 0.2	15 ± 0.5
2	94 ± 2	6 ± 0.2	15 ± 0.5
3	91 ± 1	9 ± 0.2	10 ± 0.3
Avg.	93 ± 2	7 ± 2	14 ± 3

Table 6.3: SEM-EDS points of unwashed deposit from the 1:1 test (Tb^{3+} = 1.17wt.%, Gd^{3+} = 1.00wt.%)

Point No.	**Cl (wt.%)**	**Tb (wt.%)**	**Gd (wt.%)**	**Cl/Tb**	**Cl/Gd**
1	91 ± 2	5 ± 0.2	4 ± 0.2	17 ± 0.7	23 ± 1
2	79 ± 1	13 ± 0.4	9 ± 0.2	6 ± 0.2	9 ± 0.3
3	91 ± 2	5 ± 0.3	3 ± 0.3	17 ± 1	26 ± 2
4	94 ± 3	4 ± 0.4	3 ± 0.4	26 ± 3	36 ± 5
5	75 ± 2	15 ± 0.5	11 ± 0.5	5 ± 0.2	7 ± 0.4
Avg.	86 ± 9	8 ± 5	6 ± 4	14 ± 9	20 ± 12

The results from Tables 6.1, 6.2, 6.3 show high Cl/Tb and high Cl/Gd ratios. A molar ratio above 3 indicates the EDS points are only analyzing salt. The only EDS point that could be analyzing metal is from point number 1, from test 1 where the Cl/Tb ratio is 2.04 at its maximum in the uncertainty range.

Table 6.4: SEM-EDS points of washed deposit from the 25:1 test

Point No.	Cl (wt.%)	Tb (wt.%)	Cl/Tb
1	44 ± 0.6	56 ± 1	0.8 ± 0.02
2	47 ± 0.5	53 ± 0.8	0.9 ± 0.02
Avg.	45 ± 2	55 ± 2	0.8 ± 0.1

Samples from the 25:1 and 1:1 tests were washed with ethanol several times to remove the salt. A photograph of the 25:1 test sample in the ethanol wash is shown in Figure 6.6. The photograph shows the salt separating from the metal rod and deposit.

Figure 6.6: 25:1 Test sample in ethanol bath

Tables 6.4 and 6.5 show the SEM-EDS results after the samples were washed several times.

The molar ratios of Cl to Tb and Gd in Tables 6.4 and 6.5 are all below 3. The EDS points were assumed to be analyzing metallic Tb and Gd deposits. The assumed metallic Tb/Gd ratios in the sample from test 8 are shown in Table 6.6.

Table 6.5: SEM-EDS points of washed deposit from the 1:1 test

Point No.	**Cl (wt.%)**	**Tb (wt.%)**	**Gd (wt.%)**	**Cl/Tb**	**Cl/Gd**
1	22 ± 1	46 ± 3	32 ± 2	0.5 ± 0.03	0.7 ± 0.1
2	22 ± 2	50 ± 5	27 ± 4	0.4 ± 0.1	0.8 ± 0.2
3	27 ± 0.8	44 ± 1	29 ± 1	0.6 ± 0.03	0.9 ± 0.05
4	36 ± 1	38 ± 2	26 ± 1	0.9 ± 0.05	1 ± 0.1
5	21 ± 1	47 ± 2	32 ± 2	0.4 ± 0.03	0.6 ± 0.1
6	25 ± 1	44 ± 2	30 ± 2	0.6 ± 0.03	0.8 ± 0.1
Avg.	26 ± 6	45 ± 4	29 ± 3	0.6 ± 0.2	0.9 ± 0.3

Table 6.6: Tb/Gd ratios from the EDS measurements of the unwashed and washed deposits of the 1:1 test

Point No.	**Tb/Gd**$_{unwashed}$	**Tb/Gd**$_{washed}$
1	1 ± 0.1	1 ± 0.1
2	2 ± 0.1	2 ± 0.4
3	2 ± 0.2	2 ± 0.1
4	1 ± 0.2	2 ± 0.1
5	1 ± 0.1	2 ± 0.1
6		2 ± 0.1
Avg.	1 ± 0.1	2 ± 0.1

The average Tb/Gd ratio of the electrolyte salt is 1 ± 0.1. The average metallic Tb/Gd ratio is 2 ± 0.1.

Current-time curves

The current-time curves measured during electrodeposition for both of the 1:1 Test (Tb^{3+} = 1.17wt.%, Gd^{3+} = 1.00wt.%) experiments were compared to make sure they match. The first Test is labeled A and the second test is labeled B. The current-time curves for the first 200 s of A and B, are shown in Figure 6.7.

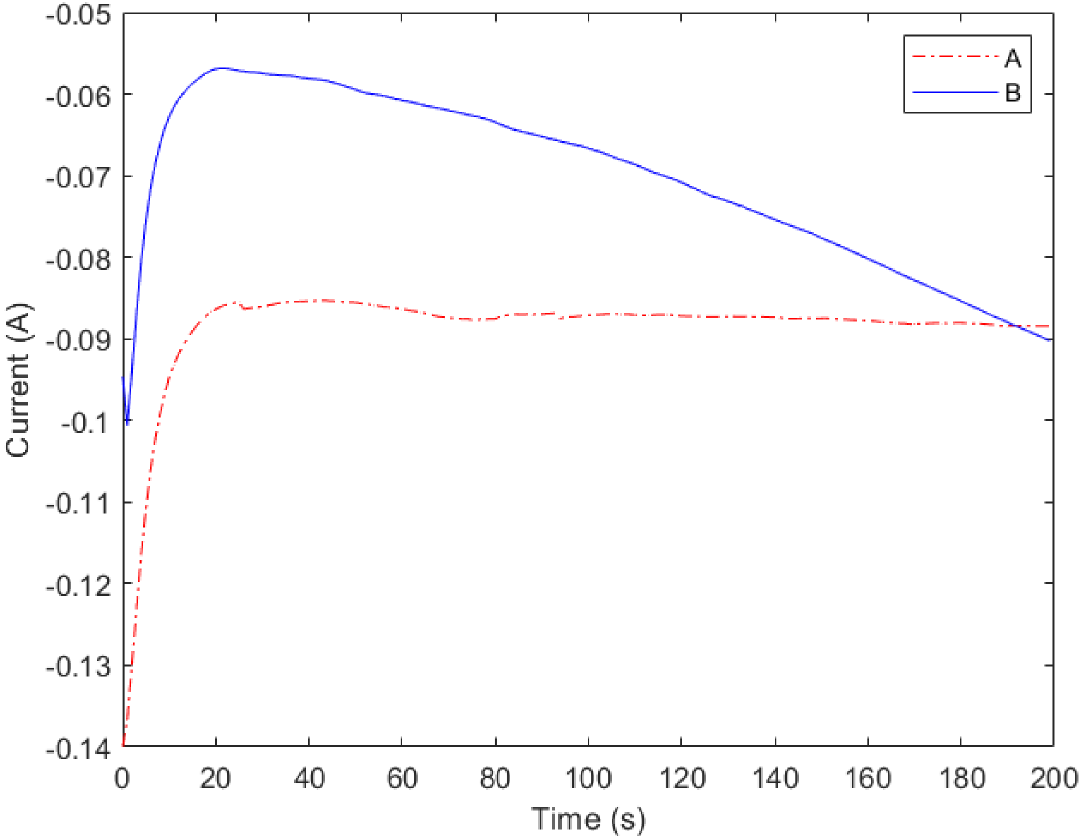

Figure 6.7: Current-time curves on W cathode (2 mm diameter) during potentiostatic electrolysis at -2.13 V in LiCl-KCl eutectic melts containing 1.17 wt.% of Tb^{3+} and 1.00 wt.% of Gd^{3+} at 773 K.

The cathodic current of test B increased more rapidly than test A, but started at a more positive current. This could be due to a difference in WE surface area since increasing the surface area should increase the current, dictated by Ohm's law. During the first 200 s, the average current for test A was -0.089 A and -0.070 A for test B. The WE for test A could have been immersed in the electrolyte a little more than the WE for test B.

Open-circuit potential

Differences in OCP measurements are usually indicative of the apparent potentials of specific species on the WE and should vary logarithmically with concentration or mole

Table 6.7: Standard apparent potentials, vs. 5-mol.% Ag|AgCl, from CA tests with concentrations of Tb and Gd metal in cathode deposits

Test No.	**Tb wt.%**	**Gd wt.%**	**$E^{0'}$ (V vs. Ag|AgCl)**
1	1.000 ± 0.317		-2.108 ± -0.008
2	0.989 ± 0.311	0.011 ± 0.004	-2.102 ± -0.008
3	0.986 ± 0.310	0.014 ± 0.005	-2.101 ± -0.008
4	0.985 ± 0.310	0.015 ± 0.005	-2.117 ± -0.008
5	0.982 ± 308	0.018 ± 0.006	-2.092 ± -0.008
6	0.923 ± 282	0.077 ± 0.026	-2.097 ± -0.008
7	0.885 ± 0.266	0.115 ± 0.038	-2.102 ± -0.008
8	0.572 ± 0.161	0.428 ± 0.136	-2.078 ± -0.008

fraction. If this behavior can be verified for molten salt mixtures of interest, then it could be used to determine concentration[56]. In Rappleye's work, for example, the $E^{0'}$ of Gd^{3+}/Gd was found to be -2.999 V vs. $Cl^{-}|Cl$. For U^{3+}, $E^{0'} = -2.479 \pm 0.012$ and for Mg^{2+}, $E^{0'} = -2.784 \pm 0.049$. And there was a clear distinction in the potential versus time curves.

OCP tests were conducted throughout the experimental campaign. Comparing the OCP results from three different tests with the same parameters (Tests 1, 8, and 3 with 4), the average relative error of the OCP measurements was found to be 0.4%.

The OCP tests were conducted after each CA test and the results for these tests are in Table 6.7.

The purpose of the OCP test was to see if a change in open circuit potential could be measured when Tb was deposited on the WE versus Tb and Gd co-depositing on the W electrode. The OCP data in Table 6.7 is invariant within experimental error.

To verify the seemingly overlapping results, further OCP tests were conducted using a 6.35 mm diameter Tb rod as the WE and another one using a 6.35 mm diameter Gd rod as the WE. The electrolyte concentration consisted of approximately 1.0 wt.% $TbCl_3$ and

0.2 wt.% $GdCl_3$, Tb/Gd = 5, in LiCl-KCl eutectic. A 5-mol.% Ag|AgCl RE was used and tests were conducted at 773 K. The results of those tests are shown in Fig. 6.8.

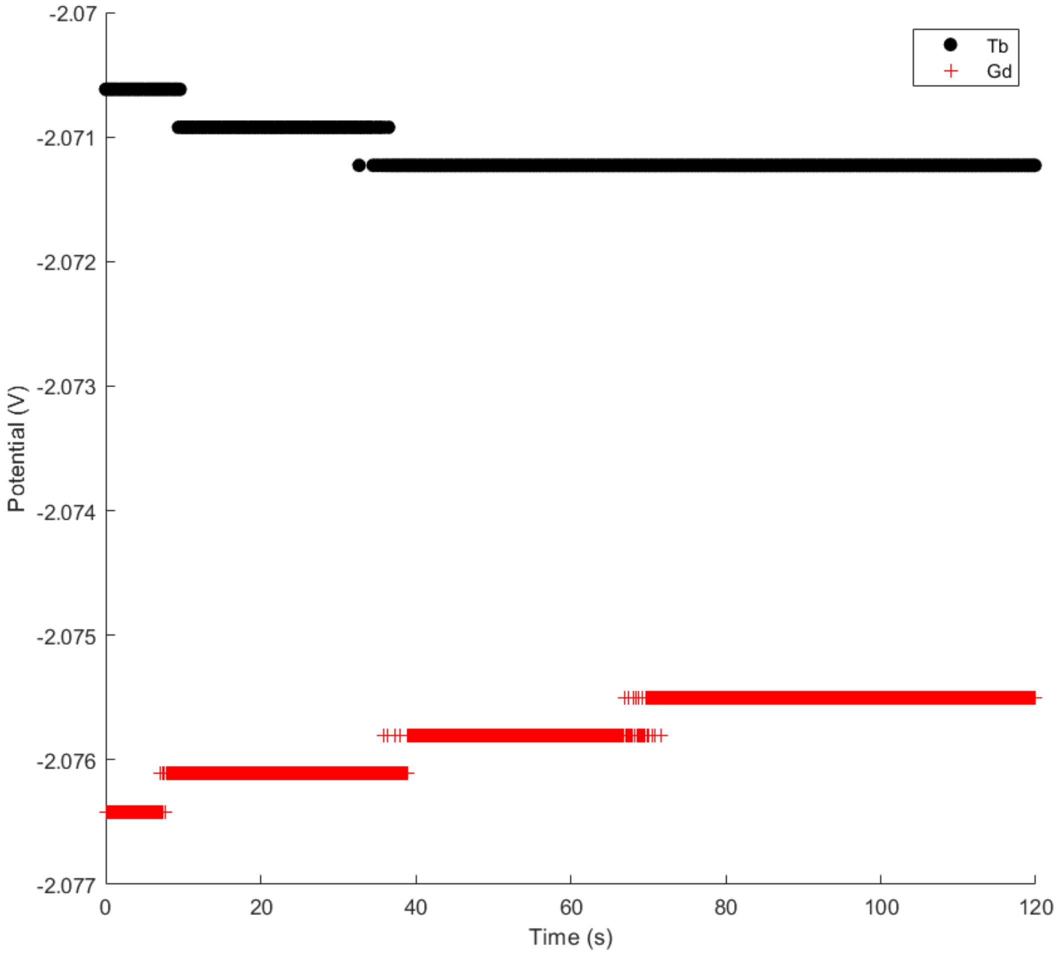

Figure 6.8: OCP tests vs. 5-mol.% Ag|AgCl RE using a 6.35 mm diameter Tb rod for the Tb test and a Gd rod for the Gd test as WE's, in 1.0 wt.% $TbCl_3$ and 0.2 wt.% $GdCl_3$ in LiCl−KCl eutectic at 773 K.

Figure 6.8 shows the OCP values between the Tb WE and the Gd WE are on the scale of 1/1000 V. It would be very difficult to distinguish elemental composition of the WE deposit using OCP.

Different processes and conditions in the cell may contribute to the OCP and therefore it doesn't necessarily correspond to any fixed equilibrium potential value. The results in

Table 6.7 and Fig. 6.8 do not show a significant difference between the Tb rod and the Gd rod and the CA deposits. When the potentials of the analytes are very close, it will be difficult to use OCP to distinguish changes in cathode deposit composition.

6.1.2 Mass transfer model

Figure 6.9 shows the current-time curves during electrolysis from the constant potential deposition experiments.

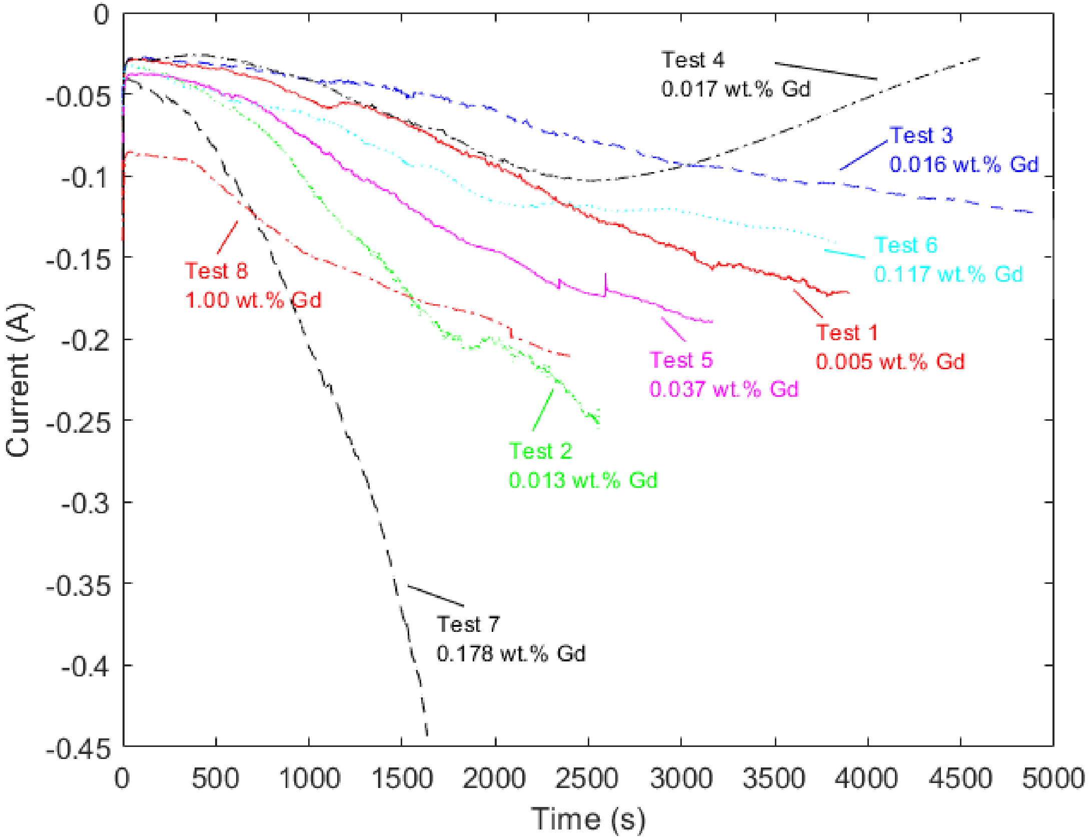

Figure 6.9: Current versus time on W cathode (2 mm diameter), E = -2.13 V at 773 K K in LiCl-KCl eutectic melts containing 1 wt% of Tb^{3+} and various concentrations of Gd^{3+} measured with ICP-OES.

On very short time scales, the analysis of CA data is based on the Cottrell equation, which defines the current-time dependence for linear diffusion control. According to the equation, the current approaches infinity at very short times and zero at very long times. However, in practice, this is not observed. At longer times, cathode area growth and natural convection can prevent the current from completely decaying away as plotted in Figure 6.10.

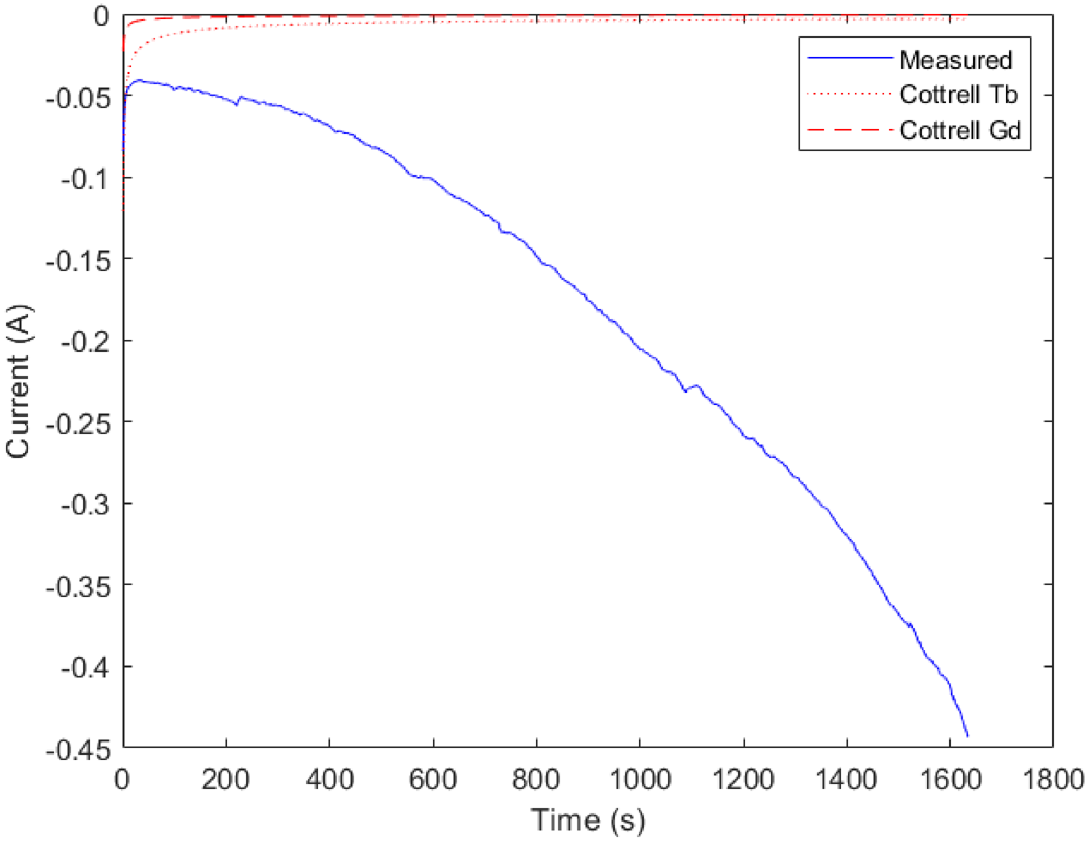

Figure 6.10: Current versus time plot at E = -2.13 V vs Ag|AgCl(5-mol.%) for Test 7 (1.1 wt% TbCl3, 0.18 wt% GdCl3, T = 773 K, Area = 1.57 cm^2)

Figure 6.10 shows the plots of the current versus time for the measured data of Test 7, and the predicted currents from the Cottrell equation for Tb and Gd. Since both Tb^{3+} and Gd^{3+} were in the electrolyte and both deposited on the cathode, the currents for both analytes were calculated.

The current-time plots are analyzed to see if information about deposit formation could be gained. A mass transport model, could tell us something about area growth over time with respect to mass. The area over mass should be consistent over time if the same species is being reduced on the cathode, but it could change when two different analytes are depositing.

In a constant potential experiment, the current is mass transfer controlled with the following expression:

$$i \approx nFAC \tag{6.1}$$

where nF are constants, k, relating electrons transferred to number of moles. The concentration term is assumed uniform in the bulk solution, so the current really depends on area growth over time:

$$i(t) = kCA(t) \tag{6.2}$$

where,

$$\frac{i(t_1)}{i(t_0)} = \frac{A(t_1)}{A(t_0)} \tag{6.3}$$

resulting in

$$A(t) = \frac{A(t_0)i(t)}{i_0} \tag{6.4}$$

where $A(t_0)$ is equal to the initial surface area of the WE and the current, i_0, is equal to the current in the first few seconds of the run, $t = 1$ s. The $A(t_0)$ is them divided by the total mass of each sample to understand how area growth per second may be affected by the mass of the metal. The are per gram versus time plot is shown in Figure 6.11.

Table 6.8: Comparison of parameters for tests 1, 5, and 8

Test No.	**Electrolyte Tb/Gd**	**Cathode area** (cm^2)	**Total charge** (C)	**Measured mass** (mg)	**Theoretical mass** (mg)
1	150	1.6	-373	229 ± 51	205
5	29	1.58	-367	179 ± 39	201
8	1	1.58	-367	183 ± 31	201

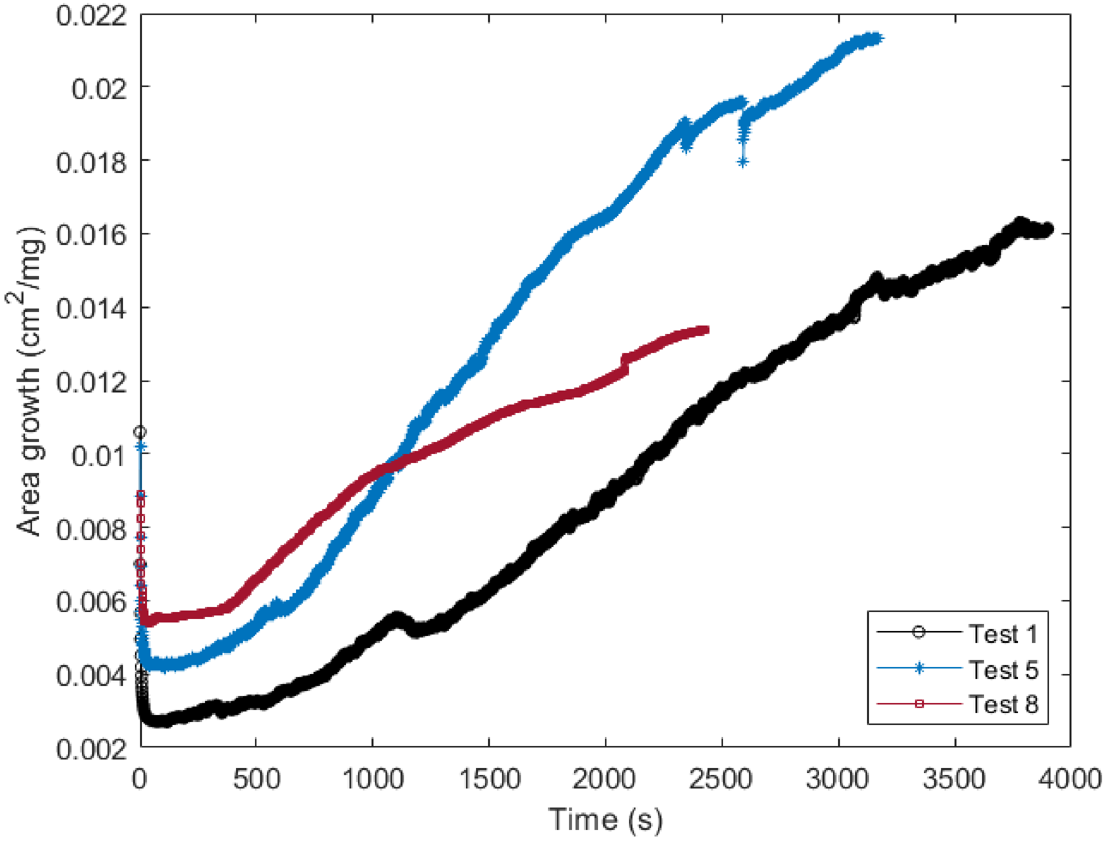

Figure 6.11: $cm^2\,mg^{-1}$ versus time (s) for tests 1, 5 and 8

Tests 1, 5, and 8 were chosen for this analysis because they all had similar operating parameters. Table 6.8 shows the cathode area, the total charge passed, and the measured and theoretical masses of the deposits.

These are useful for comparing because tests 1 and 5 yield similar area/gram growth over time but test 8 deposits the same amount of material as the other tests but in nearly

Table 6.9: Tb data in salt samples

Sample No.	**Tb (g)**	**$TbCl_3$ (wt.%)**
1	$6.88 \times 10^{-3} \pm 2.34 \times 10^{-5}$	$0.014 \pm 4.77 \times 10^{-5}$
2	$1.73 \times 10^{-3} \pm 7.39 \times 10^{-6}$	$0.018 \pm 7.71 \times 10^{-5}$
3	$5.62 \times 10^{-3} \pm 4.15 \times 10^{-5}$	$0.015 \pm 1.12 \times 10^{-4}$
4	$4.60 \times 10^{-3} \pm 1.53 \times 10^{-5}$	$0.016 \pm 5.20 \times 10^{-5}$
5	$5.73 \times 10^{-3} \pm 1.13 \times 10^{-5}$	$0.019 \pm 3.70 \times 10^{-5}$
6	$5.09 \times 10^{-3} \pm 5.71 \times 10^{-5}$	$0.023 \pm 2.58 \times 10^{-4}$
7	$6.00 \times 10^{-3} \pm 2.13 \times 10^{-5}$	$0.019 \pm 6.83 \times 10^{-5}$
8	$5.89 \times 10^{-3} \pm 5.25 \times 10^{-5}$	$0.02 \pm 1.83 \times 10^{-4}$

one quarter of the time. This gives an indication that Tb may not be the only material depositing on the cathode, which is consistent with the measured results from ICP-OES and SEM-EDS.

6.1.3 Full composition analysis

The ICP-OES results from the fully dissolved salt and cathode deposit samples are detailed in this section.

Salt sample results

The frozen electrolyte salt shown in Fig. 5.7b was weighed and analyzed using ICP-OES. The final analyte compositions were calculated using equation 5.1 and the mass of each sample. Tables 6.9 and 6.10 display the masses of Tb and Gd in the salt samples and their weight fractions in $TbCl_3$ and $GdCl_3$, which were used to estimate the amounts of $TbCl_3$ and $GdCl_3$ that were in the cathode deposit samples.

Table 6.11 displays the measured Tb/Gd ratios in each of the salt samples and the expected ratios from the test matrix, 5.2.

Table 6.10: Gd data in the salt samples

Sample No.	**Gd (g)**	**$GdCl_3$ (wt.%)**
1	$4.58 \times 10^{-5} \pm 3.99 \times 10^{-7}$	$9.35 \times 10^{-5} \pm 8.16 \times 10^{-7}$
2	$2.17 \times 10^{-5} \pm 2.31 \times 10^{-7}$	$2.28 \times 10^{-4} \pm 2.42 \times 10^{-6}$
3	$1.05 \times 10^{-4} \pm 5.46 \times 10^{-7}$	$2.84 \times 10^{-4} \pm 1.48 \times 10^{-6}$
4	$8.67 \times 10^{-5} \pm 3.36 \times 10^{-7}$	$2.97 \times 10^{-4} \pm 1.15 \times 10^{-6}$
5	$2.00 \times 10^{-4} \pm 1.51 \times 10^{-6}$	$6.57 \times 10^{-4} \pm 4.97 \times 10^{-6}$
6	$4.54 \times 10^{-4} \pm 3.91 \times 10^{-6}$	$2.06 \times 10^{-3} \pm 1.77 \times 10^{-5}$
7	$9.70 \times 10^{-4} \pm 1.19 \times 10^{-5}$	$3.13 \times 10^{-3} \pm 3.83 \times 10^{-5}$
8	$5.05 \times 10^{-3} \pm 5.14 \times 10^{-5}$	$1.76 \times 10^{-2} \pm 1.79 \times 10^{-4}$

Table 6.11: Tb/Gd ratios in each salt sample

Sample No.	**Tb/Gd**	**$Tb/Gd_{expected}$**
1	150 ± 1.41	undefined
2	79.5 ± 0.911	100
3	53.5 ± 0.483	75
4	53.1 ± 0.271	50
5	28.7 ± 0.224	25
6	11.2 ± 0.158	10
7	6.19 ± 0.079	5
8	1.17 ± 0.016	1

To illustrate how the measured values compare with the test matrix, Figure 6.12 shows the ICP-OES measured Tb^{3+}/Gd^{3+} ratios versus the expected Tb^{3+}/Gd^{3+} ratios, from the test matrix (Table 5.2) in each salt sample, which resulted in a best fit slope of 0.76.

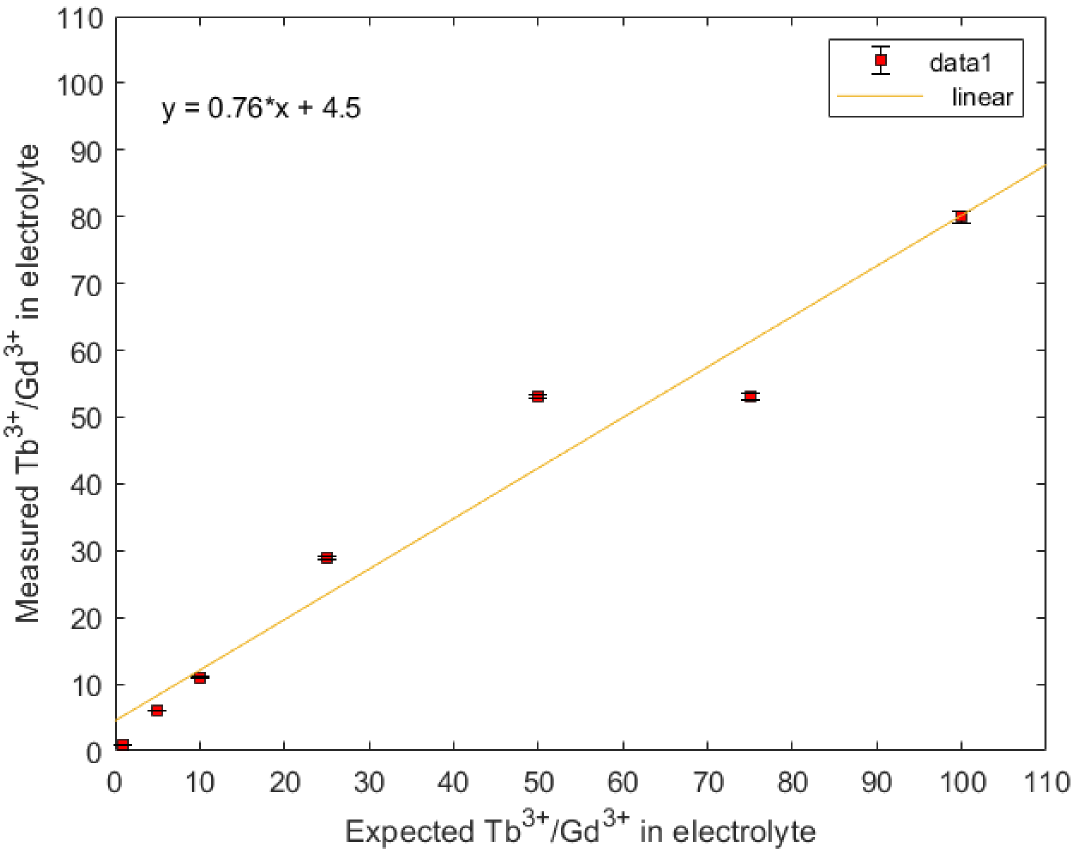

Figure 6.12: Measured versus expected Tb^{3+}/Gd^{3+} ratio in electrolyte salt samples 2-8

Cathode deposit results

The cathode deposit sample included both the dissolved metal deposit and adhered electrolyte salt as seen in Figure 6.1a. The electrolyte salt was not washed off of the cathode samples to avoid the metal deposit reacting with water, so both the metal deposit and adhered salt were dissolved and analyzed using ICP-OES. The total weight of the cathode sample was obtained by subtracting the masses of the mullite tube and W rod from the total sample mass. The total amount of Tb and Gd was calculated using Equation 5.1 and the dilution equation 5.3. The amount of $TbCl_3$ and $GdCl_3$ was approximated with Equation 5.4, multiplying the weight fraction of $TbCl_3$ and $GdCl_3$ from the salt samples in Tables 6.9 and 6.10 by the total mass of each cathode deposit.

Table 6.12: Tb data in the cathode deposits

Tb/Gd$_{salt}$	**TbCl3 (g)**	**Tb metal (g)**	**Tb (wt.%)**
150 ± 1.41	$0.011 \pm 3.71 \times 10^{-5}$	0.236 ± 0.050	1.0 ± 0.301
79.5 ± 0.911	$0.005 \pm 2.02 \times 10^{-5}$	0.275 ± 0.058	0.989 ± 0.296
53.5 ± 0.483	$0.013 \pm 9.46 \times 10^{-5}$	0.151 ± 0.032	0.986 ± 0.295
53.1 ± 0.271	$0.026 \pm 8.47 \times 10^{-5}$	0.205 ± 0.044	0.985 ± 0.294
28.7 ± 0.224	$0.014 \pm 2.83 \times 10^{-5}$	0.179 ± 0.038	0.982 ± 0.293
11.2 ± 0.158	$0.029 \pm 3.28 \times 10^{-4}$	0.185 ± 0.039	0.923 ± 0.268
6.19 ± 0.079	$0.018 \pm 6.23 \times 10^{-5}$	0.127 ± 0.027	0.886 ± 0.253
1.17 ± 0.016	$0.020 \pm 1.77 \times 10^{-4}$	0.102 ± 0.022	0.575 ± 0.154

Table 6.13: Gd data and the Tb/Gd in the cathode deposits

Tb/Gd$_{salt}$	**GdCl3 (g)**	**Gd metal (g)**	**Gd (wt.%)**	**Tb/Gd$_{metal}$**
79.5 ± 0.911	$5.94 \times 10^{-5} \pm 6.32 \times 10^{-7}$	$0.003 \pm 7.94 \times 10^{-4}$	$2.28 \times 10^{-4} \pm 2.42 \times 10^{-6}$	88 ± 29
53.5 ± 0.483	$2.41 \times 10^{-4} \pm 1.25 \times 10^{-6}$	$0.002 \pm 5.43 \times 10^{-4}$	$2.84 \times 10^{-4} \pm 1.48 \times 10^{-6}$	71 ± 24
53.1 ± 0.271	$4.83 \times 10^{-4} \pm 1.87 \times 10^{-6}$	$0.003 \pm 7.83 \times 10^{-4}$	$2.97 \times 10^{-4} \pm 1.15 \times 10^{-6}$	67 ± 22
28.7 ± 0.224	$4.99 \times 10^{-4} \pm 3.78 \times 10^{-6}$	$0.003 \pm 8.24 \times 10^{-4}$	$6.57 \times 10^{-4} \pm 4.97 \times 10^{-6}$	55 ± 18
11.2 ± 0.158	$2.62 \times 10^{-3} \pm 2.25 \times 10^{-5}$	$0.015 \pm 3.93 \times 10^{-3}$	$2.06 \times 10^{-3} \pm 1.77 \times 10^{-5}$	12 ± 4.0
6.19 ± 0.079	$2.85 \times 10^{-3} \pm 3.49 \times 10^{-5}$	$0.016 \pm 4.17 \times 10^{-3}$	$3.13 \times 10^{-3} \pm 3.83 \times 10^{-5}$	8 ± 3
1.17 ± 0.016	$1.71 \times 10^{-2} \pm 1.74 \times 10^{-4}$	$0.075 \pm 1.92 \times 10^{-2}$	$1.76 \times 10^{-2} \pm 1.79 \times 10^{-4}$	1 ± 0.4

The salt sample analysis revealed two of the samples yielded the same Tb/Gd ratio of 53, within the error margin. The error analysis for the metallic contributions of the deposit were calculated by comparing these tests, which yielded a relative error of 21% for Tb metal and 26% for Gd metal.

Tables 6.12 and 6.13 display the concentrations of $TbCl_3$ and $GdCl_3$, the masses and weight percents of Tb and Gd metal, and the ratios of Tb metal to Gd metal in each cathode sample.

Table 6.14 shows the total mass of metal in the deposit (g) and the amount expected from Faraday's Equation based on the total charge passed as measured by NOVA. The molar mass of Tb, $M = 158.93\,\mathrm{g\,mol^{-1}}$, is used in the theoretical calculations since that is the dominant species in the deposit.

The majority of the measured values are below or equal to the theoretical values. In the

Table 6.14: Measured and theoretical mass of metal in each deposit

$\mathrm{F} = 96\,500\,\mathrm{C\,mol^{-1}}$
$\mathrm{n} = 3$
$\mathrm{M} = 157.25\,\mathrm{g\,mol^{-1}}$

Tb/Gd$_{salt}$	**Charge (C)**	**Measured (g)**	**Theoretical (g)**
150 ± 1.41	373.39	0.236 ± 0.050	0.205
79.5 ± 0.911	361.31	0.278 ± 0.058	0.190
53.5 ± 0.483	367.21	0.153 ± 0.032	0.202
53.1 ± 0.271	292.98	0.208 ± 0.044	0.161
28.7 ± 0.224	366.99	0.182 ± 0.038	0.201
11.2 ± 0.158	368.71	0.201 ± 0.040	0.202
6.19 ± 0.079	358.71	0.144 ± 0.027	0.158
1.17 ± 0.016	366.66	0.177 ± 0.029	0.201

Table 6.15: Experimental conditions and results of Tb-Gd electrodeposition tests

Electrolyte (wt.%)			**CA Potential (V)**	**Duration (s)**	**Electric Charge (C)**	**OCP (V)**	**Deposit (wt.%)**		
Tb/Gd$_{salt}$	**Tb^{3+}**	**Gd^{3+}**					**Tb**	**Gd**	**Salt**
150 ± 1.41	0.014	9.35×10^{-5}	-2.13	3899	373	-2.11	0.303		0.697
79.5 ± 0.911	0.018	2.28×10^{-4}	-2.13	2614	361	-2.10	1.05	0.012	-0.064
53.5 ± 0.483	0.015	2.84×10^{-4}	-2.13	4919	367	-2.10	0.179	0.003	0.819
53.1 ± 0.271	0.016	2.97×10^{-4}	-2.13	4599	293	-2.12	0.126	0.002	0.872
28.7 ± 0.224	0.019	6.57×10^{-4}	-2.13	3169	367	-2.09	0.235	0.004	0.761
11.2 ± 0.158	0.023	2.06×10^{-3}	-2.13	3849	369	-2.10	0.146	0.012	0.842
6.19 ± 0.079	0.019	3.13×10^{-3}	-2.13	1714	359	-2.10	0.139	0.018	0.843
1.17 ± 0.016	0.020	1.76×10^{-2}	-2.13	2429	367	-2.08	0.105	0.078	0.817

actual experiments, the transfer of species to the electrode are subject to external phenomena such as temperature changes, metal falling off of the electrode after depositing, vibrations in the glovebox, and reoxidation of the species back into the electrolyte.

The summary of results is divided into two tables, 6.15 and 6.16. Table 6.15 presents the experimental conditions and the measured weight percents of Tb, Gd, and salts in the electrolyte and in the cathode deposit. Table 6.16 shows the Tb^{3+}/Gd^{3+} ratios in the electrolyte and the Tb/Gd ratio of just the metal in the cathode deposit.

The results of chemical analysis shown in Table 6.15 indicated that the adhered salt

Table 6.16: Tb/Gd results of Tb-Gd electrodeposition tests

Tb/Gd$_{salt}$	**Tb^{3+}/Gd^{3+} Electrolyte**	**Tb/Gd Metal**
150 ± 1.41	150 ± 1.41	
79.5 ± 0.911	79.5 ± 0.911	88.2 ± 29.4
53.5 ± 0.483	53.5 ± 0.483	71.0 ± 23.6
53.1 ± 0.271	53.1 ± 0.271	66.7 ± 22.2
28.7 ± 0.224	28.7 ± 0.224	55.3 ± 18.4
11.2 ± 0.158	11.2 ± 0.158	12.0 ± 4.01
6.19 ± 0.079	6.19 ± 0.079	7.78 ± 2.59
1.17 ± 0.016	1.17 ± 0.016	1.35 ± 0.450

accounted for 80% of the deposits on average. In all the tests the Tb/Gd ratio is higher in the deposit than in the electrolyte. This is likely due to the higher Tb concentration in the metallic deposit. Tests 6, 7 and 8 contained both metallic Tb and metallic Gd with ratios that agree well with those in the electrolyte, as can be seen in Fig. 6.15.

Figure 6.13 plots Tab. 6.14, using the average theoretical mass of M_{Tb} and M_{Gd} for tests 6, 7 and 8.

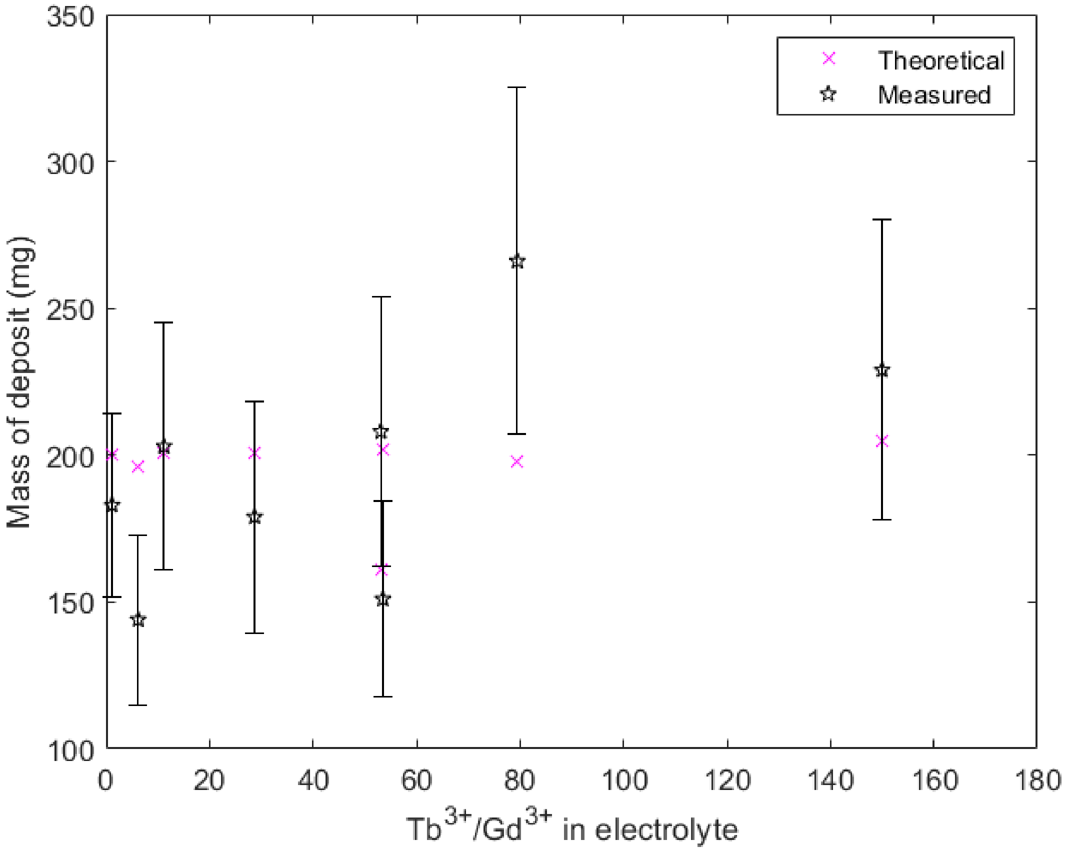

Figure 6.13: Comparison of measured and theoretical mass of deposit based on total charge passed

Within the uncertainty range of the measured metal deposits, tests 1, 4, 5, 6 and 8 agree with the theoretical values. The majority of the measured values are under or equal to the theoretical values, which makes sense since the theoretical amount operates under perfect conditions with no external factors such as fluctuations in temperature and non-homogeneity of the ions in the electrolyte around the cathode.

The weight percents of Tb and Gd metal in the deposit sample versus the measured Tb^{3+}/Gd^{3+} ratio in electrolyte salt are shown in Figure 6.14.

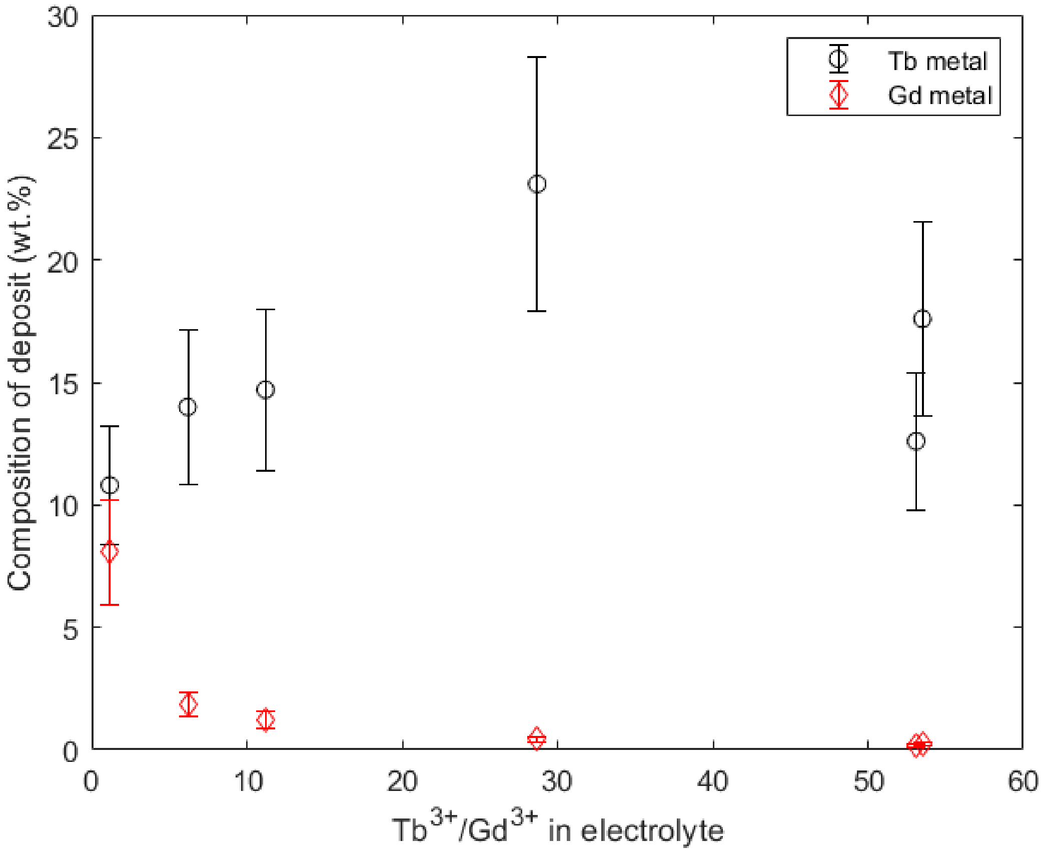

Figure 6.14: Concentrations of Tb and Gd metal in wt.% of cathode deposit sample versus Tb^{3+}/Gd^{3+} ratio in electrolyte salt, tests 3 to 8

Figure 6.15 shows the plot for Tb/Gd metal in the cathode deposits versus the Tb^{3+}/Gd^{3+} ratio in electrolyte salt for tests 3 to 8.

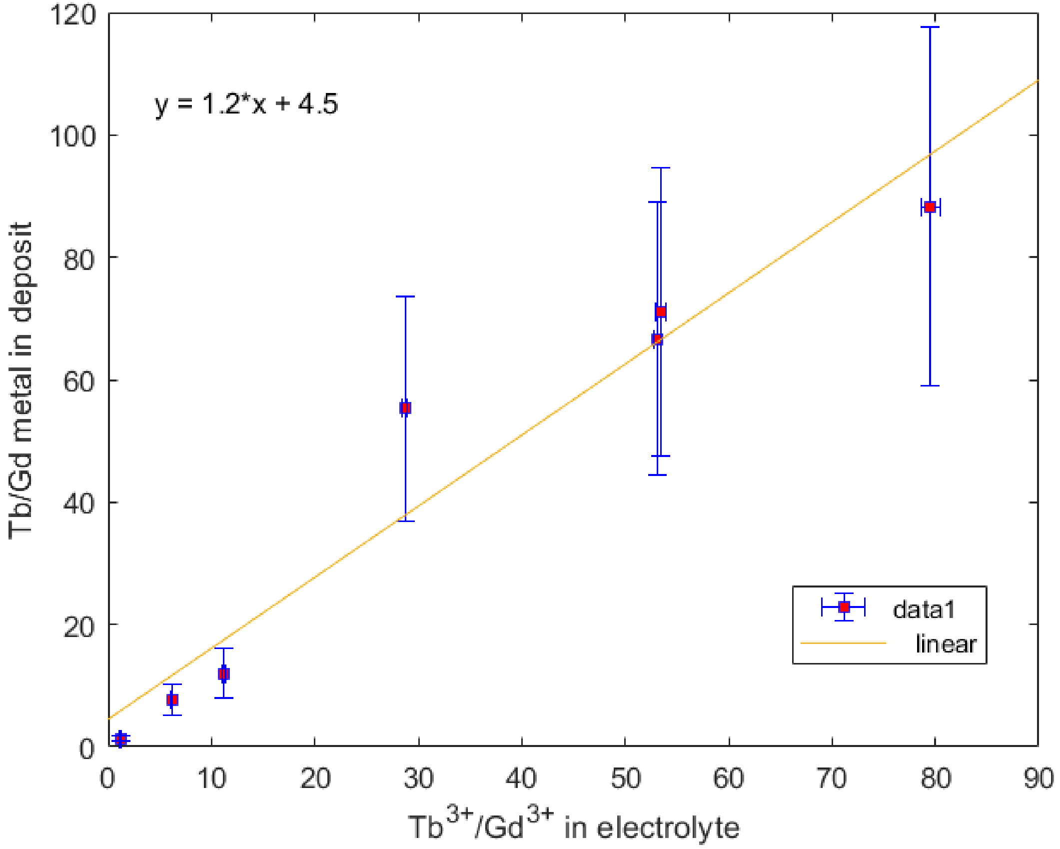

Figure 6.15: Tb/Gd metal in cathode deposits versus Tb^{3+}/Gd^{3+} ratio in electrolyte salt, tests 3 to 8

Plot 6.15 reveals that when the Pu/Cm ratio in the electrolyte is large, the ratio will not be the same on the cathode as in the salt.

6.1.4 Reproducibility findings

The Tb/Gd ratios from the ICP-OES and the SEM-EDS results are all listed in Table 6.17.

Table 6.17: Compiled Tb/Gd results from ICP-OES and average SEM-EDS measurements of cathode deposit samples from test A and B

		Tb/Gd	Comments
ICP-OES (test A)	Electrolyte	1.17 ± 0.650	all salt
	Deposit	1.32 ± 0.591	mostly salt
	Metal	1.34 ± 0.664	all metal
SEM-EDS (test B)	Unwashed deposit	1.43 ± 0.08	mostly salt
	Washed deposit	1.5 ± 0.1	all metal

The SEM-EDS results corroborate with the ICP-OES results, showing only Tb metal in the deposits from tests 1 and 5 and Tb and Gd metal in the deposit from test B with similar ratios in the salt and with test A. This finding supports the assumption that the Tb/Gd ratios in the salt and the metal could be equal when the Tb-Gd electrolyte salt concentration ratio is about 1:1.

6.1.5 Uncertainty and Error

Every step in the experimental process has an associated error and the final results are subject to the propagation of those errors. The more steps in the experimental plan, the opportunity for uncertainty grows.

Error propagation was conducted on calculated concentration measurements. For dividing a general function, $x = f(u, v)$, where $x = \pm au/v$, the following equation is used to determine the uncertainty σ_x for x,

$$\frac{\sigma_x^2}{x^2} = \frac{\sigma_u^2}{u^2} + \frac{\sigma_v^2}{v^2} \tag{6.5}$$

For equations of the form $x = au \pm bv$, Equation 6.6 is used,

$$\sigma_x^2 = a^2\sigma_u^2 + b^2\sigma_v^2 v^2 \tag{6.6}$$

Error propagation was used to compare the Tb/Gd ratios from the SEM-EDS washed deposit and the ICP-OES metal deposit. The Tb/Gd ratio from the SEM-EDS washed deposit was called $S \pm \sigma S$, and the Tb/Gd ratio from the ICP-OES metal deposit calculated was called $I \pm \sigma I$. To see if they agree, the difference, $|D| = S - I$, is computed. The uncertainty, σD is calculated using error propagation,

$$\begin{aligned} \sigma D &= \sqrt{\sigma S^2 + \sigma I^2} \\ &= \sqrt{(0.1)^2 + (0.664)^2} = 0.7 \end{aligned} \tag{6.7}$$

Since $|D| = 0.2 \pm 0.7$, zero is within the uncertainty range of D, so the two measurements agree. The ratios from the ICP-OES salt sample and the unwashed SEM-EDS sample are expected to agree since they are both measuring salt, and with a $|D| = 0.3 \pm 0.7$, they do agree. In fact, all of the Tb/Gd ratios are in agreement.

During electrolysis, the diffusion coefficient of each metal ion in the electrolyte limits its ability to traverse the diffusion layer and deposit on the cathode in a uniform and consistent matter. The heterogeneity of the electrolyte and distance to the cathode may inhibit certain species from being able to react in the time allotted. As the metal deposit grows, dendrites form and these change the constituency of the cathode and the surface area, these both affect the electrochemical process. In addition, these dendrites may fall off of the cathode. This may influence the electrochemical reaction since the surface area changed and it will have an effect on the final total mass of deposit results because that material may not be accounted for.

Measurement uncertainty also effects the final result and is taken into account. Uncertainty and error analysis was incorporated throughout the process and steps were taken to mitigate these effects as much as possible. Each sample was measured three times in the ICP-OES machine. Samples and electrodes were weighed three times. Some of the CA tests were repeated and analyzed using different methods to bolster the results. In addition to the systematic error from the scale, some of the salt powder could have fallen from the weigh boat from the scale to the furnace. Although care was taken to pour the salt powder in the center of the crucible, some of the salt powder could have adhered to the side of the crucible and not in the molten salt. To mitigate this source of error, visual inspection of the crucible was conducted after each salt addition. Detailed description of the uncertainty propagation can be found in the Appendix.

6.2 Simulating Tb/Gd Deposition

This project determined that Tb and Gd were good surrogates for Pu and Cm to use in experimental electrodeposition tests. The experiments concluded that the Tb/Gd ratios in the electrolyte and the cathode were inconsistent throughout the different electrodeposition tests. The experiments were then recreated in ERAD. The purpose of the experimental simulations was to test ERAD's performance for predicting analyte concentrations in the electrolyte and at the cathode for electrodeposition tests.

ERAD is run as a command from the command prompt or terminal window. ERAD gets all of its instructions from an input file titled *inpref*. The *inpref* file is organized by a broad pattern structure divided into six namelists. Each namelist contains parameters that define the systems such as element properties, electrode area, and initial inventories in the electrochemical cell. These parameters can be determined from electrochemical studies and thermochemical databases. For this study, most of the *inpref* parameters

Table 6.18: General input parameters for experimental ERAD simulations

Description	**Input parameter**
Temperature	773
Elements	Tb, Gd, K, Li, Cl
Time	0.5 - 1.4 h
Current	0.06 - 0.21 A
Anode surface area	6.301 cm^2
Anode initial mass	13.07 g
Cathode surface area	1.57 cm^2 (avg.)
Electrolyte initial mass	50 g

were obtained from the operating conditions and results of the experiments.

6.2.1 Input parameters

Most of the *inpref* parameters for the ERAD simulations matched the experiment values exactly and some were estimated from the literature, like the diffusion coefficient for each analyte and the alpha value. General ERAD input parameters and species-specific input parameters are displayed in Tables 6.18 and 6.19.

The experiments conducted used a constant potential of $E = -2.13V$ for electrolysis, but ERAD only simulates constant current runs. The current was estimated using the total charge passed over time for each experiment using the following relationship,

$$i = Q/t. \tag{6.8}$$

The mass and geometry of the anode changed over the course of the experiments. There were a total of 11 experiments and at the end of the experiments, the anode was noticeably depleted from Tb oxidation. Figure 6.16 shows photographs of the Tb rod before the CA experiments, left, and after the experiments, right. The dotted lines help illustrate the visible change in circumference.

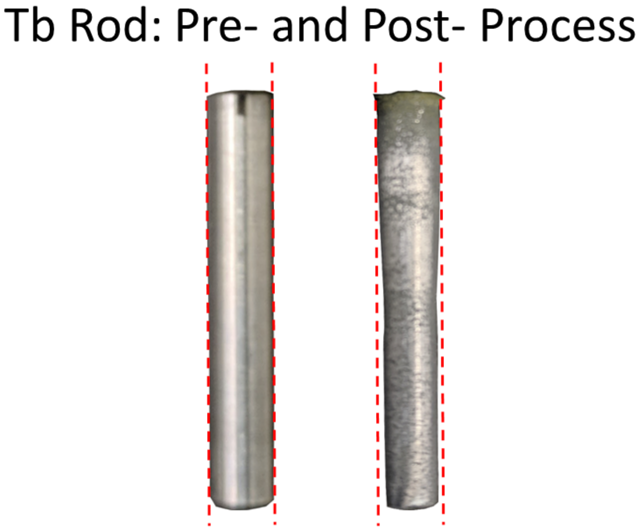
Tb Rod: Pre- and Post- Process

Figure 6.16: Photographs of Tb anode before and after experimental campaign

Measuring anode depletion was not taken into consideration when designing the experiments, therefore experimental data was not available to model. It would have been ideal to use a micrometer to measure circumference change along the length of the anode after each run, but moving electrodes in and out of the cell after each experiment would have introduced more uncertainty between tests by changing surface areas, changing temperatures and possibly removing salt. Another option could have been to use the initial and final geometries to estimate the change for each run. The anode depletion was estimated in ERAD using the final mass of the anode calculated at the end of one run in the output file *outblk3*, and using that as the initial anode mass for the next run in the *inpref* file. The initial anode mass in the ERAD simulations for test 1 was 13.0 g and the final anode mass was 11.4 g at the end of test 8.

The electrolyte mass was changed similarly, using the electrolyte content results in output file *outblk2*. The initial electrolyte mass was 49.8 g and the final electrolyte mass was

Table 6.19: Species specific input parameters for experimental ERAD simulations

	Tb^{3+}	**Gd^{3+}**
E^0 (V)	-2.108	
D (10^{-5} $cm^2\,s^{-1}$)	0.822 [86]	1.13 [87–89]
i ($A\,cm^{-2}$)	1	0.8
α*	0.5	0.5
Anode (wt.%)	100	0
Electrolyte (wt.%)	1	Varied

*commonly assumed value for α

Table 6.20: Sensitivity test values for Gd apparent potential

Test No.	**$E^{0'}_{Gd}$**	**Test No.**	**$E^{0'}_{Gd}$**
τ 1	2.202	τ 4	2.146
τ 2	2.183	τ 5	2.127
τ 3	2.164	τ 6	2.108

50.7 g. The composition of the electrolyte matched the experimental composition of the electrolyte as measured in Table 6.11 for each run.

The input parameter for the apparent potential of Tb, *stde*, was determined from OCP measurements from test 1, Tb 1.0 wt.% in TbCl3-LiCl-KCl eutectic electrolyte, where the potential was measured as -2.108 V vs. 5-mol wt.% Ag|AgCl.

To explore how the apparent potential affects concentration predictions in ERAD, a sensitivity study was conducted varying the input parameter for Gd apparent potential, $E^{0'}_{Gd}$. The initial potential was determined from OCP measurements of a Gd rod where $E = -2.202V$ and the test values $\tau 1 - 6$ are shown in Table 6.20.

Experiments 2 - 8 were simulated in ERAD six times using E_{Gd} = 2.202, 2.183, 2.164, 2.146, 2.127 and 2.108 V. The output files, *outblk3*, containing the cathode content in wt.%, were compared to the experimental results. The results of the sensitivity study are plotted in Figure 6.17.

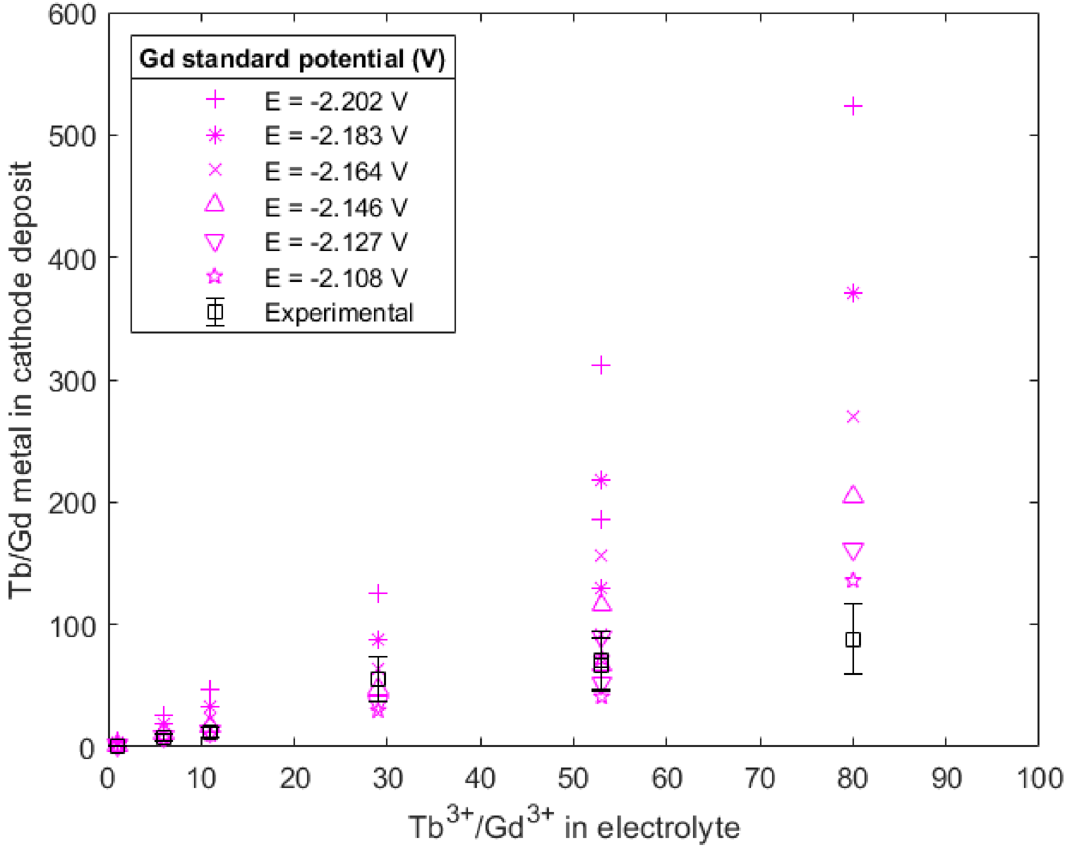

Figure 6.17: Standard potential sensitivity study

Within the experimental uncertainty range, $E_{Gd} = -2.127$ V agreed with the experimental results in all the tests except number 2 with the Tb/Gd ratio of about 80; ERAD predicted much higher ratios. $E_{Gd} = -2.108$ agree in 4 tests. $E_{Gd} = -2.146$ agree in 3 tests. $E_{Gd} = -2.164$ only agree in 1 test. $E_{Gd} = -2.202$ does not agree with any of the experimental Tb/Gd metal ratios.

6.2.2 Comparison of Experiments and Simulations

The Tb/Gd in the metal cathode deposits was compared to the Tb/Gd ratios from the cathode content from the ERAD simulations and was plotted in Figure 6.18.

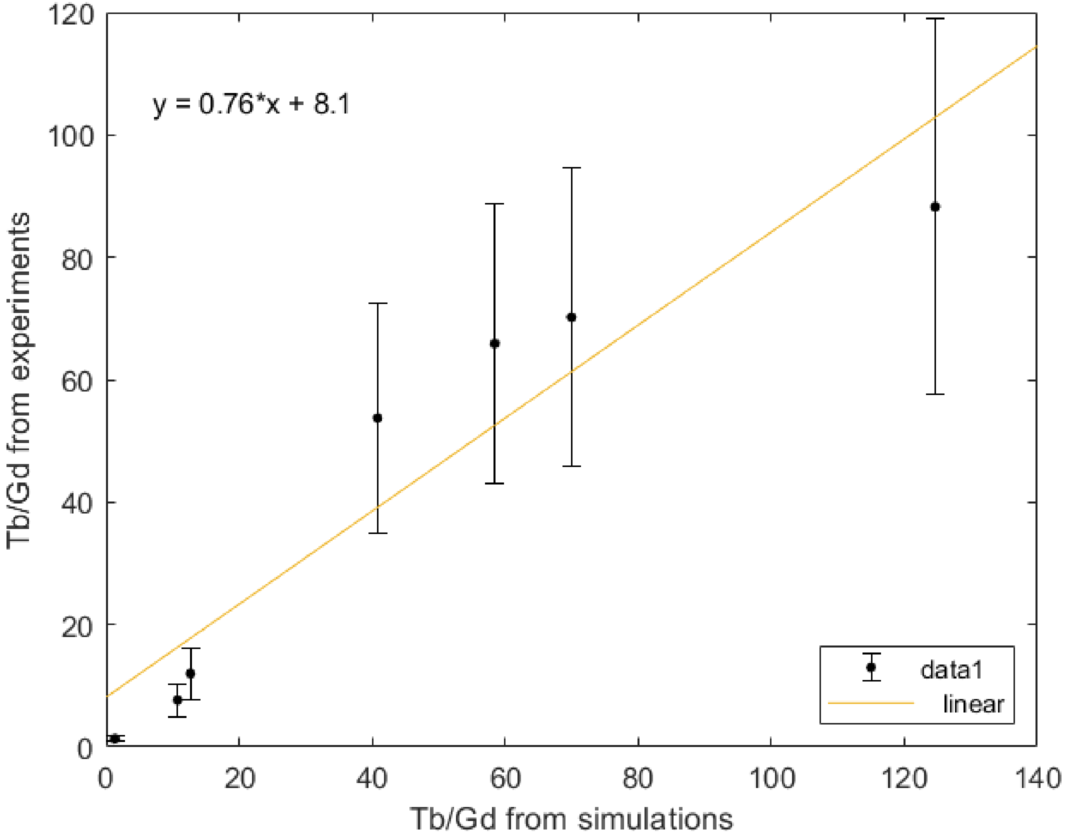

Figure 6.18: The cathode Tb/Gd ratio from experiments versus Tb/Gd ratio from the simulations with $E_{Gd} = -2.127$ V

Using the optimized apparent potential of $E_{Gd} = -2.127$ V for Gd, the Tb/Gd ratios from the simulations correspond with the experimental results within their uncertainty range, except for Test 2.

6.2.3 Input parameter discussion

ERAD successfully predicted Pu and Cm ratios in the salt and at the cathode that were in good agreement with the experimental electrodeposition results. The sensitivity test improved those findings and revealed how changes in the apparent potential improved ERAD performance. The refined E_{Gd} of -2.127 V makes the potential difference between

Tb and Gd 0.019 V. The difference in apparent potential between the two analytes under investigation is the main parameter that determines their separation factor in varying concentration conditions. Keeping that potential difference constant will yield useful results when simulating other systems including large-scale facilities.

The apparent potential is highly dependent on the electrochemical system used. Temperature, WE surface area, and electrolyte mixture all affect the apparent potential and may vary from one electrochemical system apparatus to another. Bagri et al. developed a method for determining the Raoultian standard state potentials of pure supercooled chlorides that are independent of electrolyte medium and are functions of temperature which makes them useful for comparing baseline potentials of different species[90]. Using Bagri's method and the thermodynamic database of pure substances for Tb[91], the Raoultian standard state potential for Tb was found to be -2.778 V, while the potential for Gd was calculated in the paper as -2.804 V[90]. The potential difference between Tb and Gd was found to be 0.026 V which is in good agreement with the value found from the refined ERAD results.

6.2.4 Limitations of ERAD

While ERAD was the most appropriate ER model to use to study electrochemical reactions in this research, it is prudent to note some of the limitations as they relate to this study.

ERAD does not do consecutive dynamic modeling[92]. To simulate an ER conducting several runs, the user must manually change the input file before each run. The parameters of significance for this type of simulation are the electrolyte composition and anode mass or geometry. The last line of the output files for these parameters must be copied and pasted into the new *inpref* file. To implement this feature for this work, a bash script was written; the bash script can be found in the Appendix.

ERAD does not simulate constant potential runs, only constant current. The exact constant potential experiments could not be simulated and were approximated by estimating the *inpref* input for current.

One of the major concerns was to determine the sensitivity of the modelâĂŹs result against the variation of input parameters[75]. A sensitivity analysis was performed on the apparent potential parameter and the results of the sensitivity test in Section 6.2.2 closely matched the experimental results. Conducting the sensitivity test and approximating a constant current ended up with satisfactory results, but the current was not constant in the actual experiment. There was great variation in the current over time as the surface area grew and the geometry changed.

The diffusion layer is modeled as a one dimensional line[78], but over time as the ions in the salt next to the cathode reduce, the diffusion layer grows and it takes longer for the ions to travel from the bulk solution through the diffusion layer and reduce on the cathode. In constant potential experiments, the change in current reflects the diffusion layer phenomena which in turn provides information about the rate at which reduction is occurring and this cannot be captured in ERAD.

ERAD models the entire electrode surface area as a single homogeneous area and assumes uniform growth on the cathode. ERAD does not take into account dendrite formation which affects current density along the surface of the electrode which affects deposition at different points along the cathode surface[75]. The electrolyte is modeled as a single homogeneous volume where all ions are distributed evenly. This is an ideal scenario, but the ions may be distributed in many different ways due to temperature gradients from uneven heating of the cell, more dense analytes may tend towards the bottom of the electrolyte, the electrodes are mechanically moved in and out of the cell and the mechanism by which they move may have some vibration which could introduce disturbances in the electrolyte. The static geometry assumptions are not reasonable.

ERAD models the anode and cathode in one dimension at a fixed distance, effectively modeling the electric field as infinite parallel plates with parallel field lines, as seen in Figure 6.19. This incorrectly assumes a very strong and uniform electric field and resistance is not taken into account.

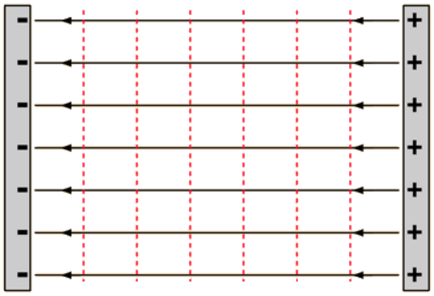

Figure 6.19: Parallel plate electric field

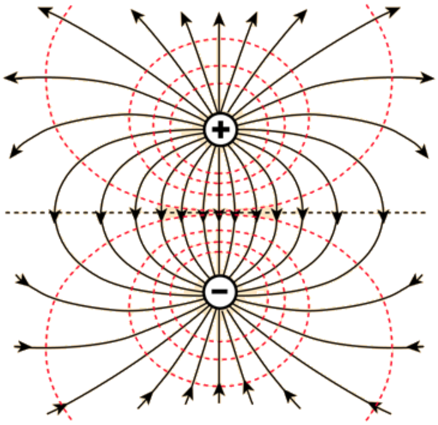

Figure 6.20: Electric dipole field

The experimental setup and and most basic real-world designs should be modeled more like an electric dipole field seen in Figure 6.20, or higher moments. Such a model might be able to account for the distance between electrodes and how that affects electric field strength.

Chapter 7

Safeguards Assessment

This chapter presents a safeguards assessment for a notional pyroprocessing facility that identifies the types of material being processed and the operating data to monitor for in each unit operation. An acquisition path analysis is conducted on a hypothetical misuse/ diversion path segment. The hypothetical misuse/ diversion path segment is then simulated in the KAPF+ reference facility using ERAD and an assessment is made about neutron signatures from the predicted electrolyte and cathode contents.

Identifying material types and their safeguards classification is a common first step for establishing safeguards approaches[8]. Material types of interest for safeguards are unirradiated direct use, irradiated direct use and indirect use material. Pu and Cm are expected to be found in the Fuel Chopper, Oxide Reducer, Electrorefiner, Electrowinner, Cadmium Distiller, and the Melting Furnace. In this acquisition path segment examined, Pu separation occurred in the ER. If the Pu to Cm ratio on the material coming into the facility is known, the Pu to Cm ratio method should be applicable and valid for the Fuel Chopper and Oxide Reducer unit operations located in MBA1. Once Pu is separated from Cm in the ER, there will be an unknown ratio of Pu to Cm moving into the Salt Distiller, Electrowinner, Cadmium Distiller, and the Melting Furnace and the efficacy of the neutron balance method is called into question if Cm does not follow Pu with the same ratio.

7.1 Acquisition path analysis

An acquisition path analysis is conducted on the misuse scenario in the ER[4, 93–95]. Formulating the scenario in this manner helps to explore possible concealment strategies and how to detect them with specific safeguards measures. The acquisition path segment that was modeled in ERAD was the misuse/ diversion path using the ER to separate Pu by codepositing it on the U product cathode. The ER was operated to increase Pu concentration in the U metal product by limiting UCl_3 additions and not cleaning the salt. The main proposed safeguards measures are NMA using the neutron balance method, video and radiation monitoring and process monitoring of the ER cell. Possible concealment scenarios involve adding a non-Cm neutron emitter to conceal the movement of Cm and Pu, and add non-UCl_3 replacement to the salt to beat the video monitoring. The acquisition path segment involving the misuse of the ER and diversion of material is shown in Table 7.1.

This scenario involves no salt cleanup and limits the amount of UCl_3 recharge to encourage Pu reduction on the cathode. Proposed safeguards measures are measures that would be in place to detect the acquisition path segment. Possible concealment scenarios are actions taken to deceive the safeguards measures. Residual anomalies are signatures that could be expected from the concealment scenarios. Timeliness refers to the time-scale of the different safeguards measures.

ERAD simulations were conducted to better understand material composition in the electrolyte and at the cathode in this acquisition path analysis segment and to see if neutron counting is a good method for making those distinctions.

Table 7.1: Diversion/misuse of ER to separate Pu

Acquisition Path Segment	**Proposed Safeguards Measures**	**Possible Concealment**	**Residual Anomalies**	**Timeliness**
Operate ER to increase Pu conc. in U metal product	NMA - Pu/Cm ratio	add non-Cm neutron source to ER salt	excessive neutrons	PM, NRTA
limit UCl_3 additions	integrated video and radiation monitoring	Spurious UCl_3 replacement	ER PM exceeding normal operating boundaries	Video and radiation monitoring
no salt cleanup	ER PM, cell voltage, cell current, total charge, UCl_3 concentrations, salt level			NMA would not see diversion until end of material balance

7.2 Engineering-scale Simulations

The commercial facility modeled was the Korea Advanced Pyroprocess Facility Plus (KAPF+). The KAPF+ consists of 2 modules with a capacity of 200 MTHM/year for treating PWR SF. Each module consists of 4 ERs processing about 125 kgHM/day operating for 250 days per year[40]. One operation day is 24 hours. The KAPF+ processes PWR SNF cooled for more than 10 years. The fuel referenced is the Hanbit (former Yonggwang) Unit 3 & 4 (PLUS7) which has typical features of 16 x 16 rod array, initial enrichment of 4.5 wt%, and burnup of 50,000 MWd/MTU with a Pu/Cm ratio of about 300[20].

Using the proposed operating plans from Ko et al., the simulations processed new batches of the reference SNF for 24 hours, electrorefining 20 consecutive batches of SNF before

Table 7.2: General operating input parameters for KAPF+ simulations

Description	**Input parameter**
Temperature	773
Elements	U, Pu, Cm, K, Li, Cl
Time	24 h
Current	1800 A
Anode surface area	3748 cm^2
Anode initial mass	125 kg
Cathode surface area	800 cm^2
Electrolyte initial mass	1000 kg

the electrolyte salt is moved to the electrowinner[20]. The abnormal operation involved not adding the UCl_3 refresher before each new run. The final electrolyte composition from one run was used as the initial electrolyte composition for the next run in order to see how Pu and Cm accumulate in the electrolyte salt and deposit on the cathode.

The *inpref* input parameters for the KAPF+ ERAD simulations are listed in Table 7.2.

It is not clear how the KAPF+ ER will be run to fully oxidize 125 kg of SNF in 24 hours but the ER design will likely include multiple cathodes surrounding the spent fuel anode and ERAD only provides a limited approximation of mass transport in an ER, especially for larger scale operations. The current density for these ERAD simulations was determined through trial and error using past ERAD simulation work [13, 77] as starting points. The values for current density to be on the order of 0.01 to 1.0 $\mathrm{A\,cm^{-2}}$ were not enough to fully oxidize the anode. Using only one cathode in ERAD, the current was set at 1800 A to operate with a current density of 2.25 $\mathrm{A\,cm^{-2}}$, which fully oxidized U in the anode.

Knowing the expected operating current of the KAPF+ would be valuable to further

Table 7.3: Species-specific input parameters for KAPF+ simulations

	$\mathbf{U}^{3+}$	$\mathbf{Pu}^{3+}$	$\mathbf{Cm}^{3+}$
E^0 (V)	-2.501[83]	-2.76[83]	-2.779[50]
D (10-5 cm2 s-1)	2[83]	1.12[83]	2.41[50]
i (A cm-2)	1[83]	0.8[83]	0.8*
α	0.5	0.5	0.5
Anode (wt.%)	98.9	1.04	0.0034
Electrolyte (wt.%)	7	2	0.2

assumed value

assess ERAD's ability to predict mass transport behavior accurately.

The input parameters specific to U, Pu and Cm in LiCl-KCl-UCl_3-$PuCl_3$-$CmCl_3$ system are listed in Table 7.3.

Using the results from the experimental simulations, the apparent potential difference for Pu and Cm was set to 0.019 V. To maximize anode dissolution within the 24-hour cycle, the current density was set to $2.25\,\mathrm{A\,cm^{-2}}$, which meant the current was set to 1800 A. The results for Pu and Cm weight fractions and Pu/Cm ratios in the electrolyte and cathode are listed in the Table 7.4

Table 7.4: Pu and Cm in the electrolyte and cathode at the end of each cycle

Cycle	**Electrolyte**			**Cathode**		
No.	**Pu (wt.%)**	**Cm (wt.%)**	**Pu/Cm**	**Pu (wt.%)**	**Cm (wt.%)**	**Pu/Cm**
0	2.00	0.200	10.0	0.00	0.00	1.00
1	2.14	0.201	10.6	0.00	0.00	1.00
2	2.28	0.201	11.3	0.00	0.00	1.00
3	2.42	0.202	12.0	0.00	0.00	1.00
4	2.56	0.204	12.6	0.00	0.00	1.00
5	2.71	0.205	13.2	0.00	0.00	1.00
6	2.85	0.206	13.8	0.00	0.00	1.00
7	3.00	0.208	14.4	0.00	0.00	1.00
8	3.15	0.209	15.1	0.00	0.00	1.00
9	3.29	0.210	15.7	0.00	0.00	1.00
10	3.44	0.212	16.3	1.84×10^{-3}	0.00	2.36×10^{7}
11	3.42	0.213	16.1	1.28	0.00	1.63×10^{10}
12	3.16	0.215	14.8	3.07	0.00	3.93×10^{10}
13	2.87	0.216	13.3	3.29	0.00	4.21×10^{10}
14	2.57	0.217	11.8	3.31	0.00	4.23×10^{10}
15	2.27	0.219	10.4	3.30	1.93×10^{-8}	1.71×10^{8}
16	1.97	0.220	8.95	3.30	1.93×10^{-8}	1.71×10^{8}
17	1.67	0.222	7.52	3.29	1.68×10^{-4}	1.95×10^{4}
18	1.36	0.223	6.11	3.28	1.06×10^{-3}	3.10×10^{3}
19	1.06	0.224	4.72	3.26	3.13×10^{-3}	1.04×10^{3}
20	0.754	0.225	3.35	3.23	7.54×10^{-3}	428
21	0.467	0.207	2.25	3.09	0.139	22.2
22	0.217	0.145	1.50	2.80	0.451	6.22
23	0.035	0.037	0.961	2.31	0.772	2.99
24	0.003	0.002	1.92	1.26	0.254	4.96

Given the off-normal conditions where UCl_3 is not replenished and the salt is not removed and replaced with clean salt, the first time Pu codeposits on the cathode with U is cycle number 10, but Cm does not codeposit until cycle number 15. The Pu/Cm ratio on the cathode at the end of cycle 15 is 1.71×10^{8} and the Pu/Cm ratio in the electrolyte is 10.4. [1] The electrolyte salt is supposed to move to the electrowinner after 20 batches are processed, but if it is not moved Pu and Cm continue to accumulate in the salt bath and the Pu/Cm ratios at the cathode and the electrolyte will not come within an order of magnitude of each other until cycle 22. The simulation results reveal that

---

[1] The ratio is not infinity for cycles 10 to 14 because ERAD does not allow 0 as an input in the *inpref* file; it is approximated as 1×10^{-9}.

the Pu/Cm ratio in the cathode is not the same as the ratio in the electrolyte which means the neutron balance method will not be effective under this abnormal operating condition.

To better illustrate the difference in the Pu/Cm ratio in the cathode versus the electrolyte, a semi-log plot of the ratios for cycles 15-24 are displayed in Fig. 7.1.

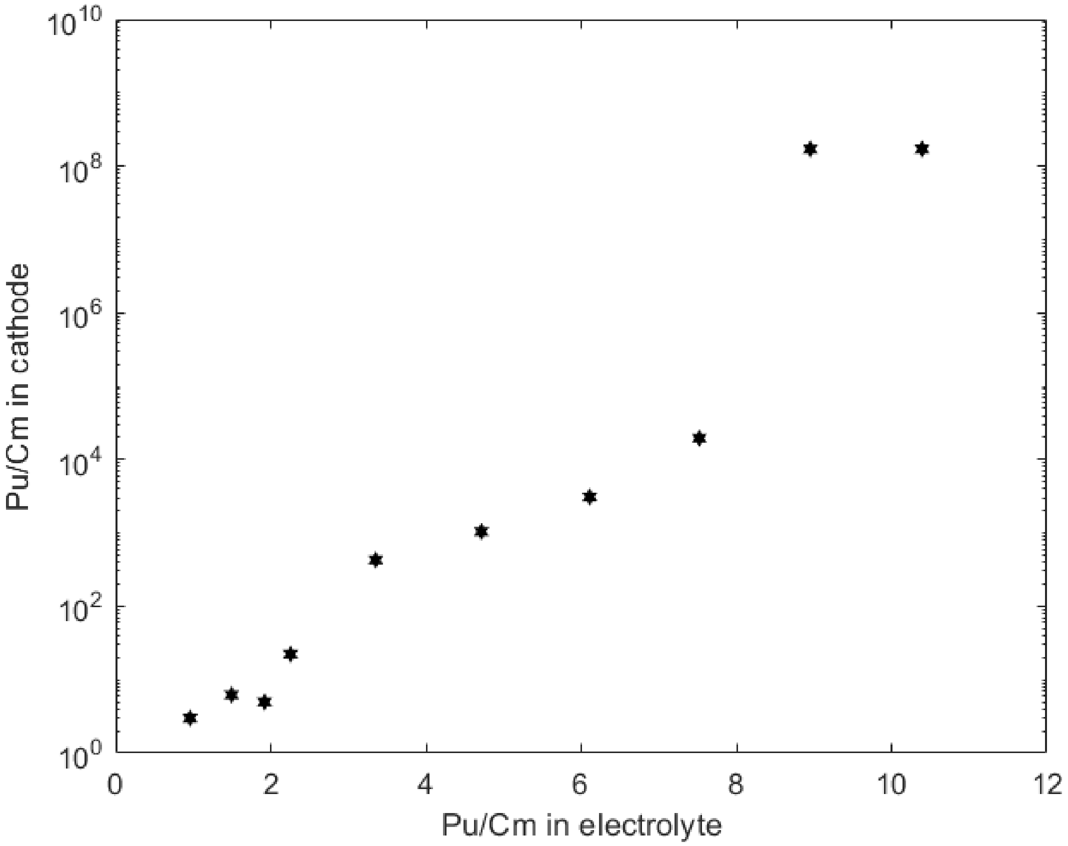

Figure 7.1: Semi-log plot of Pu/Cm ratio in the cathode versus electrolyte from KAPF+ runs 15 - 24

The Pu/Cm ratios between the electrolyte and the cathode are not consistent. This scenario is an extreme approximation and is meant to illustrate what can happen if Pu and Cm accumulate in the electrolyte salt without UCl_3 being replenished and without salt cleanup. According to these results, the neutron balance method relying on a constant Pu/Cm ratio during all processing is not a sufficient safeguards approach. The ERAD simulations and experiments concluded that this acquisition path segment will lead to codeposition at the cathode. While the neutron balance ratio method is not adequate for tracking Pu as it is processed in the ER, neutron measurements on the cathode deposit may still prove useful to indicate that Pu is present where it is not supposed to be.

7.3 Neutron Measurements

The elemental composition of the cathode from the KAPF+ ERAD simulations were used along with isotopic composition information from an ORIGEN calculation similar to the modeled PWR SNF with an initial enrichment of 4.5 wt%, and burnup of 50,000 MWd/MTU with 10 year cooling time[96]. These isotopic compositions are displayed in Table 7.5 with representative isotopic weight percents of U, Pu, and Cm and their SF yields.

The amount of Pu in the cathode at the end of cycle 10 from the KAPF+ ERAD simulation was 2.36 g. Using the standard SF yield data from Table 7.5, the expected neutron counts for Pu and U in the cathode from cycle 10 were calculated and tabulated in Table 7.6.

The total SF yield from 1.3×10^5 g of U was 1717.14 n/s, which was the expected amount under normal operating conditions. The total SF yield from 2.4 g of Pu was 1053.90 n/s, nearly doubling the amount of neutrons emitted from the cathode. The additional neutrons from Pu provided a signature of an off-normal event. While 2.4 g of Pu was below the significant quantity amount 8 kg, the Pu from this particular electrodeposition run should be accounted for to obviate potential protracted diversion strategies.

Cycle 15 is the first time Cm codeposits on the cathode with U and Pu. The SF yields are calculated in Table 7.7.

The SF neutron contribution from Pu in cycle 15 is 3 orders of magnitude greater than

Table 7.5: Standard spontaneous fission yields of U, Pu and Cm isotopes[51]

	iso	**wt%**	**Standard SF yield (n/s-g)**
U	92232	5.3×10^{-10}	1.3
	92233	7.4×10^{-9}	8.6×10^{-4}
	92237	1.9×10^{-11}	
	92234	1.9×10^{-4}	5.0×10^{-3}
	92235	9.5×10^{-3}	3.0×10^{-4}
	92236	5.5×10^{-3}	5.5×10^{-3}
	92238	9.8×10^{-1}	1.4×10^{-2}
Pu	94238	2.1×10^{-2}	2.6×10^{3}
	94239	5.8×10^{-1}	2.2×10^{-2}
	94240	2.7×10^{-1}	1.0×10^{3}
	94241	6.0×10^{-2}	5.0×10^{-2}
	94242	7.0×10^{-2}	1.7×10^{3}
Cm	96242	5.7×10^{-5}	2.1×10^{7}
	96243	7.4×10^{-3}	
	96244	8.5×10^{-1}	1.1×10^{7}
	96245	1.3×10^{-1}	
	96246	1.3×10^{-2}	

U. Neutron counting will very easily detect Pu in this codeposition scenario. The contribution from Cm is well below that from Pu and U.

The accumulation of actinides in the electrolyte salt from consecutive electrorefining yielded large neutron counts, mainly from 244 Cm. The high neutron counts could make it difficult to detect changes in electrolyte salt composition. Table 7.8 displays the calculated neutron yields in different unit operations if the electrolyte salt was transferred out of the ER and into the EW for further processing.

The neutron yields in the Electrorefiner, Electrowinner, Cadmium distiller, and Melting Furnace are dominated by 244 Cm in the electrolyte salt. Both the small and large

Table 7.6: Spontaneous fission neutron yields for Pu and U on cathode from KAPF+ ERAD simulations cycle 10

	Isotope	**Cathode content (g)**	**SF yield (n/s)**	**Total SF yield (n/s)**
Pu (2.4 g)	94238	4.8×10^{-2}	1.3×10^{2}	1053.90
	94239	1.4	3.0×10^{-2}	
	94240	6.3×10^{-1}	6.4×10^{2}	
	94241	1.4×10^{-1}	7.1×10^{-3}	
	94242	1.7×10^{-1}	2.8×10^{2}	
U (1.3×10^{5} g)	92232	6.7×10^{-5}	8.8×10^{-5}	1717.14
	92233	9.4×10^{-4}	8.1×10^{-7}	
	92237	2.4×10^{-6}	0.00	
	92234	2.4×10^{1}	1.2×10^{-1}	
	92235	1.2×10^{3}	3.6×10^{-1}	
	92236	7.1×10^{2}	3.9	
	92238	1.3×10^{5}	1.7×10^{3}	

diversions of neutron sources into the Salt Distiller had no effect on the total neutron counts from the Electrorefiner to the Electrowinner. Looking only at the neutron balance from the Electrorefiner to the Melting Furnace waste, the was no change in neutron count and therefore it could be incorrectly concluded that there was no change in elemental composition.

7.4 Safeguards implications

The acquisition path analysis revealed that a combination of multiple safeguards techniques will be needed to detect this scenario. Video and radiation monitoring will be needed to monitor the anode entering the electrochemical cell, the cathode leaving the electrochemical cell and the UCl_3 refilling the electrolyte.

Destructive analysis will need to occur on samples entering the ER and leaving the ER. This is the only way to determine the composition of the anodic feedstock. Once in the ER, the spent metal fuel will oxidize into the molten salt electrolyte bath. Due to the

Table 7.7: Spontaneous fission neutron yields for Pu and U on cathode from KAPF+ ERAD simulations cycle 15

	Isotope	**Cathode content (g)**	**SF yield (n/s)**	**Total SF yield (n/s)**
Pu (4.2×10^3 **g**)	94238	8.7×10^1	2.3×10^5	1.9×10^6
	94239	2.5×10^3	5.4×10^1	
	94240	1.1×10^3	1.2×10^6	
	94241	2.5×10^2	1.3×10^1	
	94242	3.0×10^2	5.1×10^5	
U (1.2×10^5 **g**)	92232	6.5×10^{-5}	8.5×10^{-5}	1.7×10^3
	92233	9.1×10^{-4}	7.8×10^{-7}	
	92237	2.4×10^{-6}	0.0	
	92234	2.3×10^1	1.2×10^{-1}	
	92235	1.2×10^3	3.5×10^{-1}	
	92236	6.9×10^2	3.8	
	92238	1.2×10^5	1.7×10^3	
Cm (2.5×10^{-5} **g**)	96242	1.4×10^{-9}	2.9×10^{-2}	2.3×10^2
	96243	1.8×10^{-7}	0.0	
	96244	2.1×10^{-5}	2.3×10^2	
	96245	3.1×10^{-6}	0.0	
	96246	3.2×10^{-7}	0.0	

dynamic nature of the facility, new fuel assemblies will be processed daily and depending on the facility layout, they will be separated into different ERs. Knowing the initial fuel composition entering the facility is helpful for overall material accounting of the initial and final material balance, but may do little for nuclear material accountancy in MBA 2 once multiple fuel assemblies are combined and separated into multiple ERs.

To implement the neutron balance method as a safeguards tool, the Pu/Cm ratio has to be measured at each unit operation. If only one SNF assembly is processed at a time and the facility is completely cleaned out before the next batch is processed, this method should work because the total neutron count at the beginning and at the end of the pyroprocess flowsheet should balance since no new material is being introduced, however this operational scenario may be impractical for the economic performance of the facility. However, the KAPF+ for example, has an operating cycle of 20 days, processing one SNF

Table 7.8: Total neutron yields in different unit operations at the end of cycles 10 and 15

	Unit operation					
Cycle No.	**ER**	**SD**$_{norm}$	**SD**$_{Abnorm}$	**EW**	**CD**	**MF**
10	1.87×10^{10}	1717	2771	1.87×10^{10}	1.87×10^{10}	1.87×10^{10}
15	1.89×10^{10}	1717	1.89×10^{6}	1.89×10^{10}	1.89×10^{10}	1.89×10^{10}

assembly per day (divided into multiple ERs) before the salt in the ER is removed and cleaned. Under these operating conditions, it might not be possible to keep track of the Pu/Cm ratio once SNF assemblies start mixing in the ER electrolyte.

One solution for keeping track of the Pu/Cm ratio on the mixed batched electrolyte could be to use DA on samples before every batch is processed. In the diversion scenario modeled, the ratio of Pu to Cm in the electrolyte for cycle 10 is 16 and 2.4 g of Pu deposit on the cathode, so 0.14 g of Cm are expected to deposit with it. The SF neutron yield for 0.14 g of Cm is 1.34×10^6 n/s. The amount of Pu to yield 1.34×10^6 n/s is 3 kg. Figure 7.2 shows the SF neutron yield versus Pu mass up to an SQ. The red reference line identifies the expected neutron yield (1.34×10^6 n/s) under the assumed Pu/Cm ratio.

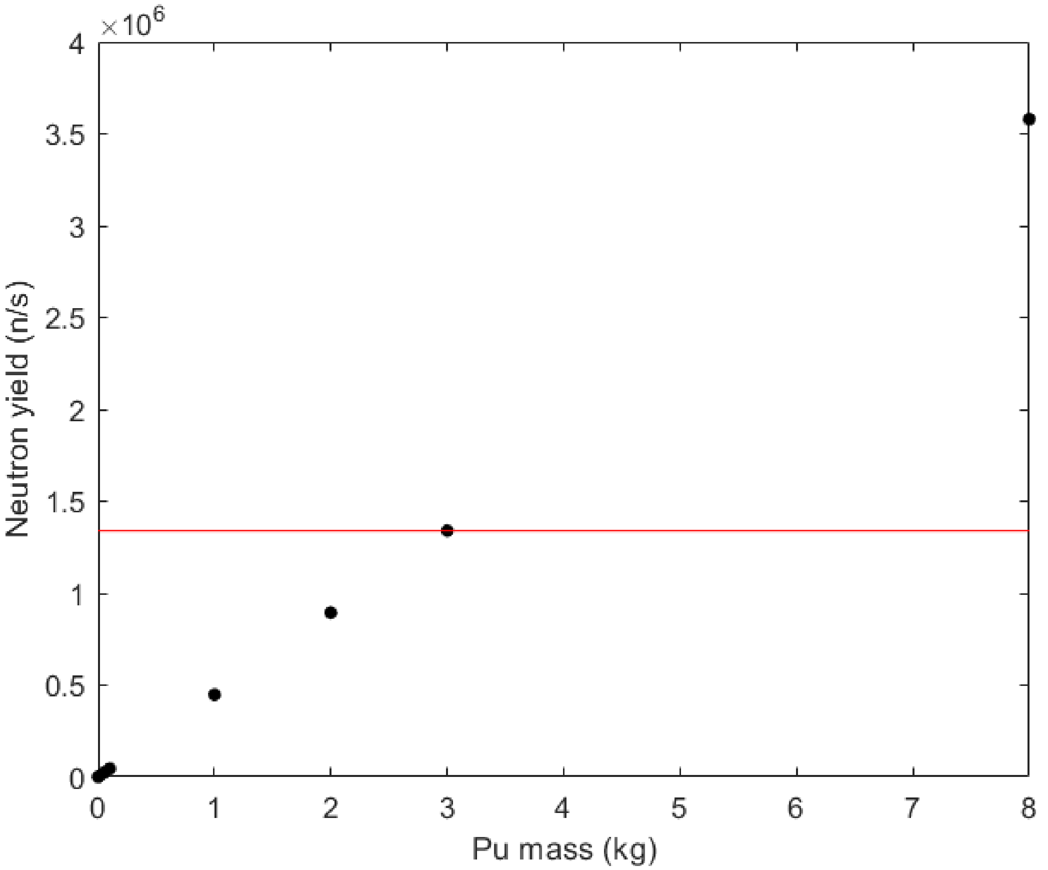

Figure 7.2: Neutron yield versus Pu mass with neutron count threshold for the modeled misuse/diversion scenario at cycle 10

If the assumption is that the Pu/Cm ratio in the electrolyte stays constant when Pu is diverted, when in reality it does not, this diversion scenario could result in up to 3 kg of Pu being diverted if only the neutrons are being counted. The inspector would reasonably assume 2.4 g were diverted, which would result in a miscalculation of 1250%.

Chapter 8

Conclusions

The electrochemical behaviors of Pu and Cm in the ER were investigated to determine if the neutron balance method could be used as a safeguards technique to track Pu in the ER. The neutron balance method relies on the assumption that ratio of Pu mass to Cm mass in the spent fuel remains constant throughout all unit operations.

This project determined that Tb and Gd were good surrogates for Pu and Cm to use in experimental electrodeposition tests. The experiments concluded that the Tb/Gd ratios in the electrolyte and the cathode deposit were inconsistent throughout the different electrodeposition tests. The ERAD simulations of the large-scale electrorefiner also found a discrepancy in the Pu/Cm ratio in the electrolyte versus the ratio in the cathode under different electrolyte concentrations.

The experimentally qualified ERAD results revealed that the neutron balance method is not an adequate safeguards option for the ER. This finding is significant because the literature review revealed that all proposed safeguards approaches for pyroprocessing facilities involves relying on the constant Pu/Cm ratio assumption to apply the neutron balance method.

If the Pu/Cm is known for each SNF assembly coming into the facility at the head end of the process, the method could work in MBA 1. If the ER is only processing one SNF assembly at a time and the molten salt and process lines are cleaned out before the next SNF assembly enters the ER, and the Pu/Cm ratio coming into the ER is known, then the Pu/Cm ratio method could work in the ER and for tracking Pu onto the other processes like the cadmium distiller and electrowinner and into the actinide waste stream.

However, if the ER is going to processes multiple SNF assemblies consecutively, as is planned for the KAPF+ for example, complications may arise when using the Pu/Cm ratio to track Pu.

As new anode baskets filled with SNF enter the ER, the ratio of Pu/Cm in the electrolyte changes, but not necessarily the total neutron count. The ERAD model predicts the total neutron count in the ER would stay relatively constant because Cm concentration does not fluctuate that much. Even in the diversion scenario modeled, only a very small fraction of Cm ended up codepositing with Pu on the U product cathode. Neutron counting data on the molten salt electrolyte will give an indication of system health at best, but will not be useful in keeping track of significant quantities (SQs) of Pu.

Passive neutron monitoring should be used with caution on the U product stream. The diversion scenario simulations revealed Pu codeposition without Cm for at least 5 cycles. If the inspector or operator works under the assumption that the Pu/Cm ratio is constant and measures neutrons as a way to estimate Pu mass, this could result in miscalculating several kg of Pu per batch processed; leading to an SQ of Pu being diverted after only 3 batches.

One of the proposed goals at the beginning of this research was to find electroanalytical techniques that could indicate Pu and Cm separation. The experiments revealed that when reduction potentials are very close the voltammetry probes may not be effective at distinguishing individual analytes and their concentrations in the electrolyte and at the cathode. The electroanalytical techniques used in this study do not give an indication of electrolyte concentration and therefore an assessment on PM options could not be made.

Other findings showed that ERAD can approximately simulate experimentally demonstrated phenomena and therefore ERAD could be used to model multi-component misuse and diversions scenarios to predict analyte concentrations in the electrolyte and cathode. The simulations and experiments conducted in this research qualify ERAD as an appropriate and useful tool for approximating off-normal scenarios in large-scale facilities. The value in conducting those simulations is in being able to test boundary conditions for parameters such as standard potential, current, concentration of analytes in the electrolyte, to see how they effect multi-component eletrochemical deposition. This helps establish a foundation for testing assumptions about material behavior and the applicability of specific safeguards techniques.

Knowing that the Pu/Cm ratio neutron balance method may not be effective for tracking Pu in the ER, creates a space for finding new ways to track Pu. This result may invalidate the need to do gross neutron counts on SNF bundles as they enter the pyroprocessing facility, and instead encourage a more direct sampling approach on incoming SNF.

Error propagation was a big part of this research. The more measurement techniques and sensors that were used to quantify material at any given step, increased the overall uncertainty of the final result. Adding more sensors to the safeguards system may not necessarily improve probability of detection. In fact it might decrease probability of detection due to compounding uncertainties.

Appendices

Appendix A

ERAD Bash Script

```
#!/bin/bash

# this is the function to make the input file
function create_input ()
{
  input1=$1
  input2=$2

  # paste the input file here, and replace the variable I want to
  # vary with $input1, $input2, etc
  cat << EOF
Stage 1 - PHD1 - 1000 MWe PWR in KAPF+
&input1
  !Temperature (keep at 773 kelvin unless other parameters are changed accordingly)
    temp=773.d0,
  !Number of elements being tracked in the system
    nelemt=6,
  !Element names, Case Sensitive for primary anode species, secondary anode species, and anion
```

```
!Rearranging means that you should probably edit ACTS.F and ACTM.F
  ename = 'Ur', 'Pu', 'Cm', 'Li', 'Ka', 'Cl',
!primary solid anode constituent
  enamePrimary = 'Ur'
!secondary solid anode constituent (if absent set dfrac to be large)
  enameSecondary = 'Pu'
!Only a single anion is allowed in the system
  enameAnion = 'Ka'
!Standard potentials (Reverse of conventional sign) (use the OCP result from experiments)
  stde = 2.501, 2.76, 2.779, 3.683, 3.865, -0.895,
!taken from CV paper and from (zr needs updated)
!Diffusion coefficients in liquid bismuth
  diffu1= 1.51d-5, 1.0d-5, 1.0d-9, 1.5d-5, 1.5d-5, 1.5d-5,
!Estimated
!Diffusion coefficients in molten salt
  diffu2= 2.0d-5, 1.6d-5, 1.27d-5, 1.5d-5, 1.5d-5, 1.5d-5,
!Standard exchange current densities (A/cm^2)
  curr0 = 1d0, 0.8d0, 0.4712d0, 5d-9, 5d-9, 5d-9,
!Species valance states
  zi    = 3.0d0, 3.0d0, 3.0d0, 1.0d0, 1.0d0, -1.0d0,
!Transfer coefficient for anode (alpha)
  tca   = 0.5d0, 0.5d0, 0.5d0,0.5d0, 0.5d0, 0.5d0,
!Transfer coefficient for cathode (alpha)
  tcc   = 0.5d0, 0.5d0, 0.5d0,0.5d0, 0.5d0, 0.5d0,
!initial cathode potential (Volts) [-0.5 to -3.0]
  catp= -1.0d0,
!initial anode potential  (Volts) [-0.5 to -3.0]
  anop= -1.0d0,
!End time of current 'steps' (hours)
  tset= 24.00,
  steptype=  0,
!Current setting for each current 'step' (Amps)
```

```
    ctrlvar= 1800d0,
  !ctrlvar= 1874d0,
  !Absolute error for Butler-Volmer Solver (recommended: less than 1d-16)
    aberr= 1.0d-35,
  !Solubility limit for elements in Cadmium pool (mole fraction)
    psolim= 0.0113d-2, 0.018d-2, 1.0d0, 1.0d0, 1.0d0, 1.0d0,
  !Cyclic voltammogram option: tmodi = 'cyclic'
  !  tmodi = 'cyclic'
  !CV scan rate (V/s) sign of number indicates starting direction
  !  sr = -.1
  !Cv start voltage, maximum voltage, and minimum voltage
  !  v = -1.000, -1.35, -1.8
  !Output coordinate for first column on tables (mnemonic X select) 1=coulombs passed, 2=time in seconds, 3=time in hours
    xsel = 2
  !Period between major outputs such as (plots of diffusion layers) unit selected by xsel
     outperiod = 100.
  !Supress CV output before tcrit
     osupress = .False.
  !Add column headings to output
     colheading = .TRUE.
  !.TRUE.=Write cathode contents to restart file/ .FALSE. Write original cathode contents to restart file
     writecathode = .TRUE.
  !Used to specify plot monitor of bulk compositions and concentrations 0=Off
     plotmonitorcon = 0
  !Used to specify to display plot monitor of surface plots 0=Off
     plotmonitorsurf = 0
  !used to specify which elements to monitor on the monitor plot.  For all element, input " ", example: 'Ur Pu Zr'
!      plotelelist = ''
```

```
!     plotelelist="La Pu Ur"
    plotelelist="Ur Li Ka Cl",
    nopas = .True.
/
&sanode
!Type of solid anode (3=cylinder, 2=cylinder with clad 0=liquid anode)
  !102 = cylinder with clad without geometry update (ie no layer formation)
  sflag = 102,
!Number of cells in Zr region
  nzr =  40,
!Initial mesh cell size in Zr region
  dy2o= 1.0d-5,
!Radius of fuel segment (cm)
  r0 = 0.4178,
!Height of fuel segment (cm)
  hi0 = 0.64d0,
!Number of chopped fuel segments
  ncfs = 3417,   !anode surface area
!Fraction of electrolyte diffusion coefficient in Zr region due to porous media (normally a guess)
  dfrac = 1   !Set to 1 to avoid discontinuity in the tiny layer cells that just sit there
!Set initialize to 90232 if you want to skip it. Set to 1 to run initialization
  initialize = 90232,
!Solubility limit in the salt
  slimcon = 1e14
/
&input2
!Size of anodic liquid metal diffusion layer [keep it the size of 1*dy in this code version] (cm)
  del(1)=10.0d-4,
!Size of anodic molten salt diffusion layer (cm)
```

```
  del(2)=15.0d-03,
!Size of cathodic molten salt diffusion layer (cm)
  del(3)=15d-03,
!Size of cathodic liquid metal diffusion layer [set to 1*dy if solid cathode] (cm)
  del(4)=10.0d-4,
!Mesh Size (cm)
    dy=10.0d-4,
!Contact area of anode-salt, cathode-salt, and pool-salt interfaces (cm^2)
  area= 3748d0, 800d0,
/
&INPUT3
!Solver settings.  Dont mess with them unless you edit the source code.
  ISTATE=1,
  ITASK=5,
  epslon=1.d-5
  iopt=1,
!Maximum number of computations per timestep.  (Has never helped the result)
  mxstep=100,
!First timestep size (seconds).  Keep it small
  h0=1d-15
!Keep this set to 5, which tells lsoda to compute a banded jacobian.
  jt=5,
!Matrix lower bandwidth.  Its minimum value seems to be 19 when using 10 elements.
!Smaller=faster bigger->more stable
!Smaller->faster bigger->more stable
  ml=17,
!Matrix upper bandwidth.
  mu=17,
!Maximum timestep
  hmax=500.0d0
```

```
  itol=1,
!LSODA/E relative tolerance
  rtoli=1.d-10
!LSODA/E absolute tolerance
  atoli=1.0d-11,
  iprint=2,
  zeroconc=1d-7
!  maxbvexp = 1d8
/
&input4
!Composition of anode (weight fraction)
  Can = 9.89d-01, 1.04d-02, 3.39419d-05, 1.0d-9, 1.0d-9, 1.0d-9,
!Composition of electrolyte (weight fraction)
  Cms= $1, $2, $3, $4, $5, $6,
  !cms = 0.07, 0.02, 0.002, 0.063885292, 0.250134475, 0.593980233,
!Composition of cathode (weight fraction)
 Cca=  1d-7, 1d-7, 1d-7, 1d-9, 1d-9, 1d-9,
!Composition of pool (weight fraction)
 Cpo=  1d-9, 1d-9, 1d-9, 1d-9, 1d-9, 1d-9,
!Composition of pool intermetallics (weight fraction)
 Cim=  1d-9, 1d-9, 1d-9, 1d-9, 1d-9, 1d-9,
!Composition of inlet stream (weight fraction)
 Cin=  1d-9, 1d-9, 1d-9, 1d-9, 1d-9, 1d-9,
/
&input5
!masses of anode, electrolyte, cathode, pool, and pool precipitate (g)
   mass= 125d3, 1000d3, 1.0d0, 1d-9, 1d-9,
! if vol specified, volume is used
! if dens specified, volume is calculated via density (g/cm^3)
!  dens = -19.1, -1.6387, -19.3, -1d-9, -1d-9,
! density taken from zr density paper in archives
  vol = 4950d0, 19800d0, 1.0d0, 1d-9, 1d-9,
!Atomic weights of the elements
```

```
  gatom= 238.03, 244, 247, 6.94, 39.1, 35.45,
/

#############################
#  Main script starts here  #
#############################

# create an empty data file
 > electrolyte_data
 > cathode_data
 > anode_data
# > curc_data

# set the first run (match experiment numbers)
electrolyte=(doesnt_matter 0.07 0.02 0.002 0.063885292 0.250134475 0.593980233)


# this is the main part of the code, it uses a for loop
for run in {1..20}; do

  echo "Running case $run"

  # create the input file
  create_input "${electrolyte[1]}" "${electrolyte[2]}" "${electrolyte[3]}" "${electrolyte[4]}" "${electrolyte[5]}" "${electrolyte[6]}" > inpref

  # run the code
  ../erad.x > output_file

  # steal the last line
  electrolyte=($(tail -n1 outblk2))
  cathode=($(tail -n1 outblk3))
```

```
  anode=($(tail -n1 outblk1))
# curc=($(tail -n1 outcurc))

  # append it to a new file
  echo ${electrolyte[@]} >> electrolyte_data
  echo ${cathode[@]} >> cathode_data
  echo ${anode[@]} >> anode_data
# echo ${curc[@]} >> curc_data

  #multiply the electrolyte output by 100
  len=${#electrolyte[@]}
  for (( i=0; i<len; i++))
  do
    electrolyte[$i]=`python -c "print ${electrolyte[$i]}/100.0"`
  done

  # change E's to d's
  electrolyte=(`echo ${electrolyte[@]} | sed -e s/E/d/g`)

  # save the input and output files
  #mv inpref inpref.$run
  #mv outblk2 outblk2.$run
  #mv outblk3 outblk3.$run
  #mv outblk1 outblk1.$run
  #mv outcurc outcurc.$run
  #mv output_file output_file.$run

done
```

kapfauto.sh

Appendix B

Signature Based Safeguards (SBS)

Several publications have demonstrated benefits from using process monitoring (PM) on nuclear facilities as a complementary safeguards measure to NMA[16, 23, 29, 46]. More recently, this concept has been expanded and preliminarily demonstrated for pyroprocessing technology. The concept of Signature Based Safeguards (SBS) is part of this expansion and is being developed by the University of New Mexico and the University of Utah[13, 23, 24, 77]. SBS is built around the interpretation of input from various sensors in a declared facility coupled with complementary NMA methods to increase confidence and lower standard error inventory difference (SEID)[36, 47]. This works provides a framework for applying SBS to monitor the Pu/Cm ratio in the salt and the cathode.

The concept of SBS is built around the interpretation of input from various sensors in a declared facility coupled with complementary NMA methods to increase confidence and lower SEID[13, 24, 47]. SBS relies on real time or near real time data collected from PM sensors coupled with NMA methods to draw safeguards conclusions. A preliminary evaluation framework for comparing an all-inclusive set of PM technologies suitable for pyroprocessing has been developed.

PM, as defined by the IAEA, is an element of a safeguards approach that monitors material, processes, and equipment (nuclear and nonnuclear) in all types of nuclear facilities through independent and/or shared safeguards-relevant operator measurements[14]. PM uses process control measurements to detect abnormal plant operation. Process control measurements are those used by the operator to control processes such as flow rates, density measurements, and concentrations. The IAEA uses three levels of classification to evaluate data. At level one, these data provide the state of health of the system. This information can be used to arrange timely responses to indications that the monitoring system is malfunctioning or being tampered with. Level-two data provide a summary that will be used to prepare for inspection activities and assist in scheduling short noticed inspections. Level-three data is more detailed and can be useful in drawing safeguards conclusions[14]. PM differs from traditional NMA in that it strives for a real-time understanding of facility or unit operation activities associated with the control of material as it moves through the process as opposed to focusing on the strict accounting of nuclear material in process vessels. The use of these data for PM as a central part of a safeguards approach provides a higher level of operational transparency in a timely manner especially for high throughput facilities. For this reason, PM is increasingly important in nuclear safeguards as a supplement to mass-balance-based NMA. The main goal for using PM in addition to NMA is to improve the ability to detect off-normal plant operation, which could indicate diversion of SNM.

The two different approaches to applying PM to safeguards are process centric and the system centric. The process centric approach analyzes the response from assorted sensors throughout the facility and notes abnormalities or deviations from the normal mode of operation[29]. The system centric approach can be thought of as a two-layer monitoring system looking at both specific unit operations and the system as a whole; assessments are based on the data integration of both layers. Garcia et. al. described a system centric PM approach that uses statistics to infer occurrences of anomalies[23]. By running the output measurements of a network of multimodal sensors through a data analysis algorithm, abnormal operations can be detected and the plant can be analyzed to determine if material has been diverted [47]. SBS uses physics-based models in the system centric approach. Diversion scenarios are simulated to obtain specific signatures for diversion rather than using statistical inferences to estimate the amount of material unaccounted for[24, 82].

One main interest for PM technology is to detect operational anomalies as the process progresses rather than measuring mass balance inconsistencies resulting from abnormal activities after the process is over. These anomalies can indicate a number of scenarios and not all of them necessarily lead to a safeguards significant event. Anomalies of interest for detection may represent undesired plant operations and are defined by specific signatures, such as patterns of events occurring at different locations of the monitored facility and at different stages of operations. Under PM, sensors are deployed to observe unit operations comprising the monitored facility. The sensor data are collected by unattended online/in-vessel measurement and monitoring systems, which may have automated data collection and computer-assisted data analysis capabilities. The data collected and/or analyzed by the monitoring systems are then processed to detect and track the occurrence of anomalies of interest[15].

The evaluation framework begins with defining the major unit operations that determine process and facility operational states (normal or off-normal). Each unit operation was evaluated for how it can be misused to produce or separate SNM. Signatures of misuse were identified along with ways to measure them. Identifying these measurement types is an integral part of building a safeguards framework. The interplay of measurements made for tracking the operational state of a unit operation, or a set of such operations along with traditional nuclear safeguards elements form the basis for the SBS concept.

Eight unit operations are identified: fuel chopper (FC), oxide electroreducer (OR), electrorefiner (ER), salt distiller (SD), ingot caster (IC), electrowinner (EW), salt separator (SS), and waste producer (WP). Measurement technology, or sensors, to monitor batch transfers between unit operations was identified. The sensors are categorized as out-of-salt sensors (OSS), in-salt senors (ISS), and off-gas sensors (OGS), and inventory management (IM) techniques depending on how they will be used. A sensor network for each unit operation is depicted in Fig. B.1.

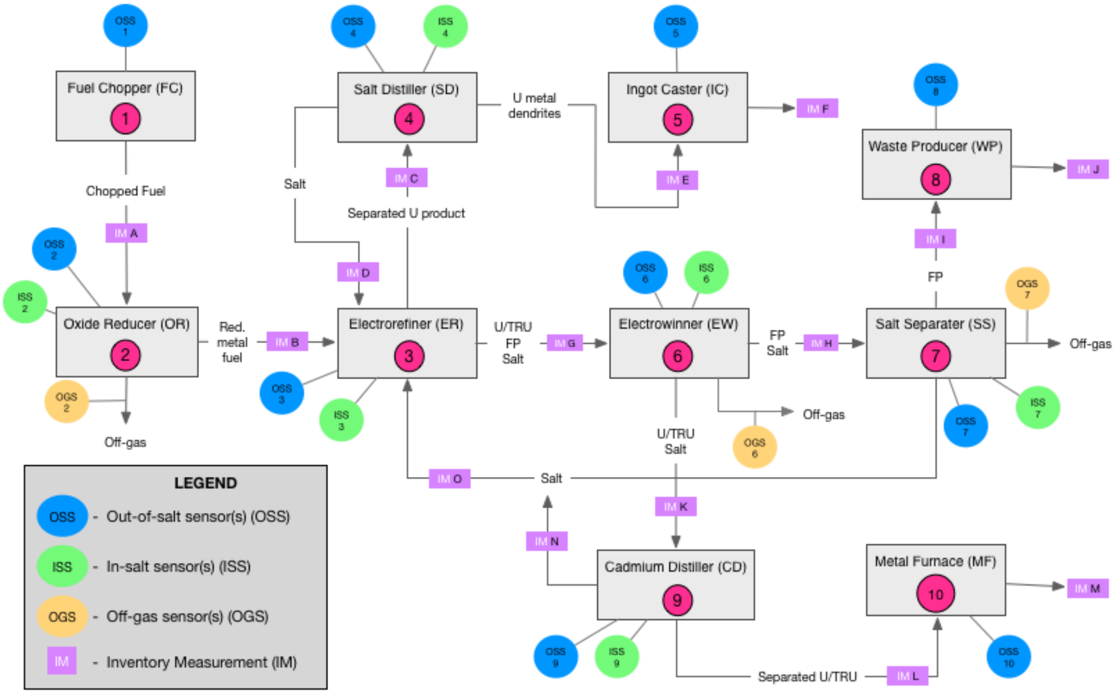

Figure B.1: Pyroprocessing Sensor Network

Table B.1 identifies the properties that the sensors monitor in each unit operation. For example, argon would be monitored by an OSS in the ER and salt density would be monitored by an ISS in the ER.

There are 15 inventory measurement (IM) points, labeled A through O in Fig. B.1. The different IMs describe points at which material accounting should be done because these are the material transfer points in between unit operations.

Table B.1: Operational Status Properties of Unit Operations

Unit Operation	OSS	ISS	OGS
1 Fuel Chopper	Radiation monitoring Scale		
2 Electroreducer	Argon monitoring Oxygen sensor Power supply Radiation monitoring	Electrode potential Salt concentration Salt density Salt level Stirrer speed Temperature	Flow rate Spectroscopic analysis
3 Electrorefiner	Argon monitoring Cathode scraper Oxygen sensor Power supply Radiation monitoring	Electrode current Electrode potential Electrode rotational speed Salt concentration Salt density Salt level Stirrer speed Temperature	
4 Salt Distiller	Argon monitoring Cathode morphology Mass of distilled salt Power Supply Radiation monitoring Vacuum and pressure sensor	Salt/metallic product concentration Temperature Volume of salt	
5 Ingot Caster	Fuel feeder vibration Ingot Morphology Mass of ingot Radiation monitoring Radiation signature		
6 Electrowinner	Argon monitoring Oxygen sensor Power supply Radiation monitoring	Electrode current Electrode potential Salt composition Salt density Salt level Temperature	Flow Rate Spectroscopic analysis
7 Salt Separator	Acoustic Sensors Oxygen sensor Phosphate mass Pressure Vacuum and pressure sensors Zeolite mass	Salt composition Salt level Salt density Temperature	Flow rate Spectroscopic analysis
8 Waste Producer	Mass Radiation sensors		

Bibliography

[1] N. Miura and H. Menlove, "The use of curium neutrons to verify plutonium in spent fuel and reprocessing wastes," Report LA-12774-MS, Los Alamos National Laboratory, 1994.

[2] P. Rinard and H. Menlove, "Application of curium measurements for safeguarding at reprocessing plants study 1: High-level liquid waste and study 2: Spent fuel assemblies and leached hulls," tech. rep., Los Alamos National Laboratory, 1996. LA-13134-MS.

[3] T. K. Li, S. Y. Lee, T. Burr, P. A. Russo, H. O. Menlove, H. D. Kim, W. I. Ko, S. W. Park, and H. S. Park, "Safeguardability of advanced spent fuel conditioning process," 45th Annual INMM Meeting, July 2004.

[4] P. Durst, I. Therios, R. Bean, A. Dougan, B. Boyer, R. Wallace, M. Ehinger, D. Kovacic, and K. Tolk, "Advanced safeguards approaches for new reprocessing facilities," tech. rep., Pacific Northwest National Laboratory, June 2007.

[5] H. R. Trellue, D. D. Dixon, H. O. Menlove, and R. J. Kapernick, *Neutron balance for integrated safeguards of a reprocessing facility.* Jun 2011.

[6] T.-H. Lee, Y.-S. Kim, T.-J. Kwon, H.-S. Shin, and H.-D. Kim, "Determination of the plutonium mass and curium ratio of spent fuel assemblies for input nuclear material accountancy of pyroprocessing, and analysis of their errors," *Nuclear Technology,*

vol. 179, pp. 196–204, August 2012.

[7] H. D. Kim, H. S. Shin, D. Y. Song, T. H. Lee, B. Y. Han, S. K. Ahn, and S. H. Park, "Application of safeguards-by-design for the pyroprocessing facilities in the rok," *Journal of Nuclear Materials Management*, vol. XL, no. 4, pp. 24–31, 2012.

[8] S.-K. Ahn, H.-S. Shin, and H.-D. Kim, "Safeguardability analysis for an engineering scale pyroprocess facility," *Journal of Nuclear Science and Technology*, vol. 49, no. 6, pp. 632–639, 2012.

[9] R. Bean, "Project report on development of a safeguards approach for pyroprocessing," Tech. Rep. INL/EXT–10-20057, Idaho National Laboratory, September 2010.

[10] S. X. Li, "Anodic process of electrorefining spent nuclear fuel in molten licl-kcl-ucl3/cd system," in *201st Meeting of the Electrochemical Society, 13th International Symposium On Molten Salts*, 2002.

[11] M. Gonzalez, L. Hansen, D. Rappleye, R. Cumberland, and M. F. Simpson, "Application of a one-dimensional transient electrorefiner model to predict partitioning of plutonium from curium in a pyrochemical spent fuel treatment process," *Nuclear Technology*, vol. 192, pp. 165–171, November 2015.

[12] R. Hoover, P. Lafreniere, and E. Blandford, "Commercial-scale pyroprocessing failure modes and implications for operations and safeguards," in *Transactions of the American Nuclear Society*, vol. 110, pp. 58–61, 2014.

[13] P. L. Lafreniere, D. S. Rappleye, R. O. Hoover, M. F. Simpson, and E. D. Blandford, "Demonstration of signature-based safeguards for pyroprocessing as applied to electrorefining and the ingot casting process," *Nuclear Technology*, vol. 189, pp. 173–185, February 2015.

[14] "Consultancy meeting on proliferation resistance aspects of process management and

process monitoring/operating data," September 2011. These issues were discussed during the lAEA sponsored meeting.

[15] T. Burr, S. Demuth, J. Howell, D. Leishman, G. Tompkins, and et al., "Status report for development of advanced process monitoring concepts for iaea safeguards sponsored by the next generation safeguards initiative (ngsi)," tech. rep., Los Alamos National Laboratory, February 2012.

[16] B. B. Cipiti, F. A. Durán, B. Key, Y. Liu, I. Lozano, and R. Ward, "Modeling and design of integrated safeguards and security for an electrochemical reprocessing facility," tech. rep., Sandia National Laboratories, 2012.

[17] H. Lee, G.-I. Park, J.-W. Lee, K.-H. Kang, J.-M. Hur, J.-G. Kim, S. Paek, I.-T. Kim, and I.-J. Cho, "Current status of pyroprocessing development at kaeri," *Science and Technology of Nuclear Installations*, vol. 2013, pp. 1–11, 2013.

[18] K.-C. SONG, H. LEE, J.-M. HUR, J.-G. KIM, D.-H. AHN, and Y.-Z. CHO, "Status of pyroprocessing technology development in korea," *NUCLEAR ENGINEERING AND TECHNOLOGY,*, vol. 42, no. 2, pp. 131–144, 2010.

[19] J. Ku, S. Moon, I. Cho, W. Choung, G. You, and H. Kim, "Development of pyroprocess integrated inactive demonstration facility," *Procedia Chemistry*, vol. 7, p. 779 âĂŞ 784, 2012.

[20] W. I. Ko, H. H. Lee, S. Choi, S.-K. Kim, B. H. Park, H. J. Lee, I. T. Kim, and H. S. Lee, "Preliminary conceptual design and cost estimation for korea advanced pyroprocessing facility plus (kapf+)," *Nuclear Engineering and Design*, vol. 277, pp. 212 – 224, 2014.

[21] C. Braun and R. Forrest, "Considerations regarding rok spent nuclear fuel management options," *Nuclear Engineering and Technology*, vol. 45, no. 4, pp. 427 – 438, 2013.

[22] K. A. E. R. Institute, “Pride pyroprocessing integrated inactive demonstration facility,” 2016.

[23] H. E. Garcia, M. F. Simpson, W.-C. Lin, T.-S. Yoo, and R. B. Carlson, “Detecting proliferation activities via system-centric integration and interpretation of multimodal data collected from a system of sensors,” in *Institute of Nuclear Materials Management 54th Annual Meeting Proceedings*, 2013.

[24] M. F. Simpson, D. Rappleye, E. D. Blandford, and H. E. Garcia, “Signature based safeguards alternative to nuclear material accountancy,” in *Institute of Nuclear Materials Management 55th Annual Meeting Proceedings*, 2014.

[25] INTERNATIONAL ATOMIC ENERGY AGENCY, *IAEA Safeguards Glossary.* No. 3 in International Nuclear Verification Series, Vienna: INTERNATIONAL ATOMIC ENERGY AGENCY, 2002.

[26] International Atomic Energy Agency, *Nuclear Material Accounting Handbook*, May 2008. IAEA Services Series No. 15.

[27] U. D. of Energy, “The nuclear fuel cycle,” August 2017.

[28] J. Carter, “Nuclear power policy statement on decisions reached following a review,” in *The American Presidency Projectc* (G. Peters and J. T. Woolley, eds.), April 1977.

[29] T. Burr, K. B. Sylvester, K. Myers, S. Demuth, A. Bakel, J. Krebs, S. Bryan;, C. Orton, M. Ehinger, H. Garcia, J. Howell, S. Johnson, M. Thomas, and J. Damico, “Roles for process monitoring in nuclear safeguards at aqueous reprocessing plants,” *Journal of Nuclear Materials Management*, vol. XL, no. 2, pp. 42–52, 2012.

[30] D. Horner, “South korean pyroprocessing awaits us decision,” *Arms Control Today*, vol. 39, July 2009.

[31] W. Moser and J. D. Navratil, "Review of major plutonium pyrochemical technology," *Journal of the Less Common Metals*, vol. 100, pp. 171 – 187, 1984.

[32] "Pyrochemical separations in nuclear applications, a status report," tech. rep., Nuclear Energy Agency, Organization for Economic Co-operation and Development, 2004. ISBN 92-64-022071-3.

[33] M. K. Goff and M. F. Simpson, "Dry processing of used nuclear fuel," in *Global, conference on sustainable strategies and future prospects for the nuclear fuel cycle industry*, 2009.

[34] Y. I. Chang, "The integral fast reactor," *Nuclear Technology*, vol. 188, no. 2, pp. 129–138, 1989.

[35] C. E. Till, Y. I. Chang, and W. H. Hannum, "The integral fast reactor - an overview," *Progress in Nuclear Technology*, vol. 31, no. 1/2, pp. 3–11, 1997.

[36] M. F. Simpson, "Developments of spent nuclear fuel pyroprocessing technology at idaho national laboratory," tech. rep., Idaho National Laboratory, March 2012.

[37] T. Inoue and L. Koch, "Development of pyroprocessing and its future direction," *Nuclear Engineering and Technology*, vol. 40, pp. 183–190, April 2008.

[38] N. Li, "Performance estimates for waste treatment pyroprocesses in atw," in *Second International Conference on Accelerator-Driven Transmutation Technologies and Applications*, 1997.

[39] G. H. N. Energy, "Ge hitachi advanced recycling center solving the spent nuclear fuel dilemma," 2009.

[40] S. Kim, W. Ko, S. Youn, R. Gao, Y. Chung, and S. Bang, "Advanced depreciation cost analysis for a commercial pyroprocess facility in korea," *Nuclear Engineering and Technology*, vol. 48, no. 3, pp. 733 – 743, 2016.

[41] "Processing of used nuclear fuel," Nov 2016.

[42] A. Diakov, "Status and prospects for russia's fuel cycle," *Science Global Security*, vol. 21, no. 3, p. 167âĂŞ188, 2013.

[43] T. ARC, "University of idaho senior design," January 2016.

[44] I. A. E. AGENCY, "The structure and content of agreements between the agency and states required in connection with the treaty on the non-proliferation of nuclear weapons." INFCIRC/153(Corrected), 1972.

[45] S. Li, R. Zarucki, and M. Pellechi, "The emerging safeguards challenges of pyroprocessing technology," in *Proceedings of Global 2011*, (Makuhari, Japan), December 2011. Paper 387547.

[46] H. E. Garcia, W. Lin, S. Johnson, T. Burr, S. Demuth, A. Bakel, J. Krebs, and M. Ehinger, "Integrated process monitoring based on systems of sensors for enhanced nuclear safeguards sensitivity and robustness," in *Institute of Nuclear Materials Management 52nd Annual Meeting Proceedings*, 2011.

[47] R. Wigeland, T. Bjornard, and B. Castle, "The concept of goals-driven safeguards," tech. rep., Idaho National Laboratory, 2009.

[48] M. Miller, S. Demuth, and J. Sprinkle, "Concepts and approaches for advanced safeguards and security," in *Proceedings of Global 2015*, (Paris, France), September 2015. Paper 5442.

[49] J. Serp, R. Konings, R. Malmbeck, J. Rebizant, C. Scheppler, and J.-P. Glatz, "Electrochemical behaviour of plutonium ion in licl-kcl eutectic melts," *Journal of Electroanalytical Chemistry*, vol. 561, no. 1, pp. 143–148, 2004.

[50] A. Osipenko, A. Maershin, V. Smolenski, A. Novoselova, M. Kormilitsyn, and A. By-

chkov, “Electrochemical behaviour of curium(iii) ions in fused 3licl-2kcl eutectic,” *Journal of Electroanalytical Chemistry*, vol. 651, no. 1, pp. 67–71, 2011.

[51] D. Reilly, N. Ensslin, and H. S. Jr., *Passive Nondestructive Assay of Nuclear Materials.* Office of Nuclear Regulatory Research U.S. Nuclear Regulatory Commission, March 1991. LA-UR-90-732.

[52] A. J. Bard and L. R. Faulkner, *Electrochemical Methods: Fundamentals and Applications.* John Wiley Sons. Inc., second ed., 2001. ISBN 0-471-04372-9.

[53] S. Editors, “Sparknote on introduction to electrochemistry.,” January 2017.

[54] I. U. of Pure and A. Chemistry, “Iupac compendium of chemical terminology (gold book) [online],” January 2018.

[55] I. Bioanalytical Systems, “Controlled potential electrolysis,” November 2017.

[56] D. S. Rappleye, *Electrochemical Concentration Measurements for Multianalyte Mixtures in Simulated Electrorefiner Salt.* PhD thesis, University of Utah, August 2016.

[57] D. A. Skoog, F. J. Holler, and S. R. Crouch, *Principles of Instrumental Analysis, Sixth Edition.* Thomson Brooks/Cole, 2007.

[58] I. Johnson, “The thermodynamics of pyrochemical processes for liquid metal reactor fuel cycles,” *Journal of Nuclear Materials*, vol. 154, pp. 169–180, June 1988.

[59] H. Nawada and N. Bhat, “Thermochemical modelling of electrotransport of uranium and plutonium in an electrorefiner,” *Nuclear Engineering and Design*, vol. 179, pp. 75–99, January 1998.

[60] S. Ghosh, B. P. Reddy, K. Nagarajan, and P. R. V. Rao, “Pragaman: A computer code for simulation of electrotransport during molten salt electrorefining,” *Nuclear Technology*, vol. 170, pp. 430–443, June 2009.

[61] R. O. Hoover, S. Phongikaroon, S. X. Li, M. F. Simpson, and T.-S. Yoo, “A com-

putational model of the mark-iv electrorefiner: Phase 1 - fuel basket/salt interface," *Journal of Engineering for Gas Turbines and Power*, vol. 131, pp. 054503–n, September 2009.

[62] R. O. Hoover, S. Phongikaroon, M. F. Simpson, S. X. Li, and T.-S. Yoo, "Development of computational models for the mark-iv electrorefiner - effect of uranium, plutonium, and zirconium dissolution at the fuel basket-salt interface," *Nuclear Technology*, vol. 171, pp. 276–284, September 2010.

[63] R. O. Hoover, S. Phongikaroon, M. F. Simpson, T.-S. Yoo, and S. X. Li, "Computational model of the mark-iv electrorefiner - two dimensional potential and current distributions," *Nuclear Technology*, vol. 173, pp. 176–182, February 2011.

[64] S. X. Li and M. Simpson, "Anodic process of electrorefining spent driver fuel in molten licl-kci-ucl3/cd system," *Minerals and Metallurgical Processing*, vol. 22, pp. 192–198, November 2005.

[65] S. X. Li, T. A. Johnson, R. W. Benedict, D. Vaden, and B. R. Westphal, "Integrated electrorefining efficiency test for pyrochemical fuel cycle," in *Transactions of the American Nuclear Society*, vol. 95, pp. 199–200, American Nuclear Society, 2006.

[66] T. Kobayashi and M. Tokiwai, "Development of trail, a simulation code for the molten salt electrorefining of spent nuclear fuel," *Journal of Alloys and Compounds*, vol. 197, pp. 7–16, June 1993.

[67] N. Li, "A kinetic model of mass diffusion limited electrowinning and electrorefining," tech. rep., Los Alamos National Laboratory, 1999. LA-UR-99-4659.

[68] B. Park, *A Time-Dependent Simulation of Molten Salt Electrolysis for Nuclear Wastes Transmutation.* PhD thesis, Seoul National University, Seoul, South Korea, 1999.

[69] M. Iizuka, K. Kinoshita, and T. Koyama, "Modeling of anodic dissolution of u-pu-zr

ternary alloy in the molten licl-kcl electrolyte," *Journal of Physics and Chemistry of Solids*, vol. 66, no. 2, pp. 427–432, 2005. Proceedings of the 11th International Conference on High Temperature Materials Chemistry (HTMC-XI).

[70] S. Choi, J. Park, K.-R. Kim, H. Jung, I. Hwang, B. Park, K. Yi, H.-S. Lee, D. Ahn, and S. Paek, "Three-dimensional multispecies current density simulation of molten-salt electrorefining," *Journal of Alloys and Compounds*, vol. 503, no. 1, pp. 177 – 185, 2010.

[71] J. Li, Y. Man-Sung, D. McNelis, and M. Simpson, "A comprehensive electrorefining process simulation model for pyroprocessing of spent fuel," (Makuhari, Japan), 2011 Global Conference, 2011.

[72] J. Zhang, "Echem modeling: A kinetic model for electrorefining based on diffusion control," tech. rep., Los Alamos National Laboratory, 2011.

[73] J. Zhang, "Parametric studies of uranium deposition and dissolution at solid electrodes," *Journal of Applied Electrochemistry*, vol. 44, pp. 383–390, Mar 2014.

[74] J. Zhang, "Kinetic model for electrorefining, part i: Model development and validation," *Progress in Nuclear Energy*, vol. 70, pp. 279 – 286, 2014.

[75] R. Cumberland, "1d and 3d simulation of electrochemical behavior of u/ucl3 and pu/pucl3 in molten salt systems," Master's thesis, Korean Advanced Institute of Science and Technology (KAIST), Daejeon, South Korea, 2013.

[76] R. M. Cumberland and M.-S. Yim, "A computational meta-analysis of ucl3 cyclic voltammograms in licl-kcl electrolyte," *Journal of the Electrochemical Society*, vol. 161, no. 4, pp. D147–D149, 2014.

[77] D. Rappleye, M. Simpson, R. Cumberland, and M. Yim, "A method for monitoring deposition at a solid cathode in an electrorefiner for a two-species system using electrode potentials," in *International Nuclear Fuel Cycle Conference, GLOBAL*

2013: Nuclear Energy at a Crossroads, vol. 2, pp. 1474–1480, American Nuclear Society, 2013.

[78] P. Lafreniere, “Identification of electrorefiner and cathode processing failure modes and determination of signature-significance for integration into a signature based safeguards framework for pyroprocessing,” Master’s thesis, University of New Mexico, 2013.

[79] P. L. Lafreniere, R. O. Hoover, and E. D. Blandford, “Determination of pyroprocessing cathode processor failure modes and integration into a signature-based safeguards (sbs) framework,” in *Institute of Nuclear Materials Management 55th Annual Meeting Proceedings*, 2014.

[80] R. M. Cumberland and M.-S. Yim, “Development of a 1d transient electrorefiner model for pyroprocess simulation,” *Annals of Nuclear Energy*, vol. 71, p. 52âĂŞ59, September 2014.

[81] T. Koyama, K. Kinosmta, T. Inoue, M. Ougier, R. Malmbeck, J.-P. Glatz, and L. Koch, “Study of molten salt electrorefining ofu-pu-zr alloy fuel,” *Journal of Nuclear Science and Technology*, vol. 39, no. 3, pp. 765–768, 2002.

[82] D. Rappleye, M. Simpson, R. Cumberland, D. McNelis, and M.-S. Yim, “Simulated real-time process monitoring of a molten salt electrorefiner,” *Nuclear Engineering and Design*, vol. 273, pp. 75 – 84, 2014.

[83] R. M. Cumberland and M.-S. Yim, “Development of a 1d transient electrorefiner model for pyroprocess simulations,” in *Transactions of the American Nuclear Society*, 2011.

[84] P. Bingham, R. J. Hand, M. C. Stennett, N. C. Hyatt, and M. T. Harrison, “The use of surrogates in waste immobilization studies : a case study of plutonium,” *MRS Proceedings*, vol. 1107, pp. 421–428, 2008.

[85] H. Hayashi, M. Takano, H. Otobe, and T. Koyama, "Syntheses and thermal analyses of curium trichloride," *Journal of Radioanalytical and Nuclear Chemistry*, vol. 297, pp. 139–144, Jul 2013.

[86] M. Bermejo, J. Gomez, A. Martinez, E. Barrado, and Y. Castrillejo, "Electrochemistry of terbium in the eutectic licl-kcl," *Electrochimica Acta*, vol. 53, no. 16, pp. 5106 – 5112, 2008.

[87] M. Bermejo, J. Gomez, J. Medina, A. Martinez, and Y. Castrillejo, "The electrochemistry of gadolinium in the eutectic licl-kcl on w and al electrodes," *Journal of Electroanalytical Chemistry*, vol. 588, no. 2, pp. 253–266, 2006.

[88] C. Caravaca, G. de Cordoba, M. TomÃąs, and M. Rosado, "Electrochemical behaviour of gadolinium ion in molten liclâĂŞkcl eutectic," *Journal of Nuclear Materials*, vol. 360, no. 1, pp. 25 – 31, 2007. Proceedings has been selected Proceedings of the Seventh International Symposium on Molten Salts Chemistry and Technology (MS7 âĂŞ Session 6: Workshop on Nuclear Energy and Nuclear Wastes.

[89] M. Iizuka, "Diffusion coefficients of cerium and gadolinium in molten liclâĂŘkcl," *The Electrochemical Society*, vol. 145, no. 1, pp. 84–88, 1998.

[90] P. Bagri, T. Bastos, and M. Simpson, *Electrochemical methods for determination of activity coefficients of lanthanides in molten salts*, vol. 75, pp. 489–495. Electrochemical Society Inc., 15 ed., 2016.

[91] I. Barin, *Thermochemical Data of Pure Substances.* Wiley-VCH Verlag GmbH, third ed., 1995.

[92] S. Adams and M. Simpson, "Simulated response to process abnormalities during spent nuclear fuel electrorefining," *Annals of Nuclear Energy*, vol. 110, pp. 1002 – 1009, 2017.

[93] Institute of Nuclear Materials Management, *Evolution of Safeguards-An*

Information-driven Approach to Acquisition Path Analysis, 55th Annual INMM Meeting, July 2014.

[94] K. B. Sylvester, “International safeguards for pyroprocessing: Options for evaluation,” tech. rep., Los Alamos National Laboratory, January 2003. LA-UR-03-0986.

[95] K. B. Sylvester and G. Eller, “Safeguards evaluation for a proposed pyroprocessing facility,” tech. rep., Los Alamos National Laboratory, June 2003. LA-UR-05-4364.

[96] E. Rauch, “Development of a safeguards approach for a small graphite moderated reactor and associated fuel cycle facilities,” masters thesis, Texas A&M University, 2009.